

CLIMATE CHANGE MONITORING REPORT 2021

June 2022

Published by the
Japan Meteorological Agency

3-6-9 Toranomom, Minato City, Tokyo 105-8431, Japan

E-mail iao-jma@met.kishou.go.jp

CLIMATE CHANGE MONITORING REPORT 2021

June 2022

JAPAN METEOROLOGICAL AGENCY

Preface

The Japan Meteorological Agency (JMA) has published annual reports under the title of Climate Change Monitoring Report since 1996 to provide up-to-date information on climate change in Japan and around the world based on the outcomes of its observations and its monitoring of the atmosphere and oceans.

Extreme meteorological phenomena around the world in 2021 included heat waves in North America and heavy rain in Central Europe. In mid- to late August, a wide area from western to eastern Japan experienced heavy rain due to enhanced frontal activity. In winter (December 2020 – January 2021), the country's Sea of Japan side experienced record heavy snowfall.

Long-term changes in the incidence of such extreme weather events are associated with global warming. The Meteorological Research Institute conducts research on the effects of climate change on individual phenomena, such as the Heavy Rain Event of July 2017 in Northern Kyushu, the Heavy Rain Event of July 2018, and Typhoon Hagibis (T1919). This report touches on the outcomes of such work.

As global warming continues, the frequency and intensity of extreme events are expected to increase, and consideration of climate change is urgently required. The importance of climate change issues is highlighted by the award of the 2021 Nobel Prize in Physics to Dr. Syukuro Manabe for his pioneering work on climate change projections.

In the coming years, climate change action will be promoted internationally under the Paris Agreement and domestically under the Global Warming Countermeasure Plan and the Climate Change Adaptation Plan.

Against this background, JMA released Climate Change in Japan 2020 – Assessment Report on Observed and Projected Climate Change in the Atmosphere, on Land and in Oceans – in December 2020 in conjunction with Japan's Ministry of Education, Culture, Sports, Science and Technology. The report presents scientific expertise on climate change in Japan, including differences observed and future projections for the global average temperature changes detailed in the RCP 2.6 and 8.5 scenarios (called the “2°C and 4°C warming scenarios” in the report). The observation details in the report are based on previous Climate Change Monitoring Reports and the latest observation data.

This report is intended to raise awareness of climate change, and is expected to be particularly useful to related organizations and stakeholders worldwide in their responses to climate change.



HASEGAWA Naoyuki
Director-General
Japan Meteorological Agency

Index

News	1
I COVID-19-related variations in atmospheric carbon dioxide concentration	1
II Record-heavy Rain in Japan in August 2021	4
III Record-high sea surface temperatures in the Sea of Japan and southeast of Hokkaido in July 2021	8
Chapter 1 Climate in 2021	11
1.1 Global climate summary	11
1.2 Climate in Japan	15
1.2.1 Annual characteristics.....	15
1.2.2 Seasonal characteristics	16
1.3 Atmospheric circulation and oceanographic conditions	20
1.3.1 Characteristics of individual seasons	20
1.3.2 Global average temperature in the troposphere	27
1.3.3 Asian summer monsoon	27
1.3.4 Tropical cyclones over the western North Pacific and the South China Sea.....	28
Chapter 2 Climate Change	30
2.1 Greenhouse gases	30
2.1.1 Concentration of carbon dioxide.....	31
2.1.2 Concentration of methane.....	36
2.1.3 Concentration of nitrous oxide	37
2.1.4 Concentration of halocarbons	38
2.2 Aerosols and surface radiation	42
2.2.1 Aerosols.....	42
2.2.2 Kosa (Aeolian dust).....	43
2.2.3 Solar radiation and downward infrared radiation.....	43
2.3 Temperature	46
2.3.1 Global surface temperature.....	46
2.3.2 Surface temperature over Japan.....	48
2.3.3 Long-term trends of extreme temperature events in Japan	49
2.3.4 Urban heat island effect at urban stations in Japan	50
2.4 Precipitation	53
2.4.1 Global precipitation over land	53

2.4.2	Precipitation over Japan.....	53
2.4.3	Long-term trends of extreme precipitation events in Japan	54
2.5	Snow depth and snow cover	58
2.5.1	Snow depth in Japan.....	58
2.5.2	Snow cover in the Northern Hemisphere.....	59
2.6	Tropical cyclones over the western North Pacific and the South China Sea	61
2.7	Phenology of cherry blossoms and acer leaves in Japan.....	62
2.8	Sea surface temperature	63
2.8.1	Global sea surface temperature.....	63
2.8.2	Global ocean heat content.....	64
2.8.3	Sea surface temperature (around Japan)	64
2.9	El Niño/La Niña and PDO (Pacific Decadal Oscillation).....	66
2.9.1	El Niño/La Niña	66
2.9.2	Pacific Decadal Oscillation.....	67
2.10	Sea levels around Japan.....	68
2.11	Sea ice.....	70
2.11.1	Sea ice in Arctic and Antarctic areas.....	70
2.11.2	Sea ice in the Sea of Okhotsk	72
2.12	Ocean carbon dioxide and ocean acidification	73
2.12.1	Ocean carbon dioxide	73
2.12.2	Ocean acidification	76

<i>Explanatory note on detection of statistical significance in long-term trends.....</i>	<i>80</i>
--	------------------

<i>Glossary.....</i>	<i>82</i>
-----------------------------	------------------

<i>References.....</i>	<i>87</i>
-------------------------------	------------------

News

I COVID-19-related variations in atmospheric carbon dioxide concentration

- It has been reported under the Global Carbon Project (GCP) and other initiatives that fossil fuel-related emissions of carbon dioxide (CO₂) in 2020 decreased due to COVID-19 restrictions. However, analysis based on observation data submitted to the World Data Centre for Greenhouse Gases (WDCGG) of the World Meteorological Organization (WMO) suggests that atmospheric CO₂ concentrations are still increasing.
- The theoretical growth rate for atmospheric CO₂ in 2020 (estimated from the decrease in emissions reported under the GCP) slowed, but the decrease in the growth rate was within natural year-to-year variation. WDCGG analysis also shows no detectable COVID-19-related reduction in CO₂ emissions in variations of the observed growth rate in the atmosphere.

Analysis conducted by the World Data Centre for Greenhouse Gases (WDCGG) of the World Meteorological Organization (WMO), which is operated by the Japan Meteorological Agency (JMA), shows that atmospheric concentrations of the main greenhouse gases (carbon dioxide (CO₂), methane (CH₄) and nitrous oxide (N₂O)) continue to increase, and that globally averaged atmospheric concentrations reached new highs in 2020 (WMO, 2021a). IPCC AR6 WG1 (IPCC, 2021) reported that observed increases in well-mixed greenhouse gas concentrations since around 1750 have been unequivocally related to human activity. Among these gases, CO₂ has the most significant effect on global warming, with atmospheric concentrations increasing year by year amid seasonal variations (Figure I.1). CO₂ is emitted into the atmosphere as a result of human activity such as fossil fuel combustion and land use changes (e.g., deforestation). Around half of emissions are absorbed by land ecosystems and oceans, and the remainder accumulates in the atmosphere. The balance between these determines the annual increase in atmospheric CO₂. The pre-industrial level (since around 1750) of 278 ppm in atmospheric CO₂ concentration represents a balance of CO₂ fluxes among the atmosphere, oceans and the terrestrial biosphere. The globally averaged CO₂ concentration in 2020 was 413.2 ppm, which is around 1.5 times the pre-industrial level.

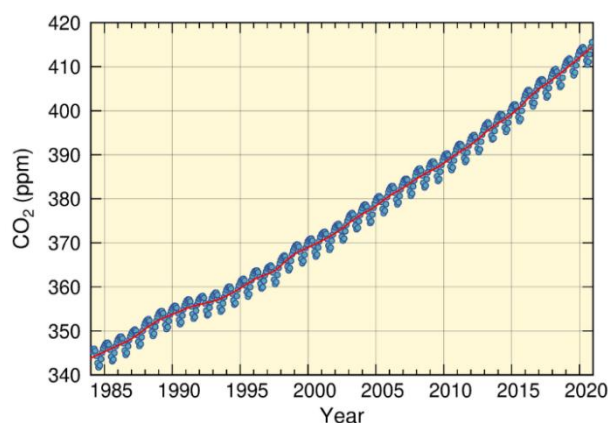


Figure I.1 Globally averaged concentrations of atmospheric CO₂

Blue dots are monthly values, and the red line represents the corresponding sequence after removal of seasonal variations (WMO, 2021a). Data are based on observations reported to WDCGG using the WMO method (2009). Contributors are listed in WMO (2022).

The onset of COVID-19 in early 2020 prompted the implementation of lockdowns and other restrictions on a global scale, resulting in decreased anthropogenic CO₂ emissions (WMO, 2020). Analysis conducted under the Global Carbon Project (GCP)¹ in 2021 indicates that 2020 fossil fuel-related CO₂ emissions were 9.5±0.5 GtC, which is around 5.4% down from 2019 (Friedlingstein et al., 2021). Figure I.2 shows annual mean growth rates for atmospheric CO₂ calculated from WDCGG observation analysis and theoretical growth rates estimated from fossil fuel-related CO₂ emissions (assuming no CO₂ absorption by the terrestrial biosphere and oceans). The observed increase in the annual mean from 2019 to 2020 (2.5 ppm) was slightly lower than that observed from 2018 to 2019 (2.6 ppm) but slightly higher than the average growth rate for the previous decade (2.4 ppm/year). Thus, the tendency in variations of the observed atmospheric growth rate for CO₂ did not change significantly. The contribution of changes in atmospheric CO₂ concentrations estimated from reduced CO₂ emissions in 2020 is assumed to be about 0.2 ppm (Figure I.2, green curve), which is significantly lower than the 1 ppm of natural year-to-year variations. This means that the effects of COVID-19 restrictions cannot be distinguished from natural annual variability (WMO, 2020; WMO, 2021b).

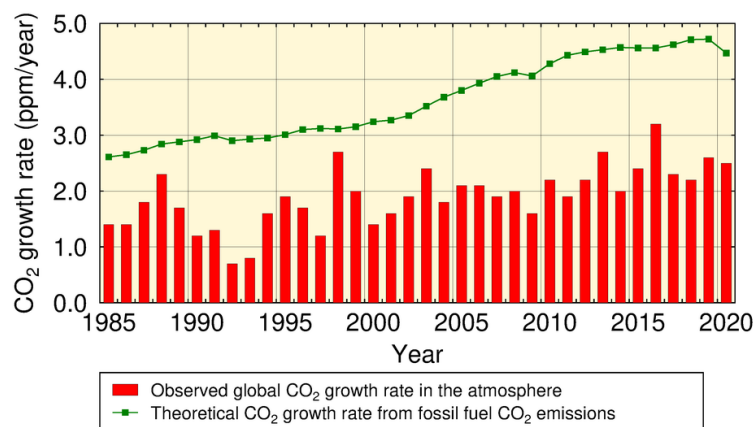


Figure I.2 Observed growth rate for atmospheric CO₂ and theoretical growth rate calculated from fossil fuel-related CO₂ emissions

Annual mean growth rates for atmospheric CO₂ calculated using observation data from WDCGG analysis (red columns), and theoretical growth rates driven by fossil fuel-related CO₂ emissions assuming no CO₂ absorption by the terrestrial biosphere and oceans (green curve). The theoretical data were calculated taking fossil fuel-related CO₂ emissions as a proxy (from the Global Carbon Project (Friedlingstein et al., 2021)), converted to moles based on the conversion factor 2.124 GtC/ppm (Ballantyne et al., 2012).

To evaluate effects relating to reduced emissions of greenhouse gases and aerosols due to the pandemic, a multi-model intercomparison for COVID-19 (called CovidMIP) has been implemented by international research teams (including the Japan Agency for Marine-Earth Science and Technology (JAMSTEC) and the Meteorological Research Institute of the Japan Meteorological Agency (MRI/JMA)) using state-of-the-art climate models. The results indicate that even though emissions of greenhouse gases and anthropogenic aerosols decreased from 2020 to 2021, effects on surface temperature and precipitation during the period 2020 – 2024 are likely to be small, and the temporary reduction in emissions due to COVID-19 will have a limited effect on global warming (Jones et al., 2021).

Reports from JMA observation stations indicate that annual mean concentrations of atmospheric CO₂ reached new highs in 2021, with 419.5 ppm at Ryori, 416.9 ppm at Minamitorishima and 419.2 ppm at Yonagunijima (based on preliminary estimations) (Figure I.3). The increase from the previous year was 2.0 to

¹ A core global project of Future Earth – an international collaborative research platform established in 2001 to support the realization of global sustainability.

3.2 ppm/year, which is comparable to the mean annual absolute increase over the previous 10 years. Ratios of atmospheric concentrations for CO₂ and CH₄ from observation stations in Japan suggest reduced fossil fuel-related CO₂ emissions around East Asia in 2020 (Tohjima et al., 2020; Tohjima et al., 2022), but the value is expected return to pre-COVID-19 levels. GCP analysis from 2021 also suggests that fossil fuel-related CO₂ emissions stood at around 9.9 GtC, representing an increase of around 4.9% from 2020 and a return to the pre-COVID-19 2019 level of 10.0±0.5 GtC (Friedlingstein et al., 2021). Atmospheric CO₂ concentrations are still increasing, and it is important to continue long-term wide-area observation and analysis of atmospheric greenhouse gas concentrations.

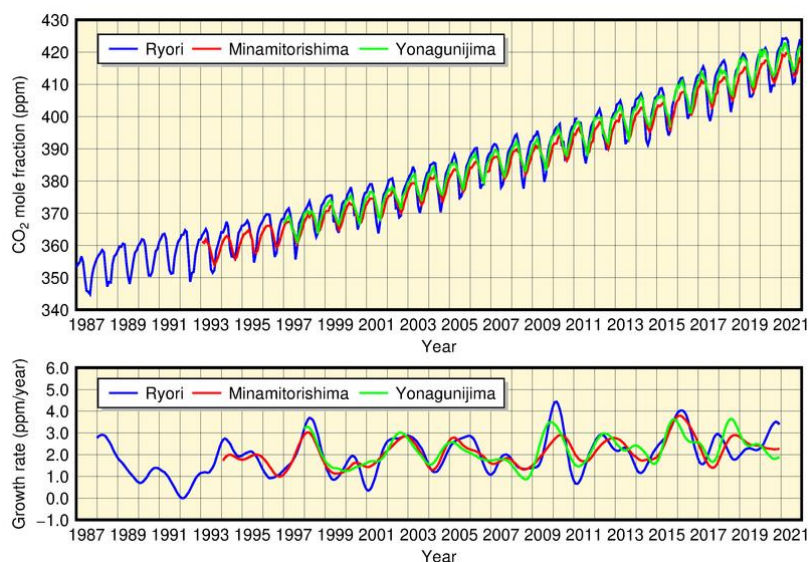


Figure I.3 Monthly mean concentrations (a) and corresponding growth rates (b) of atmospheric CO₂ observed at Ryori (blue), Minamitorishima (red) and Yonagunijima (green). Growth rate calculation is described in WMO (2009).

II Record-heavy Rain in Japan in August 2021

- In mid-August 2021, a wide area from western to eastern Japan experienced record-heavy rain, with total precipitation exceeding 1,400 mm in many places. The Sea of Japan side and the Pacific side of western Japan recorded the highest monthly precipitation in August since statistics began in 1946.
- Unusually for mid-summer in eastern and western Japan, like atmospheric flow in the latter half of the early-summer rainy season known as the Baiu, a stationary front was strengthened by a significant north-south gradient of temperature in the lower troposphere between the Okhotsk High to the north of Japan and the southward shifted North Pacific Subtropical High expanding to the south of Japan. A continuous confluence of water vapor from continental China and along the margin of the North Pacific Subtropical High also contributed to widespread continuous heavy rainfall.

(1) Weather Conditions

In mid- to late August 2021, a wide area from western to eastern Japan experienced heavy rainfall, with periodic precipitation exceeding 1,400 mm at many locations in southern Kyushu and Shikoku regions from August 11 to 26 (Figure II.1). In particular, the northern parts of the Kyushu and Chugoku regions experienced record-heavy rainfall associated with quasi-stationary band-shaped precipitation systems from August 12 to 14. Monthly precipitation amounts for August were around 3.7 times the normal for the Sea of Japan side of western Japan and around 3.0 times the normal for the Pacific side of western Japan, making them the highest since 1946. Rainfall on the Pacific side of eastern Japan was also around 2.2 times the normal, making it the second highest since the same year. In addition, 30 meteorological stations, including Kure (Hiroshima Prefecture), Kumamoto (Kumamoto Prefecture) and Makurazaki (Kagoshima Prefecture), recorded the highest monthly precipitation amounts.

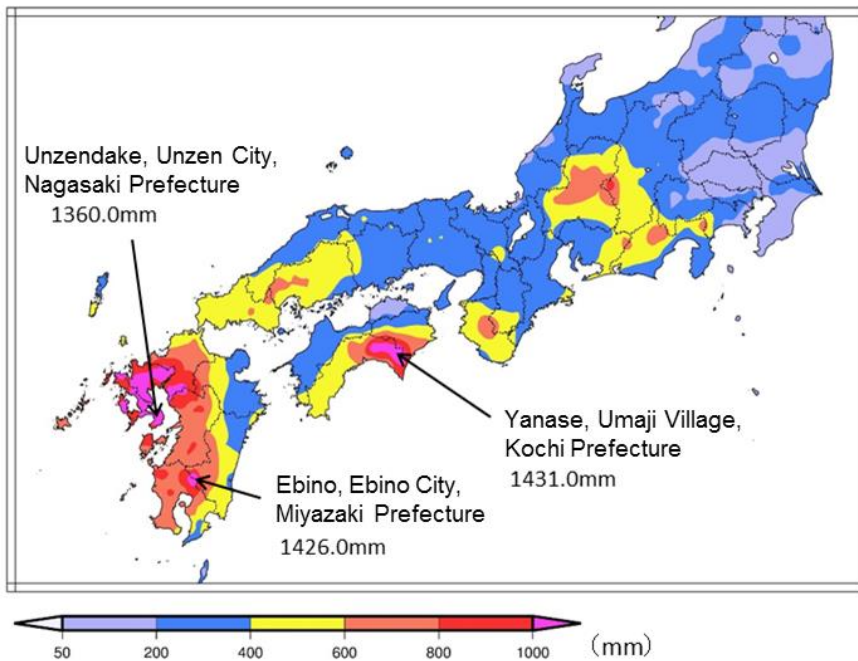


Figure II.1 Total precipitation amounts [mm] for 11 – 26 August, 2021.

(2) Characteristics of Atmospheric Circulation

To identify possible causative factors, the Japan Meteorological Agency held the JMA Advisory Panel on Extreme Climate Events (a JMA body staffed by prominent experts on climate science from universities and research institutes) on 13th September 2021 and summarized factors contributing to these extreme climatic conditions as outlined below.

From early August onward, unusually for mid-summer in eastern and western Japan, like atmospheric flow in the latter half of the early-summer rainy season known as the Baiu, a stationary front was strengthened by a significant north-south gradient of temperature in the lower troposphere between the Okhotsk High to the north of Japan and the southward shifted North Pacific Subtropical High (NPSH) expanding to the south of Japan (Figure II.2a). A continuous confluence of water vapor from continental China and along the margin of the NPSH also contributed to widespread continuous heavy rainfall.

The Okhotsk High on the surface developed from the first half of early August onward, and persisted due to an enhanced blocking high over Eastern Siberia resulting from persistent meandering of the polar-front jet stream (PFJ) in the upper troposphere (Figure II.2b). The significant enhancement of the stream in July may have contributed to this meandering from the first half of early August onward.

The NPSH shifted farther southward than normal and expanded to the seas south of Japan. This anomaly is attributed to inactive convection over the western North Pacific (Figure II.3a), which in turn resulted from tropical intra-seasonal oscillation. Water vapor inflow toward Japan from the south along the margin of the NPSH frequently occurred. Eastern China also experienced significantly above-normal precipitation amounts due to an active front near the region. The westerly jet stream was stronger than normal from China to Japan in association with an enhanced north-south temperature gradient in the middle-to-lower troposphere, causing favorable conditions for the above water vapor inflow.

The southward shift of the NPSH was related to the southward shift of the subtropical jet stream (STJ) from East Asia to Japan in the upper troposphere. The Tibetan High was intensified over southern China and a pressure trough was seen to the northeast over the East China Sea in the upper troposphere (Figure II.3b), corresponding to the significant southward meandering of the STJ to the west of Japan. This meandering is considered to have promoted upward airflow and persistent rainfall over areas from western to eastern Japan. After 15th August, northward meandering of the westerly jet stream associated with an enhanced pressure ridge over the North Atlantic may have influenced meandering over Eurasia. This may have extended farther eastward, promoting a persistent pressure trough to the west of Japan.

The negative phase of Indian Ocean Dipole (IOD) over the Indian Ocean was accompanied by positive SST anomalies to the southwest of Sumatra and negative anomalies in the western Indian Ocean (Section 1.3.1). The negative phase of the IOD may have influenced convective activity over the Asian monsoon region and affected atmospheric circulation over East Asia. Convective activity over the Asian monsoon region was suppressed from the South China Sea to the seas east of the Philippines, and exhibited a southwestward-shifted center (Figure II.3a). Statistical analysis of atmospheric circulation shows that the STJ over East Asia tended to shift southward of its normal position and a pressure trough was seen to the west of Japan in association with suppressed and southwestward-shifted convection over the Asian monsoon region. This is consistent with the atmospheric circulation seen in mid-August 2021, suggesting that anomalous convection associated with the Asian monsoon may have contributed to the widespread continuous heavy rain.

The intensity of extreme heavy rainfall in Japan exhibits an increasing trend, with maximum annual rainfall over periods of 72 hours at Automated Meteorological Data Acquisition System (AMeDAS) observation sites increasing by 3.7% per decade since 1976 (Section 2.4.3). A potential factor behind this long-term trend is an increasing trend in atmospheric water vapor concentrations associated with rising temperatures

due to global warming. Saturated water vapor is theoretically known to increase by around 7% for each 1°C rise in temperature. Although further research is needed, it is feasible that increasing water vapor concentrations caused by global warming may have contributed to the heavier rainfall observed.

The primary factors contributing to the record-heavy rain from western to eastern Japan are illustrated in Figure II.4.

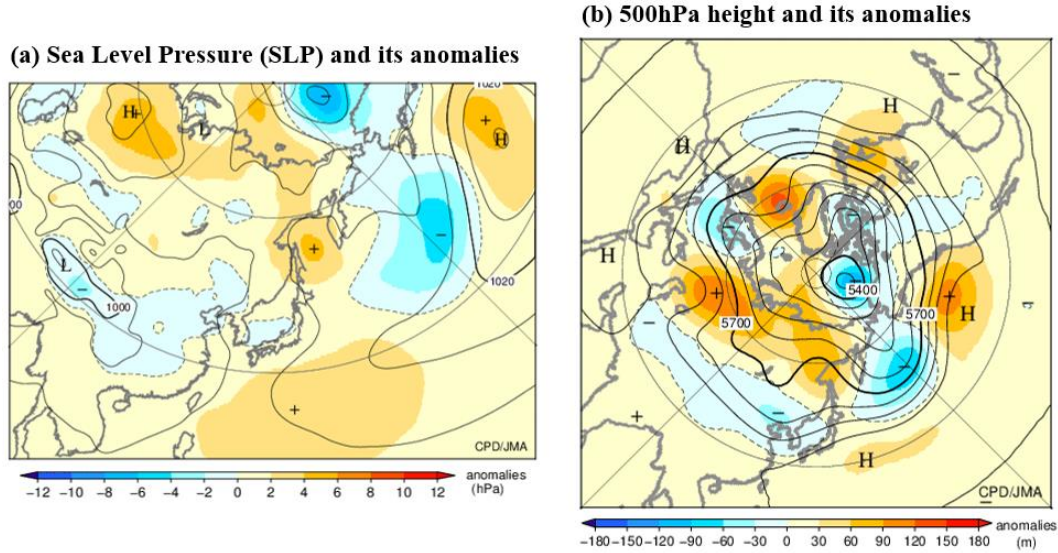


Figure II.2 (a) Sea level pressure and related anomalies, and (b) 500-hPa height and related anomalies, both for August 2021

Units are (a) hPa and (b) m, and the base period for the normal is 1991 – 2020. Graphs are based on the Japanese 55-year reanalysis (JRA-55) dataset.

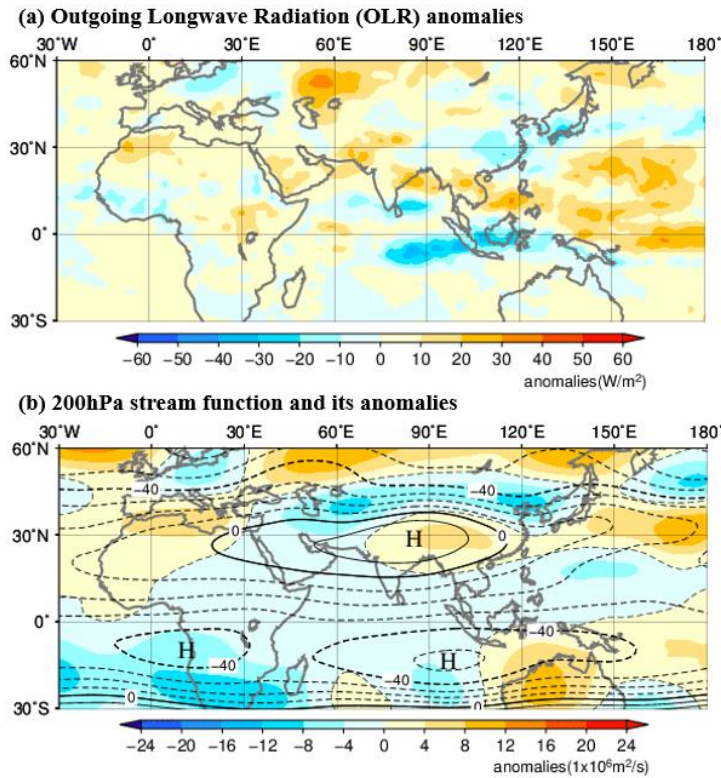


Figure II.3 (a) Outgoing longwave radiation (OLR) anomalies and (b) 200-hPa stream function and related anomalies, both for August 2021

Units are (a) W/m^2 and (b) $10 \times 10^6 m^2/s$, and the base period for the normal is 1991 – 2020. Graphs are based on (a) OLR data from the National Oceanic and Atmospheric Administration (NOAA) and (b) JRA-55.

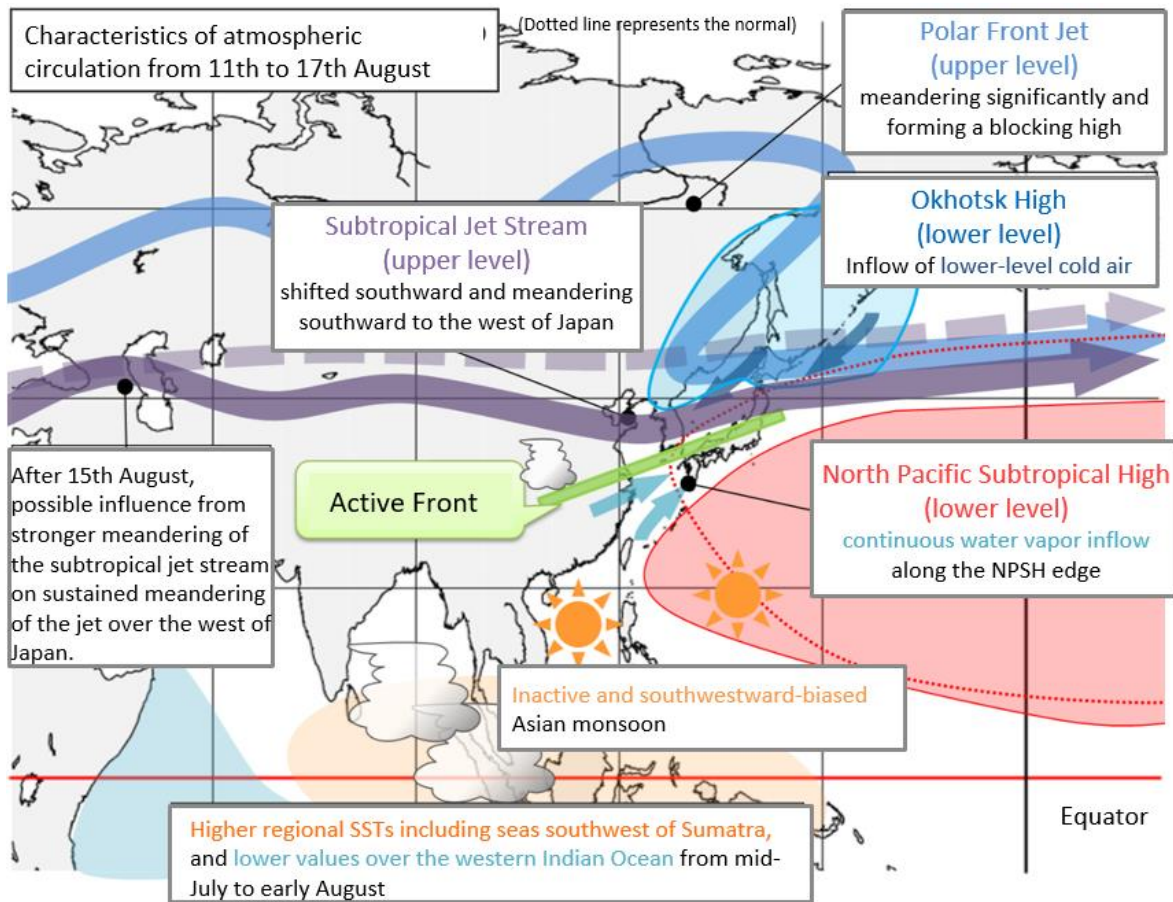


Figure II.4 Characteristics of atmospheric circulation causing record-heavy rain from 11th to 17th August

III Record-high sea surface temperatures in the Sea of Japan and southeast of Hokkaido in July 2021

- In July 2021, monthly mean sea surface temperatures (SSTs) in the Sea of Japan and east of Japan were much higher than normal, and area-averaged SSTs for northern and southern parts of the Sea of Japan and southeast of Hokkaido were the highest for July since 1982.

JMA monitors sea surface temperatures (SSTs) in the western North Pacific based on satellite, ship and buoy data. Figure III.1, which shows monthly mean SSTs and related anomalies for July 2021, indicates that SSTs in the Sea of Japan and east of Japan were much higher than normal. Figure.III.2, which shows area-averaged SSTs for July and related anomalies, indicates values of 22.6°C (+3.8°C) for the northern part of the Sea of Japan (Area A in Fig III.1), 25.7 °C (+2.9°C) for its southern part (Area B) and 17.7°C (+2.4°C) for the area southeast of Hokkaido (Area C) in 2021. These area-averaged SSTs and the related anomalies for July 2021 were the highest since 1982. Note that the values for 2021 are based on near-real time analysis.

Time-series representations of daily area-averaged SSTs for each area (Fig III.3) began to exhibit higher values than normal in mid-July 2021, and significantly exceeded the previous daily high (from 1982) in late July. Area-averaged SSTs were nearly constant for the Sea of Japan (Areas A and B) and increased at almost the same rate as the normal for areas southeast of Hokkaido (Area C) from late July to early August. Values for all three areas had significantly decreased to near or below normal by mid-August.

In July 2021, the Sea of Japan and the area east of Japan experienced warm-air coverage, much lower surface wind speeds and much more solar radiation than usual in association with a strong atmospheric high-pressure system over a wide area around northern Japan from mid-July to the first half of late July (Fig III.4). These atmospheric conditions are likely to have contributed to the high SSTs recorded in the Sea of Japan and southeast of Hokkaido. Meanwhile, the significant SST decrease observed around mid-August is attributed to the passage of Typhoon Mirinae (T2110) and an extratropical cyclone resulting from Tropical Storm Lupit (T2109), and subsequent cold air flow in the lower layer from the Okhotsk High.

Global SSTs have increased over the last 100 years (Section 2.8). Sea temperatures across a certain area can exhibit extreme rises over short periods, and the resulting warm conditions can persist for days to months covering thousands of square kilometers. These events are commonly referred to as marine heatwaves (MHWs), and have received particular attention in recent years. MHWs were covered in the IPCC Special Report on the Ocean and Cryosphere in a Changing Climate (SROCC; IPCC (2019)), which highlighted their severe impacts on marine ecosystems and fisheries and reported: "marine heatwaves have very likely doubled in frequency since 1982 and are increasing in intensity."

JMA does not currently issue information on MHWs. However, Kuroda and Seto (2021) considered anomalous warm SSTs in the field from the perspective of MHWs, reporting an area-averaged MHW index from the area south of the Okhotsk Sea to the northern part of the western North Pacific (40 – 50°N, 143°E – 180°) in summer 2021 based on daily SST analysis from 1982 onward. The number of days on which MHW index values exceeded a certain threshold was dominant in July – August 2021, indicating significant intensity during this period. It was also reported that these MHWs were caused by an extreme northward shift of the atmospheric westerly jet and a subsequent strong high-pressure system near the sea surface. MHWs are driven both by atmospheric forcing and oceanic processes. Miyama *et al.* (2021) reported that the consistent summer MHWs observed from 2010 to 2016 off the Hokkaido and Tohoku regions were likely caused by blocking of the southward Oyashio flow by warm-core eddies in these sea areas, and also suggested that MHWs may support increased catches of yellowtail in the Pacific area off southeastern Hokkaido.

IPCC AR6 WG1 (IPCC, 2021) indicated that MHWs had approximately doubled in frequency since the 1980s (high confidence), and that human influence had very likely contributed to most instances since at least 2006. As MHWs affect socio-economic activity via effects such as shifting of fishing grounds, aquacultural damage and coral breaching, it is important to maintain monitoring of related oceanic variables.

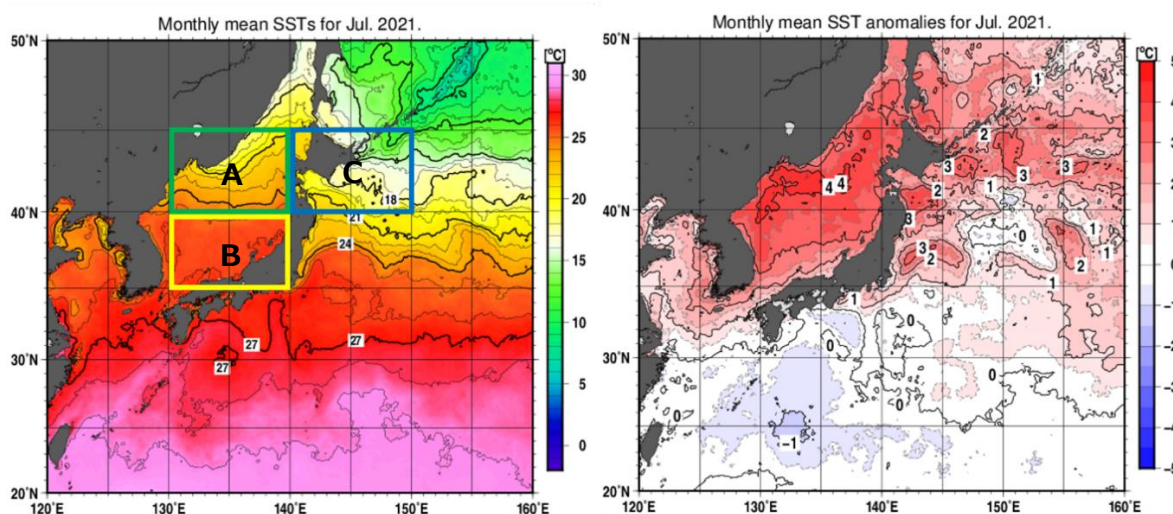


Figure III.1 July mean SSTs (left) and related anomalies (right) in 2021.

SST anomalies are deviations from the normal for the period 1991 – 2020. SSTs are near-real time analysis values. The green, yellow and blue rectangles in the figure on the left indicate averaged areas for the SST time-series representations in Figure III.2 and Figure III.3.

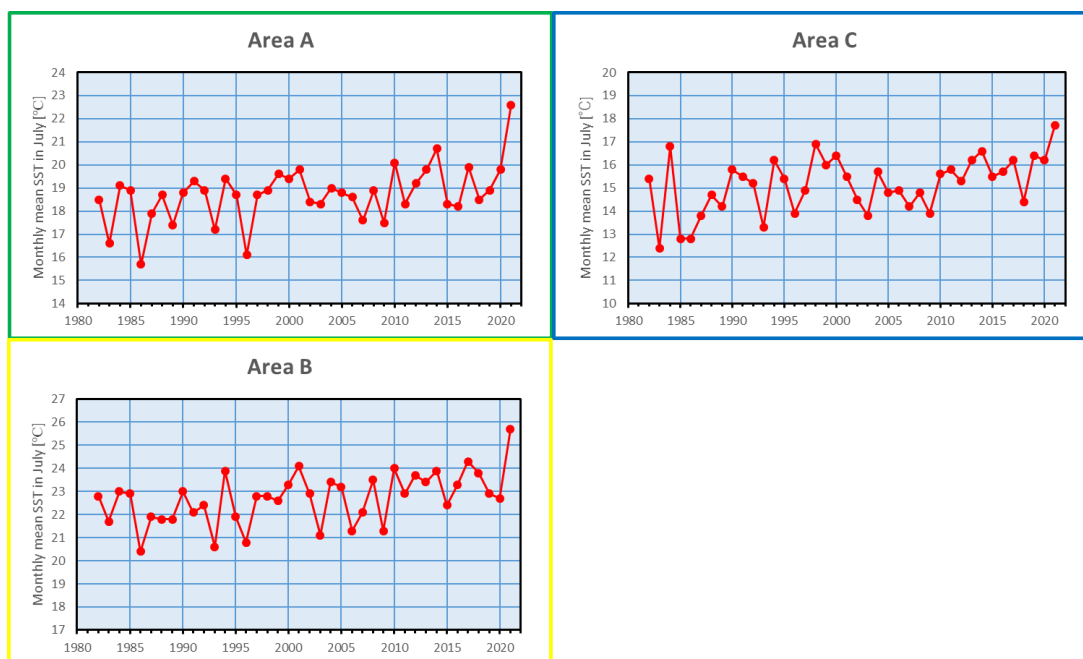


Figure III.2 July mean SSTs since 1982 for the rectangle areas shown in Figure III.1.

Values for 2021 are based on near-real time analysis.

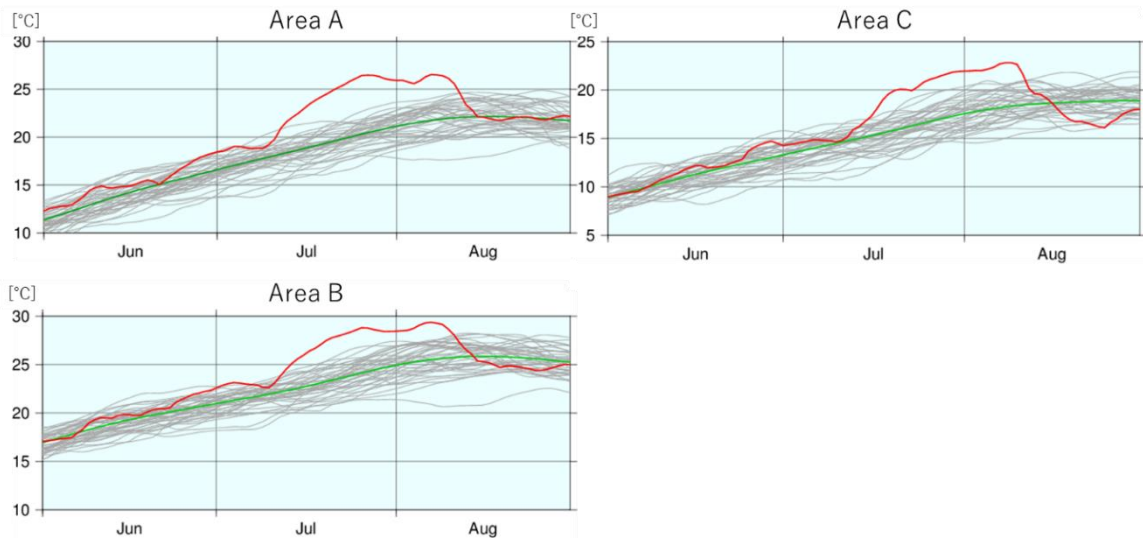


Figure III.3 Time-series representations of daily SSTs from June to August for the rectangle areas shown in Figure III.1.

Red, grey and green lines are time-series representations for 2021, other individual years from 1982 to 2020 and the normal, respectively. The base period for the normal is 1991 – 2020. Values for 2021 are based on near-real time analysis.

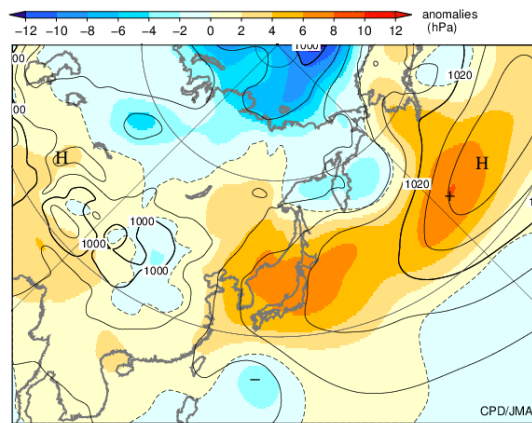


Figure III.4 10-day mean sea level pressure and anomalies around Japan (11 Jul. 2021 – 20 Jul. 2021). Contours show sea level pressure at intervals of 4 hPa, and shading indicates sea level pressure anomalies.

The base period for the normal is 1991 – 2020.

Chapter 1 Climate in 2021

1.1 Global climate summary

- Extremely high temperatures and extremely high precipitation amounts were observed in various parts of the Northern Hemisphere.
- Disaster conditions resulting in many fatalities were caused by heavy rain in central China in July, a typhoon running from the central to the southern Philippines in December, heavy rain in and around South Asia from May to November, heavy rain in central Europe in July, and heat waves from the central to the western part of North America from June to July.

Major extreme climate events² and weather-related disasters that occurred in 2021 are shown in Figure 1.1-1 and Table 1.1-1.

Extremely high temperatures ((4), (9), (12), (15), (16), (17), (19), (21) in Figure. 1.1-1) and extremely heavy rain ((1), (2), (13), (14), (18), (25) in Figure. 1.1-1) were observed in many areas over the Northern Hemisphere.

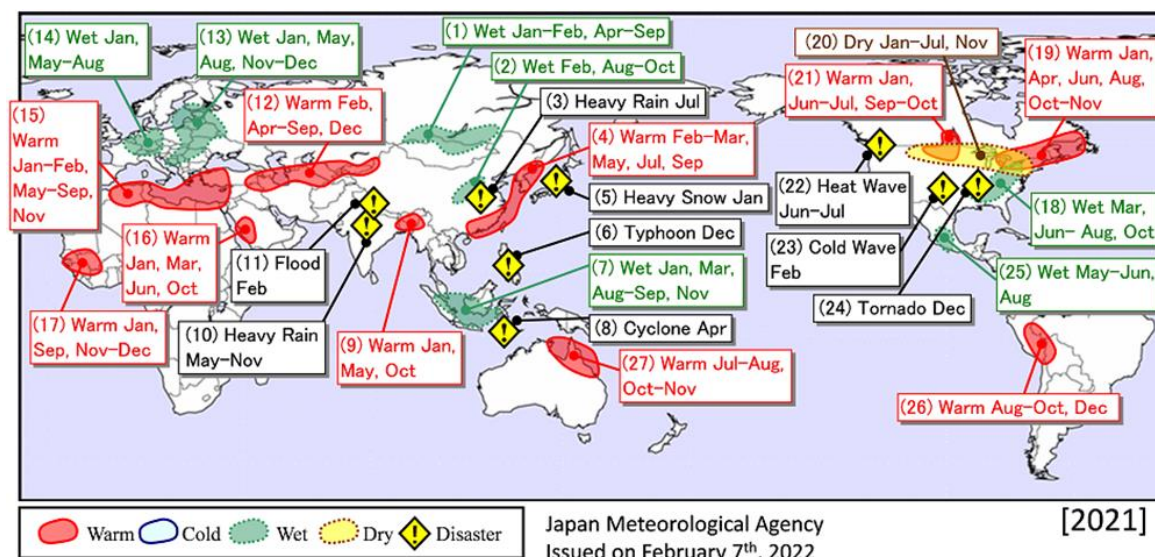


Figure 1.1-1 Major extreme events and weather-related disasters observed in 2021³

Schematic representation of major extreme climatic events and weather-related disasters occurring during the year.

“Warm”, “Cold”, “Wet” and “Dry” indicate that monthly extreme events occurred three times or more during the year in these regions. JMA defines an extreme climate event as a phenomenon likely to happen only once every 30 years.

Data and information on disasters are based on official reports of the United Nations and national governments and databases of research institutes (EM-DAT).

EM-DAT: The Emergency Events Database - Université Catholique de Louvain (UCL) - CRED, D. Guha-Sapir - www.emdat.be, Brussels, Belgium.

From the northern Korean Peninsula to southeastern China, extremely high temperatures were observed from February to March and in May, July, and September ((4) in Figure 1.1-1). Record-breaking monthly and seasonal mean temperatures were reported in Korea, China and Hong Kong (Korean Meteorological

² Extreme climate events are defined by anomalies or ratios to climatological normals. Normals represent mean climate conditions at given sites, and are currently based on a 30-year mean covering the period from 1991-2020.

³ Annual distribution maps for major extreme climatic events and weather-related disasters after 2008 are provided at JMA’s website.

<https://www.data.jma.go.jp/tcc/tcc/products/climate/annual/index.html>

Administration, China Meteorological Administration, and Hong Kong Observatory). The annual mean temperature in China in 2021 was the highest on record since 1961 (China Meteorological Administration). From southeastern Canada to the northeastern USA, extremely high temperatures were observed in January, April, June and August, and from October to November ((19) in Figure 1.1-1). In the northeastern USA, monthly mean temperatures in August and October were the highest on record since 1895 (National Oceanic and Atmospheric Administration, USA).

Extremely high precipitation amounts were observed in eastern Europe in January, May, August and from November to December ((13) in Figure 1.1-1), and in central Europe in January and from May to August ((14) in Figure 1.1-1). Conversely, from southeastern Canada to the northern USA, extremely low precipitation amounts were observed from January to July and in November ((20) in Figure 1.1-1). In the northern USA, monthly precipitation in June was the lowest on record since 1895 (National Oceanic and Atmospheric Administration, USA).

Heavy rain in central China in July ((3) in Figure 1.1-1) caused more than 300 fatalities (source: government of China). Typhoon Rai in December ((6) in Figure 1.1-1) caused more than 400 fatalities from the central to the southern Philippines (source: government of the Philippines). Heavy rain from May to November ((10) in Figure 1.1-1) caused more than 2,200 fatalities in and around South Asia (governments of India, Nepal, Pakistan, Sri Lanka, and EM-DAT). Heavy rain in central Europe in July ((14) in Figure 1.1-1) caused more than 240 fatalities (EM-DAT). Heat waves from central to western parts of North America from June to July ((22) in Figure 1.1-1) caused more than 1,000 fatalities (EM-DAT, the state government of Oregon, and the state government of Washington).

Annual mean temperatures were above normal in the Northern Hemisphere and elsewhere, especially in the eastern part of East Asia, from the southern part of Central Asia to the northern part of Northern Africa, and from eastern Canada to the northern USA (Figure 1.1-2).

Annual precipitation amounts were above normal from the southern part of Central Siberia to eastern China, in and around Indonesia, and in western India. Annual precipitation amounts were below normal from the southern part of Central Asia to the eastern Arabian Peninsula, and in the northwestern part of Northern Africa (Figure 1.1-3).

Table 1.1-1 Major extreme climatic events and weather-related disasters worldwide in 2021

No.	Type	Period	Area
(1)	Wet	January-February, April-September	From the southern part of Central Siberia to northern Mongolia
(2)	Wet	February, August-October	Central China
(3)	Heavy Rain	July	Central China
(4)	Warm	February-March, May, July, September	From the northern Korean Peninsula to southeastern China
(5)	Heavy Snow	January	In and around the Sea of Japan side of eastern Japan
(6)	Typhoon	December	From the central to southern Philippines
(7)	Wet	January, March, August-September, November	From Sumatra Island to Sulawesi Island
(8)	Cyclone	April	From southeastern Indonesia to Timor-Leste
(9)	Warm	January, May, October	In and around the eastern part of South Asia
(10)	Heavy Rain	May-November	In and around South Asia
(11)	Flood	February	Northern India
(12)	Warm	February, April-September, December	In and around the southern part of Central Asia
(13)	Wet	January, May, August, November-December	Eastern Europe
(14)	Wet	January, May-August	Central Europe
(15)	Warm	January-February, May-September, November	From the northern part of Northern Africa to the western Middle East
(16)	Warm	January, March, June, October	Western Saudi Arabia
(17)	Warm	January, September, November-December	The southwestern part of Western Africa
(18)	Wet	March, June-August, October	From the northeastern to southern USA
(19)	Warm	January, April, June, August, October-November	From southeastern Canada to the northeastern USA
(20)	Dry	January-July, November	From southeastern Canada to the northern USA
(21)	Warm	January, June-July, September-October	The central part of North America
(22)	Heat Wave	June-July	From the central to western part of North America
(23)	Cold Wave	February	From the central to southern USA
(24)	Tornado	December	The central USA
(25)	Wet	May-June, August	Central Mexico
(26)	Warm	August-October, December	From eastern Peru to northern Bolivia
(27)	Warm	July-August, October-November	Northeastern Australia

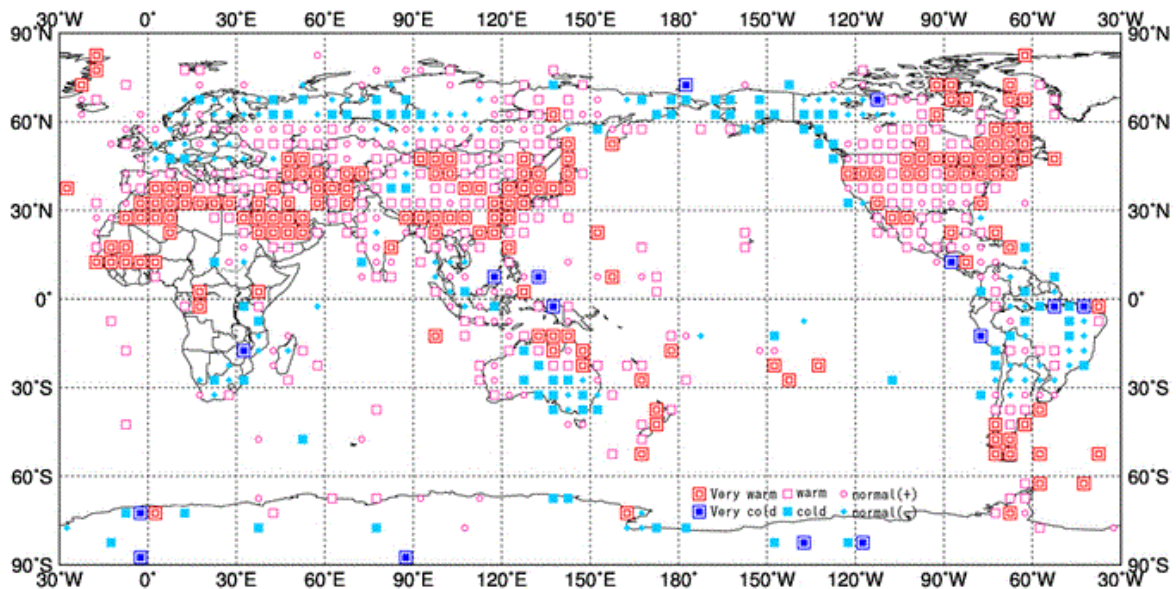


Figure 1.1-2 Normalized annual mean temperature anomalies for 2021⁴

Categories are defined by the annual mean temperature anomaly against the normal divided by its standard deviation and averaged in $5^\circ \times 5^\circ$ grid boxes. Red/blue marks indicate values above/below the normal calculated for the period from 1991 to 2020. The thresholds of each category are -1.28 , -0.44 , 0 , $+0.44$ and $+1.28$ ⁵. Land areas without graphics represent regions for which the observation data sample is insufficient or normal data are unavailable.

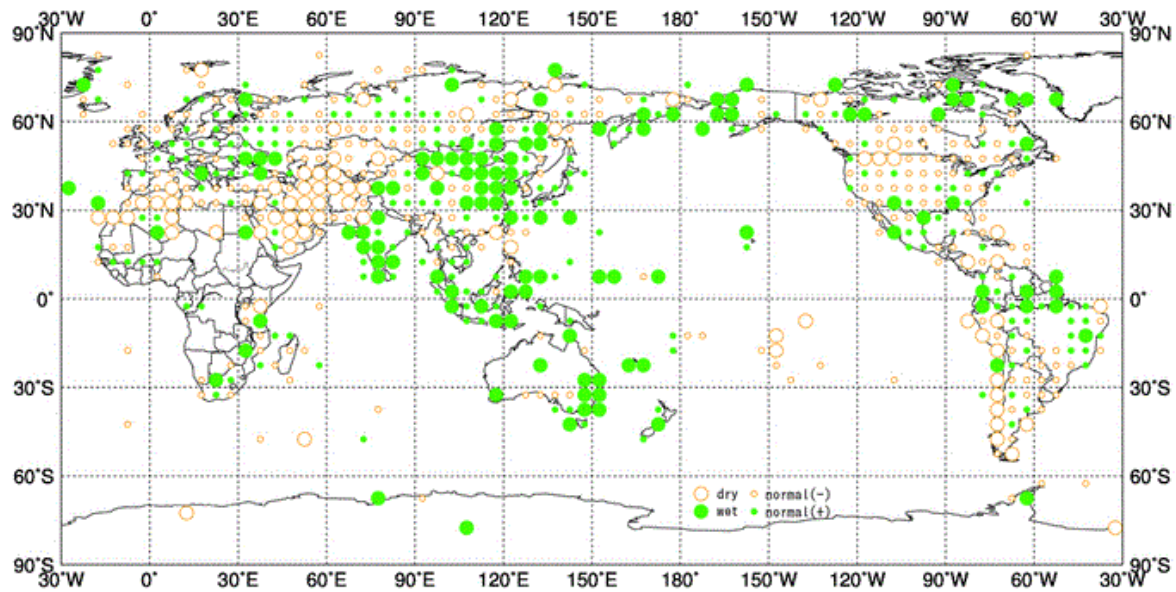


Figure 1.1-3 Annual total precipitation amount ratios for 2021

Categories are defined by the annual precipitation ratio to the normal averaged in $5^\circ \times 5^\circ$ grid boxes. Green/yellow marks indicate values above/below the thresholds. The thresholds of each category are 70, 100 and 120% of the normal calculated for the period from 1991 to 2020. Land areas without graphics represent regions for which the observation data sample is insufficient or normal data are unavailable.

⁴ Distribution maps for normalized annual mean temperature anomaly and precipitation amount ratio to normal after 2008 are provided at JMA's website.

<https://www.data.jma.go.jp/tcc/tcc/products/climate/annual/index.html>

⁵ In normal distribution, values of 1.28 and 0.44 correspond to occurrence probabilities of less than 10 and 33.3%, respectively.

1.2 Climate in Japan⁶

- Annual mean temperatures were above normal nationwide throughout most of the period. Values were significantly above normal in northern and western Japan in particular.
- In winter (Dec. 2020 – Jan. 2021), a series of heavy snowfall events occurred on the Sea of Japan side of the country.
- In mid-August 2021, western and eastern Japan experienced record-heavy rainfall.

1.2.1 Annual characteristics

The annual climate anomaly/ratio for Japan in 2021 is shown in Figure 1.2-1.

- Annual mean temperatures were above normal nationwide, and were significantly above normal in northern and western Japan.
- Annual precipitation amounts were significantly above normal on the Pacific side of eastern Japan, above normal on the Pacific side of northern Japan and in eastern and western Japan, and near normal on the Sea of Japan side of northern Japan and in Okinawa/Amami.
- Annual sunshine durations were above normal except on the Pacific side of western Japan, where values were near normal, and were significantly above normal on the Sea of Japan side of northern and eastern Japan and in Okinawa/Amami.

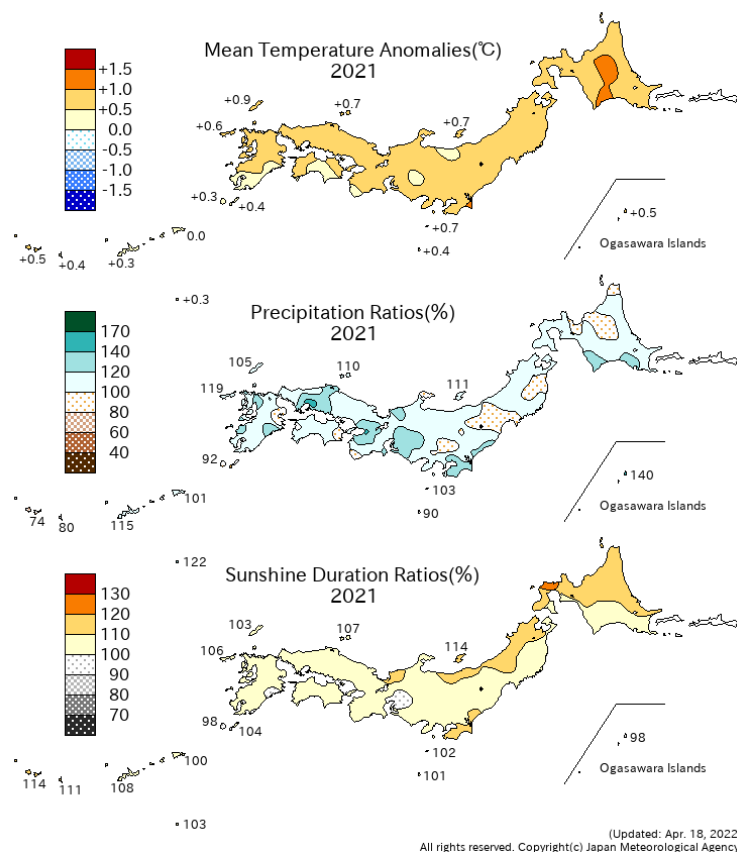
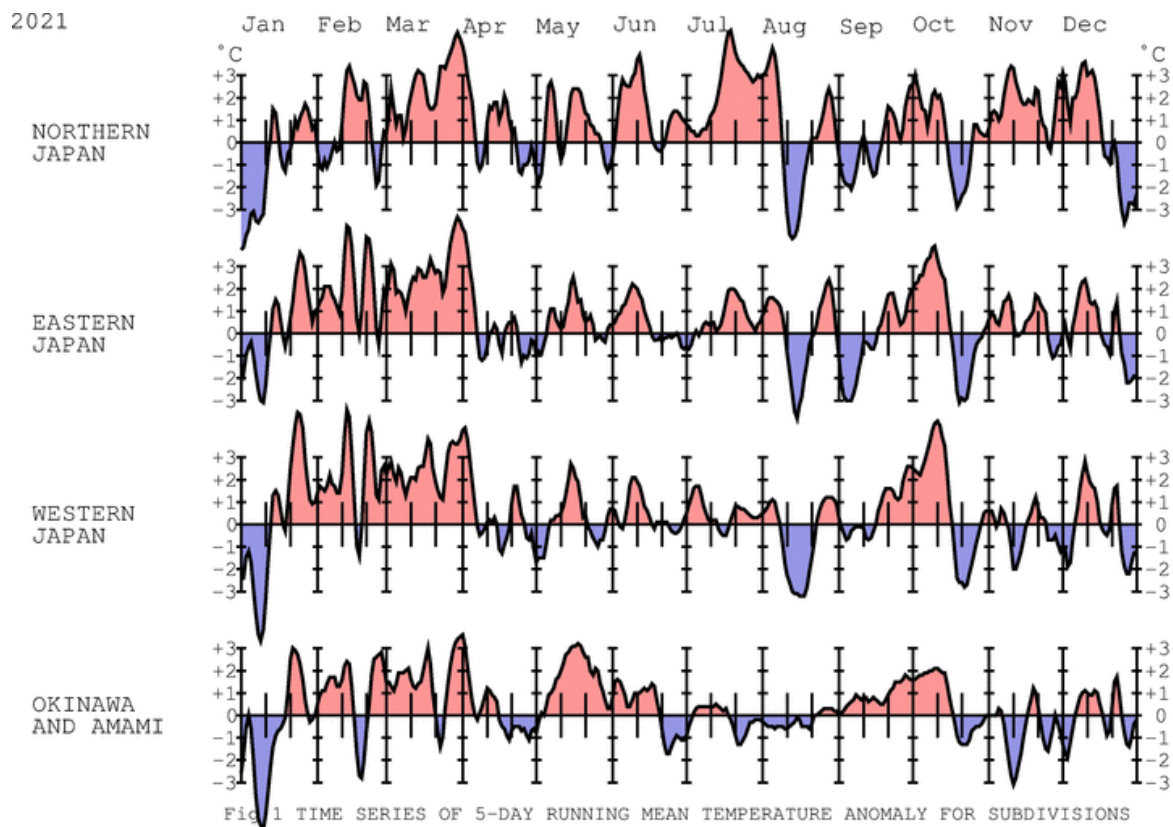


Figure 1.2-1 Annual climate anomaly/ratio for Japan in 2021

The base period for the normal is 1991 – 2020.

⁶ The term significantly above normal is used for cases in which observed mean temperatures or precipitation amounts exceed the 90th percentile for the base period (1991 – 2020), and significantly below normal is used when the corresponding figures fall below the 10th percentile.



Last Data:2022/ 1/ 2

Figure 1.2-2 Five-day running mean temperature anomaly for divisions (January – December 2021)

The base period for the normal is 1991 – 2020.

1.2.2 Seasonal characteristics

Five-day running mean temperature anomalies for different divisions (January – December 2021) are shown in Figure 1.2-2, and seasonal anomalies/ratios for Japan in 2021 are shown in Figure 1.2-3. Numbers of observatories reporting record monthly and annual mean temperatures, precipitation amounts and sunshine durations (2021) are shown in Table 1.2-1.

(1) Winter (December 2020 – February 2021)

- Seasonal mean temperatures were below normal in northern Japan and above normal in eastern and western Japan and Okinawa/Amami.
- Seasonal precipitation amounts were significantly above normal on the Sea of Japan side of eastern Japan and in Okinawa/Amami and above normal on the Sea of Japan side of northern Japan. Values were below normal on the Pacific side of northern and eastern Japan and in western Japan.
- Seasonal sunshine durations were significantly above normal in western Japan and above normal in eastern Japan, and below normal on the Sea of Japan side of northern Japan.

Temperatures varied widely between the first and second halves of winter (December 2020 – February 2021). In the first half, some locations experienced record-heavy snowfall due to strong cold-air inflow. Snowfall amounts were significantly above normal on the Sea of Japan side of western Japan and above normal on the Sea of Japan side of eastern Japan. In the second half, cold-air inflow was weak and low-pressure systems

frequently passed over areas near northern Japan. Winter precipitation amounts were significantly above normal on the Sea of Japan side of eastern Japan, which was affected by cold-air inflow in the first half and low-pressure systems in the second half. Winter precipitation amounts were significantly above normal in Okinawa/Amami due to heavy rainfall caused by low-pressure systems. Western Japan was repeatedly influenced by high-pressure systems in the second half of winter. Winter sunshine durations were the highest on record since 1946/47, with 127% of the normal on the Sea of Japan side of western Japan and 119% on the Pacific side.

(2) Spring (March – May 2021)

- Seasonal mean temperatures were significantly above normal nationwide.
- Seasonal precipitation amounts were significantly above normal in northern Japan and on the Pacific Ocean side of western Japan, and above normal in eastern Japan and on the Sea of Japan side of western Japan. Values were below normal in Okinawa/Amami.
- Seasonal sunshine durations were significantly above normal in Okinawa/Amami and above normal on the Pacific side of northern Japan and the Sea of Japan side of eastern Japan.

In spring, mean temperatures were significantly above normal nationwide, mainly due to significantly weak southward cold-air inflow in March. Northern Japan was repeatedly influenced by low-pressure systems and fronts throughout the period, and western Japan was repeatedly influenced by the Meiyu-Baiu front in May. Spring precipitation amounts were significantly above normal in northern Japan and on the Pacific Ocean side of western Japan. In Okinawa/Amami, seasonal sunshine durations were significantly above normal due to the influence of high-pressure systems and diminished influence of the Meiyu-Baiu front. The rainy season started much earlier than normal in many areas of western Japan because the Meiyu-Baiu front moved northward earlier than usual.

(3) Summer (June – August 2021)

- Seasonal mean temperatures were significantly above normal in northern Japan and above normal in eastern Japan.
- Seasonal precipitation amounts were significantly above normal on the Pacific side of eastern Japan and in western Japan and above normal in Okinawa/Amami, and were significantly below normal on the Sea of Japan side of northern Japan.
- Seasonal sunshine durations were significantly above normal in northern Japan and above normal on the Sea of Japan side of eastern Japan, and were below normal in Okinawa/Amami.

In summer, precipitation amounts were significantly above normal on the Pacific side of eastern Japan and in western Japan due to heavy rainfall caused by the Meiyu-Baiu front in early July and heavy rainfall caused by a stagnant front near Honshu in mid-August. Summer sunshine durations and mean temperatures were significantly above normal mainly in the second half of July in northern Japan due to the Pacific High. Summer precipitation amounts were significantly below normal on the Sea of Japan side of northern Japan. In Okinawa/Amami, summer precipitation amounts were above normal and sunshine durations were below normal due to frequent tropical cyclones and typhoons, including the slow-moving Typhoon In-fa near Okinawa at the end of July.

(4) Autumn (September – November 2021)

- Seasonal mean temperatures were above normal in northern and western Japan.
- Seasonal precipitation amounts were above normal on the Sea of Japan side of northern Japan and below normal on the Pacific side of eastern Japan and in western Japan and Okinawa/Amami.
- Seasonal sunshine durations were significantly above normal on the Sea of Japan side of northern Japan and in eastern Japan and Okinawa/Amami, and above normal on the Pacific side of northern Japan and in western Japan.

September and October saw sunny conditions with high-pressure systems over western Japan and suppressed influence from the autumn rain front and typhoons. In November, northern Japan was less susceptible to winter monsoon conditions and more susceptible to low pressure, with warm air flowing in from the south in front of a low-pressure system. As a result, autumn mean temperatures were above normal in northern and western Japan. Autumn precipitation amounts were above normal on the Sea of Japan side of northern Japan and below normal on the Pacific side of eastern Japan and in western Japan and Okinawa/Amami. Autumn sunshine durations were above normal nationwide.

(5) Early Winter (December 2021)

In December 2021, temperatures varied widely across Japan. Monthly precipitation amounts were significantly above normal on the Sea of Japan side of northern Japan and the Pacific side of eastern Japan. Monthly sunshine durations were significantly above normal on the Pacific side of western Japan and in Okinawa/Amami. In late December, strong cold-air inflow from the continent brought heavy snowfall to the Sea of Japan side and elsewhere.

Table 1.2-1 Number of observatories reporting record(include tie record) monthly and annual mean temperatures, precipitation amounts and sunshine durations (2021)

From 153 surface meteorological stations across Japan.

	Temperature		Precipitation amount		Sunshine duration	
	Highest	Lowest	Heaviest	Lightest	Longest	Shortest
January			1		3	1
February	30		1		40	
March	131		4			
April			1		1	
May	7		5			1
June	3		3		3	
July	12		1	9	11	
August			30			
September				1	4	
October				1	1	
November	4		2		15	
December			3		2	
year	187	0	51	11	80	2

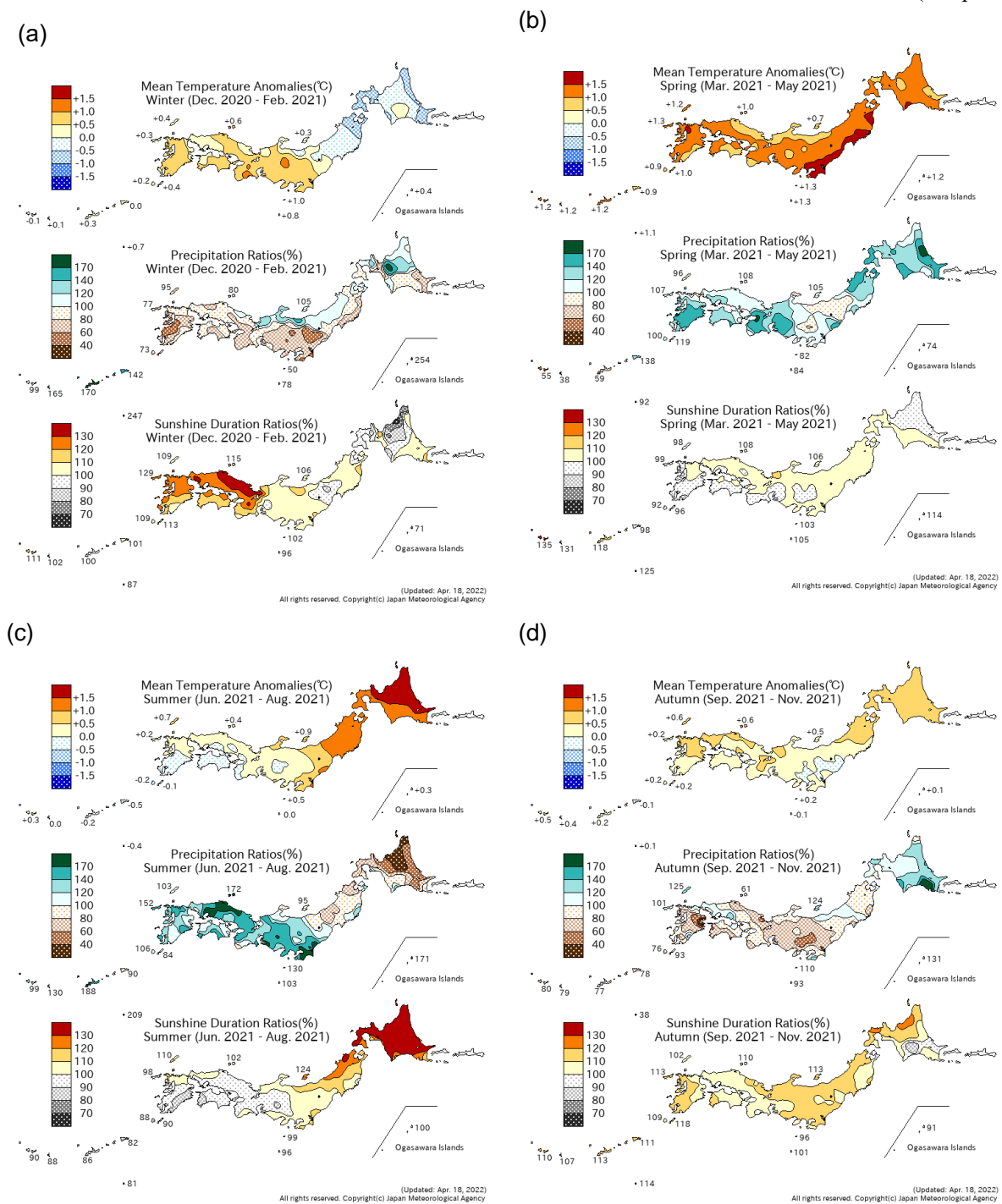


Figure 1.2-3 Seasonal anomalies/ratios for Japan in 2021

(a) Winter (December 2020 to February 2021), (b) spring (March to May 2021), (c) summer (June to August 2021), (d) autumn (September to November 2021). The base period for the normal is 1991 – 2020.

1.3 Atmospheric circulation and oceanographic conditions⁷

- The La Niña event that started in summer 2020 terminated in spring 2021, and is considered responsible for the atmospheric circulation conditions observed in winter 2020/2021.
- The negative phase of an Indian Ocean Dipole (IOD) event was observed from summer to autumn 2021. Convective activity over the Asian summer monsoon region was weaker than normal, but its intraseasonal variation was large.
- The westerly jet stream frequently meandered significantly over the Northern Hemisphere in summer 2021, causing heat waves and heavy precipitation in various places.
- A La Niña-like SST anomaly pattern that re-emerged in autumn 2021 affected atmospheric circulation.

Monitoring of atmospheric and oceanographic conditions (e.g., upper air flow, tropical convective activity, sea surface temperatures (SSTs) and the Asian monsoon) is key to understanding the causes of extreme weather events⁸. This section briefly outlines the characteristics of atmospheric circulation and oceanographic conditions seen in 2021.

1.3.1 Characteristics of individual seasons⁹

(1) Winter (December 2020 – February 2021)

La Niña conditions persisted in the equatorial Pacific from boreal summer 2020 onward. Remarkably positive SST anomalies were observed west of 150°E, and remarkably negative anomalies were observed from 160°E to the central part (Figure 1.3-1 (a)).

Tropical convection was enhanced from the northern Indian Ocean to the Maritime Continent and suppressed around the date line in the equatorial Pacific (Figure 1.3-1 (b)). In the lower troposphere of the tropical region, cyclonic circulation anomalies straddling the equator were seen from the tropical Indian Ocean to the Maritime Continent, and anti-cyclonic circulation anomalies straddling the equator were seen over the western to the central tropical Pacific (Figure 1.3-1 (c)).

In the 500-hPa height field, the polar vortex in the Northern Hemisphere split into a Siberian part and a North American part, with positive anomalies over the northern polar region and negative anomalies over Central and Eastern Siberia (Figure 1.3-1 (d)). A wave train was seen from North America to northern Eurasia, with positive anomalies over northeastern North America and negative anomalies over northwestern Europe. The westerly jet stream shifted northward from its normal position from East Asia to the North Pacific. In the sea level pressure field, positive anomalies were seen from the northern polar region to northwestern Russia, and negative anomalies were seen over northwestern Europe. The southeastward expansion of the Siberian

⁷ See the Glossary for terms relating to sea surface temperature variations and monsoon.

⁸ The main charts used for monitoring of atmospheric circulation and oceanographic conditions are: sea surface temperature (SST) maps representing SST distribution for monitoring of oceanographic variability elements such as El Niño/La Niña phenomena; outgoing longwave radiation (OLR) maps representing the strength of longwave radiation from the earth's surface under clear sky conditions into space or from the top of clouds under cloudy conditions into space for monitoring of convective activity; 850-hPa stream function maps representing air flow in the lower troposphere for monitoring of atmospheric circulation variability elements such as the Pacific High and the monsoon trough associated with the Asian summer monsoon; 500-hPa height maps representing air flow at a height of approximately 5,500 meters for monitoring of atmospheric circulation variability elements such as westerly jet streams and the Arctic Oscillation; sea level pressure maps representing air flow and pressure systems on the earth's surface for monitoring of the Pacific High, the Siberian High, the Arctic Oscillation and other phenomena; 850-hPa temperature maps representing air temperature at a height of approximately 1,500 meters; and temperature calculated from thickness in the troposphere for monitoring of mean temperature of the troposphere.

⁹ JMA publishes Monthly Highlights on the Climate System including information on the characteristics of climatic anomalies and extreme events around the world, atmospheric circulation and oceanographic conditions. It can be found at <https://ds.data.jma.go.jp/tcc/tcc/products/clisys/highlights/index.html>.

High was weaker than normal, and the Aleutian Low shifted northwestward from its normal position (Figure 1.3-1 (e)). Temperatures at 850 hPa were above normal from the northern polar region to northeastern North America and over southeastern Europe, and were below normal over Siberia (Figure 1.3-1 (f)). In the first half of winter 2020/2021, both the polar front and the subtropical jet stream meandered southward over Japan, resulting in strong cold-air-mass flow over the country (Figure 1.1-1-5). The meandering of the subtropical jet stream is attributed to enhanced convective activity over the Maritime Continent associated with the La Niña conditions.

(2) Spring (March – May 2021)

The La Niña event that started in summer 2020 terminated. In the equatorial Pacific, remarkably negative SST anomalies were observed in the central to the eastern part. In the North Pacific, remarkably positive SST anomalies were observed from the western tropical region to the area off the western coast of North America (Figure 1.3-2 (a)).

Tropical convection was enhanced from the northwestern tropical Indian Ocean to northern India, over the western tropical North Pacific and to the east of Hawaii (Figure 1.3-2 (b)). In the lower troposphere of the tropical region, cyclonic circulation anomalies were seen near the Philippines, and anti-cyclonic circulation anomalies were seen over the central tropical South Pacific (Figure 1.3-2 (c)).

In the 500-hPa height field, zonally elongated positive anomalies were seen over the mid-latitude North Pacific, where significant anomalies were observed to the south of the Aleutian Islands. Significantly positive 500-hPa height anomalies were also seen over the eastern Mediterranean Sea (Figure 1.3-2 (d)). The subtropical jet stream from Northern Africa to southern Eurasia was generally weaker than normal. Over the North Pacific, the westerly jet stream shifted northward from its normal position. In the sea level pressure field, zonally elongated positive anomalies were seen over the mid-latitude North Pacific, where significant anomalies were observed to the south of the Aleutian Islands and off the western coast of North America (Figure 1.3-2 (e)). Temperatures at 850 hPa were significantly above normal over the northern Arabian Peninsula and to the east of the Kuril Islands, and were significantly below normal over central Europe (Figure 1.3-2 (f)).

(3) Summer (June – August 2021)

Though ENSO-neutral conditions persisted throughout the season, negative SST anomalies were observed from the central to the eastern part of the equatorial Pacific. The negative phase of an Indian Ocean Dipole (IOD) event emerged with remarkably positive SST anomalies south of Sumatra. Remarkably positive SST anomalies were also observed in the equatorial Atlantic (Figure 1.3-3 (a)).

Tropical convection was enhanced from the area southwest of Sumatra to the Maritime Continent and over the seas south of Japan and the equatorial Atlantic, and was suppressed over the Arabian Sea, from the Bay of Bengal to the Philippines, and over the seas east of New Guinea (Figure 1.3-3 (b)). Convective activity over the Asian summer monsoon region was weaker than normal (Figure 1.3-7). In the lower troposphere of the tropical region, cyclonic circulation anomalies straddling the equator were seen over the eastern tropical Indian Ocean and the tropical Atlantic, and anti-cyclonic circulation anomalies straddling the equator were seen over the western tropical Pacific (Figure 1.3-3 (c)). Intraseasonal variation of the North Pacific Subtropical High (NPSH) was large. Westward expansion of the NPSH over the seas south of Japan was weaker than normal in July, while it was stronger than normal in August causing heavy precipitation around Japan (see News II).

In the 500-hPa height field, the polar vortex in the Northern Hemisphere was stronger than normal. Positive anomalies were seen over the mid-latitudes of North America and the latitude band of 60°N from the

North Atlantic to Eurasia (Figure 1.3-3 (d)). The subtropical jet stream shifted southward from its normal position over Eurasia, and the polar front jet stream was clearly seen over northern Eurasia. The westerly jet stream frequently meandered significantly over the Northern Hemisphere on an intraseasonal timescale, causing heat waves and heavy precipitation in various places (Section 1.1). In the sea level pressure field, positive anomalies were seen from northern Europe to western Russia and around the Kuril Islands, and negative anomalies were widely seen over the northern polar region (Figure 1.3-3 (e)). Development of the Okhotsk High in August caused heavy precipitation in Japan (see News II). Temperatures at 850 hPa were significantly above normal over western North America, around the central Mediterranean Sea, around the Caspian Sea and from Central Siberia to Sakhalin, and were below normal over northern East Asia and the seas north of Alaska (Figure 1.3-3 (f)).

(4) Autumn (September – November 2021)

In the equatorial Pacific, remarkably positive SST anomalies were observed west of 150°E and negative SST anomalies were observed east of 160°E, in particular with remarkably negative anomalies near the date line, indicating La Niña-like SST conditions. The negative phase of the IOD persisted with remarkably positive SST anomalies west of Sumatra (Figures 1.3-4 (a)).

Tropical convection was enhanced from the northern Arabian Sea to the southern Indochina Peninsula and from the southeastern tropical Indian Ocean to the west of New Guinea, and was suppressed from the western to the central equatorial Pacific (Figure 1.3-4 (b)). In the lower troposphere of the tropical region, cyclonic circulation anomalies straddling the equator were seen over the tropical Indian Ocean, and anti-cyclonic circulation anomalies straddling the equator were seen from the western to the central tropical Pacific (Figure 1.3-4 (c)). It is likely that these anomalies were associated with the SST anomalies observed in the equatorial Pacific and the negative phase of the IOD.

In the 500-hPa height field, a wave train was seen from the area to the south of the Aleutian Islands to northern North America, with positive anomalies to the south of the Aleutian Islands and over northern North America and negative anomalies over the Gulf of Alaska (Figure 1.3-4 (d)). It is likely that this wave train was associated with the SST anomalies observed in the equatorial Pacific. Significantly positive 500-hPa height anomalies were also seen to the east of Lake Baikal. The westerly jet stream shifted northward from its normal position to the south of the Aleutian Islands and over the northern North Atlantic. In the SLP field, positive anomalies were seen to the west of Greenland, and negative anomalies were seen from northern Europe to Central Siberia and over a wide area of North America (Figure 1.3-4 (e)). Temperatures at 850-hPa were significantly above normal to the northeast of Lake Baikal and over northern Canada, and were significantly below normal near Alaska (Figure 1.3-4 (f)).

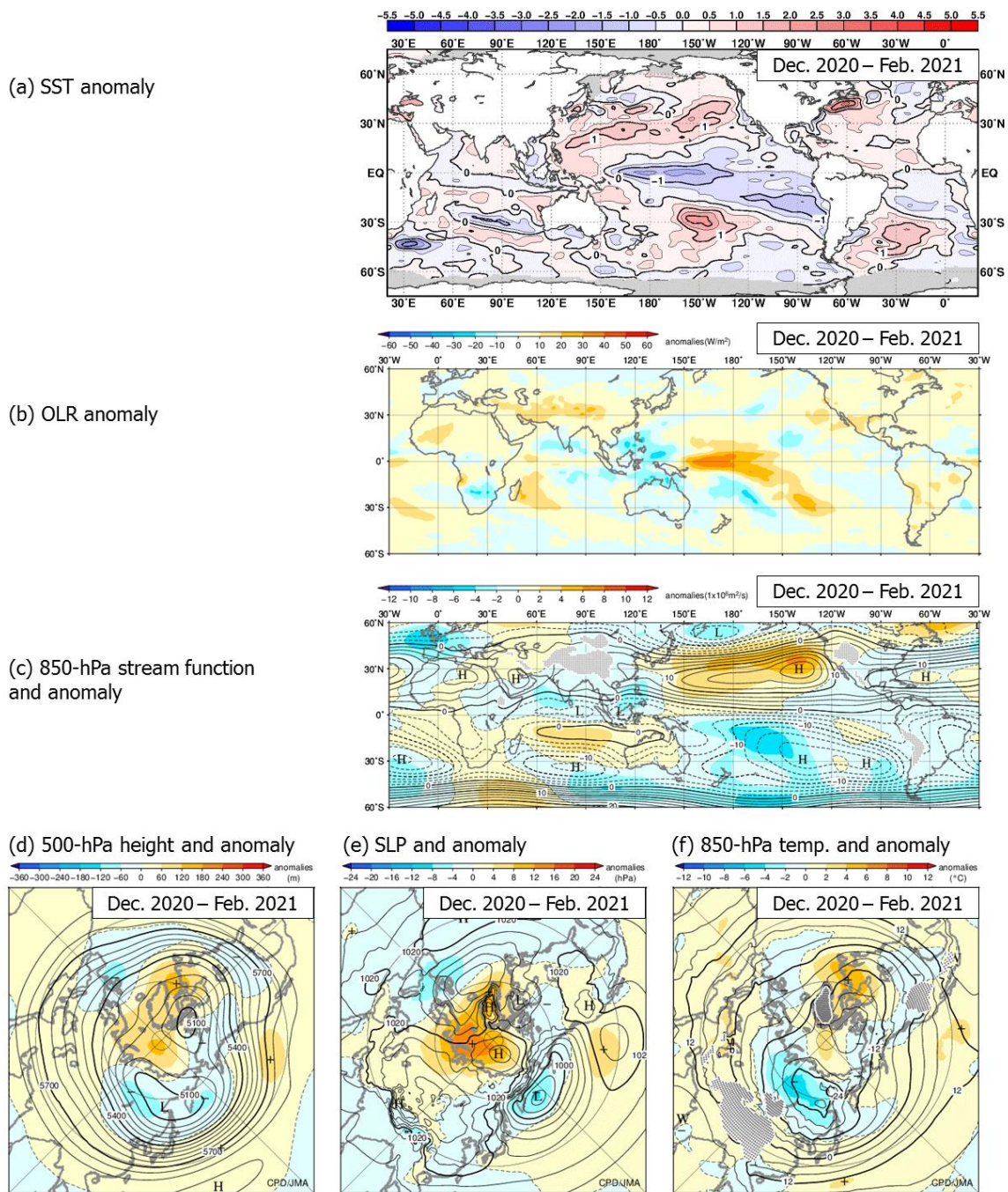
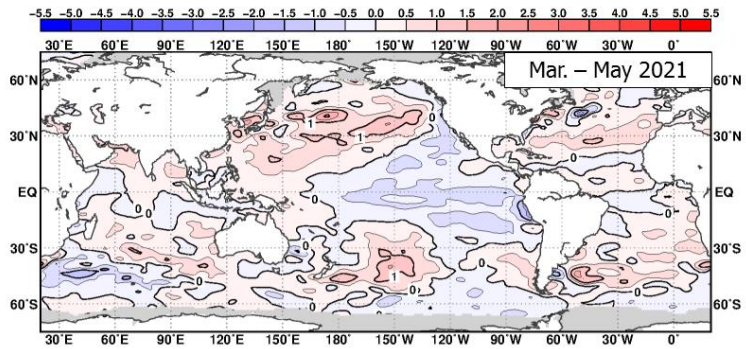


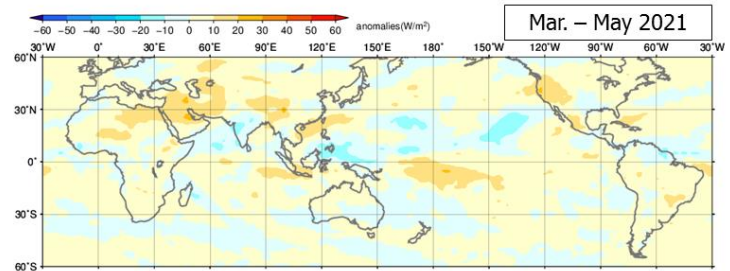
Figure 1.3-1 Three-month mean (a) sea surface temperature (SST) anomaly, (b) outgoing longwave radiation (OLR) anomaly, (c) 850-hPa stream function and anomaly, (d) 500-hPa height and anomaly in the Northern Hemisphere (NH), (e) sea level pressure (SLP) and anomaly in NH, and (f) 850-hPa temperature and anomaly in NH (December 2020 – February 2021)

The base period for the normal is 1991 – 2020. (a) The contour interval is 0.5°C. Sea ice coverage areas are shaded in gray. (b) Negative (cold color) and positive (warm color) OLR anomalies show enhanced and suppressed convection, respectively, compared to the normal. Original data provided by NOAA. (c) The contour interval is $2.5 \times 10^6 \text{ m}^2 \text{ s}$. “H” and “L” denote high- and low-pressure systems, respectively. (d) Contours show 500-hPa height at intervals of 60 m, and shading indicates height anomalies. “H” and “L” denote high- and low-pressure systems, respectively. (e) Contours show sea level pressure at intervals of 4 hPa, and shading indicates sea level pressure anomalies. “H” and “L” denote high- and low-pressure systems, respectively. (f) Contours show temperature at intervals of 4 degree C, and shading indicates temperature anomalies. “W” and “C” denote warm and cold conditions, respectively.

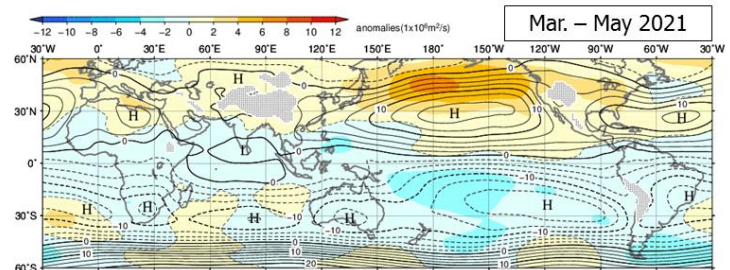
(a) SST anomaly



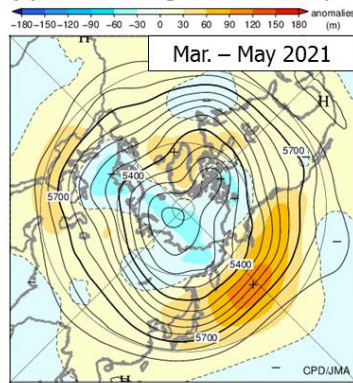
(b) OLR anomaly



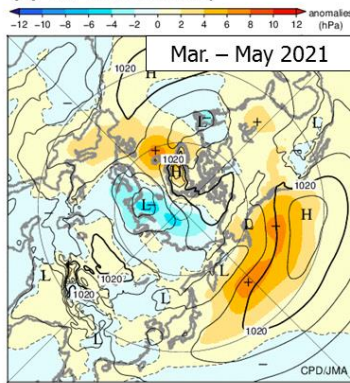
(c) 850-hPa stream function and anomaly



(d) 500-hPa height and anomaly



(e) SLP and anomaly



(f) 850-hPa temp. and anomaly

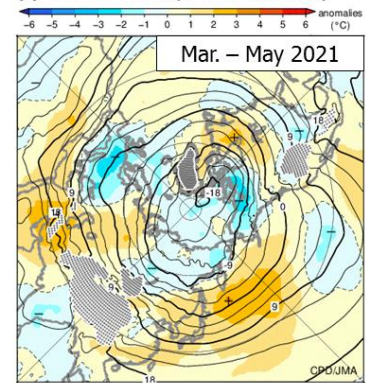
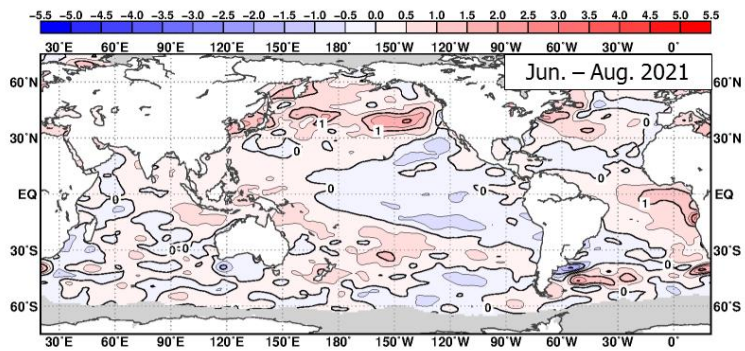


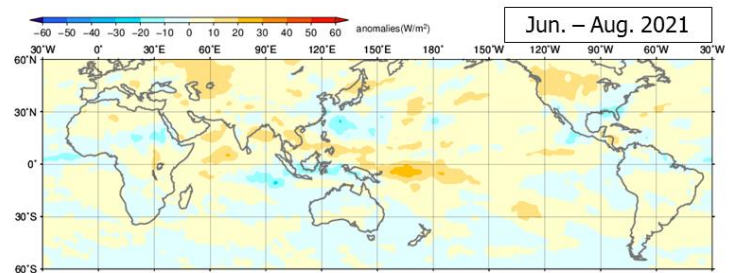
Figure 1.3-2 As per Figure 1.3-1, but for March – May 2021

In (f), contour interval is 3 degree C.

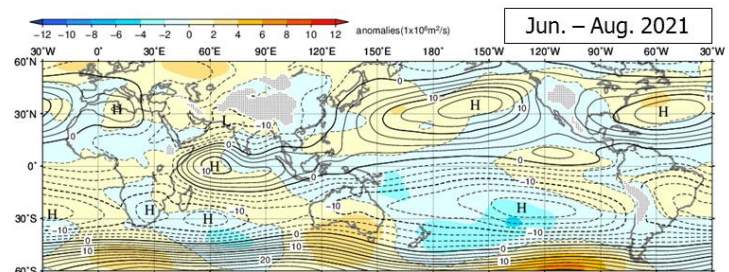
(a) SST anomaly



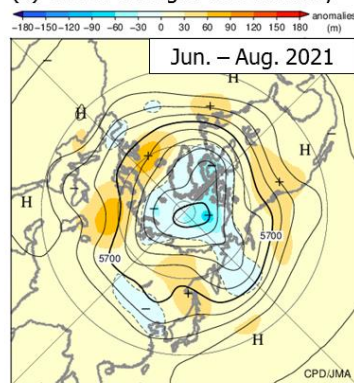
(b) OLR anomaly



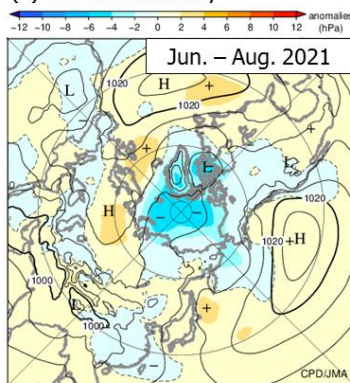
(c) 850-hPa stream function and anomaly



(d) 500-hPa height and anomaly



(e) SLP and anomaly



(f) 850-hPa temp. and anomaly

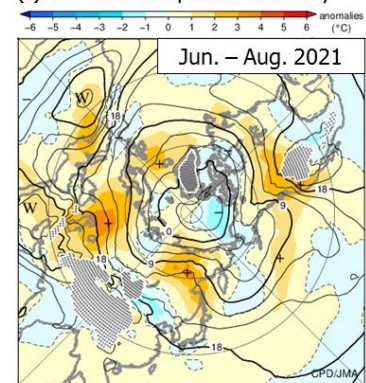
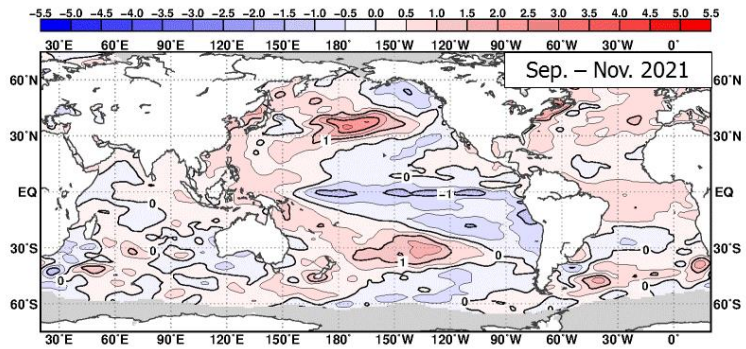


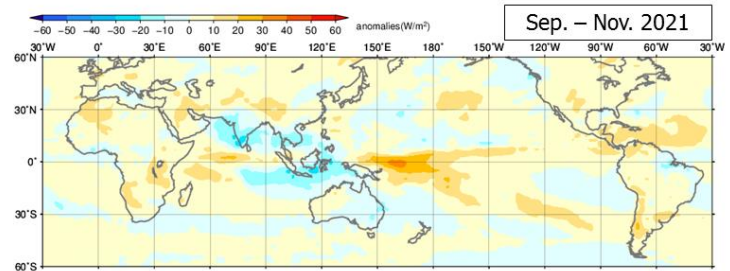
Figure 1.3-3 As per Figure 1.3-1, but for June – August 2021

In (f), contour interval is 3 degree C.

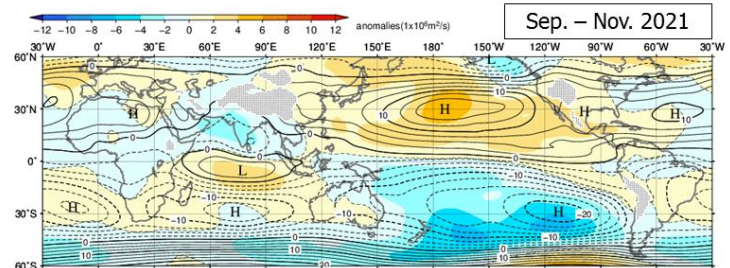
(a) SST anomaly



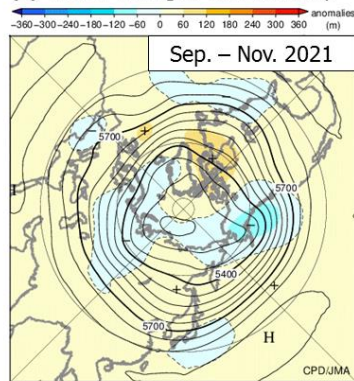
(b) OLR anomaly



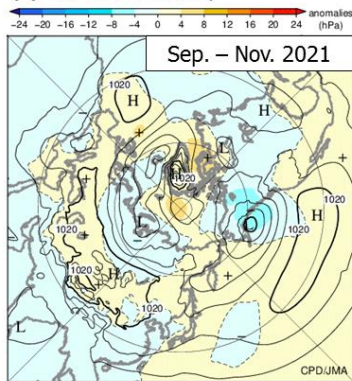
(c) 850-hPa stream function and anomaly



(d) 500-hPa height and anomaly



(e) SLP and anomaly



(f) 850-hPa temp. and anomaly

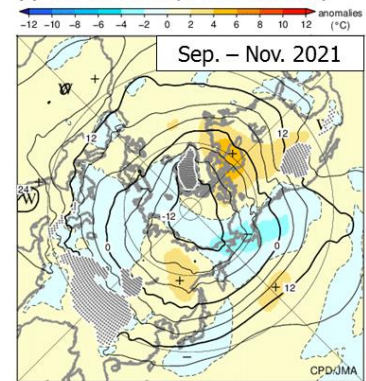


Figure 1.3-4 As per Figure 1.3-1, but for September – November 2021

1.3.2 Global average temperature in the troposphere

Although the global average temperature in the troposphere (Figure 1.3-5) remained higher than normal for most of 2020, it began to drop in winter 2020/2021 and fell to the normal level in spring 2021. It began to increase again thereafter, and the value in October 2021 was the second highest on record for the month since 1958 (see also Figure 1.3-6).

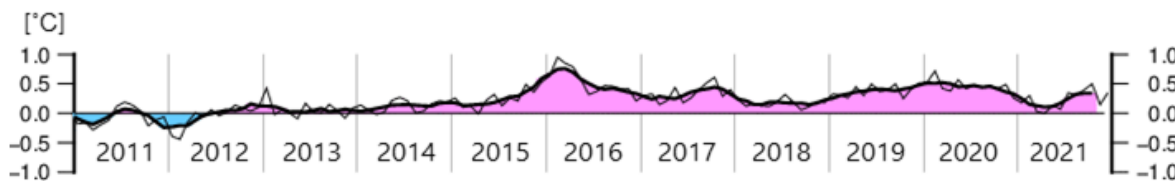


Figure 1.3-5 Time-series representation of global average temperature anomalies calculated from thickness in the troposphere (2011 to 2021)

The thin and thick lines show monthly mean and five-month running mean values, respectively. The base period for the normal is 1991 – 2020.

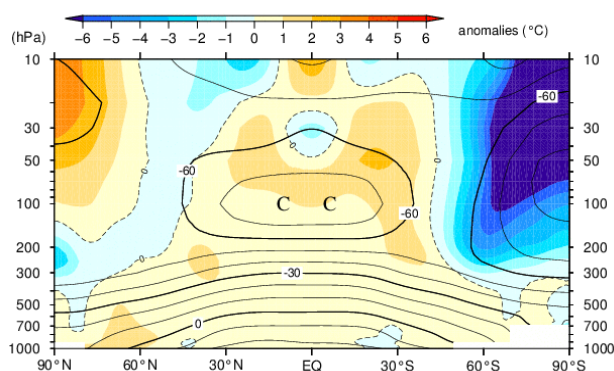


Figure 1.3-6 Latitude-height cross section of zonal mean temperature and anomaly (October 2021)

Contours show zonal mean temperature at intervals of 10 degree C, and shading indicates temperature anomalies. The base period for the normal is 1991 – 2020. “W” and “C” denote warm and cold conditions, respectively.

1.3.3 Asian summer monsoon

Convection during the 2021 Asian summer monsoon season (June – September) was generally suppressed, as indicated by the OLR index (SAMOI (A))¹⁰, JMA, 1997; Figure 1.3-7). In particular, it is likely that the remarkably suppressed convection observed in August caused a significant southward shift of the subtropical jet stream over Eurasia and resulted in persistent heavy precipitation over Japan in association with an unusually stationary front in the middle of summer.

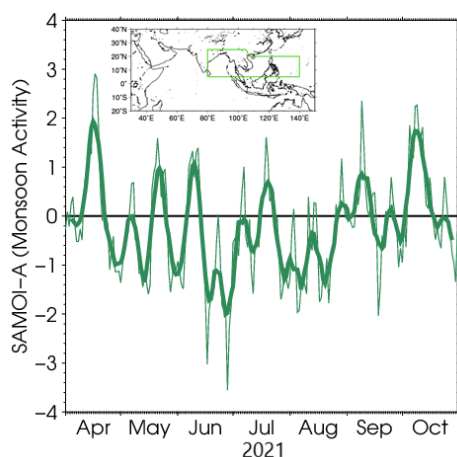


Figure 1.3-7 Time-series representation of the Asian summer monsoon OLR index (SAMOI (A)) (April – October 2021)

The thin and thick green lines indicate daily and seven-day running mean values, respectively. SAMOI (A) indicates the overall activity of the Asian summer monsoon, and positive and negative values indicate enhanced and suppressed convective activity, respectively, compared to the normal. The base period for the normal is 1991 – 2020. Original OLR data provided by NOAA.

¹⁰ SAMOI (A) is defined as reversed-sign area-averaged OLR anomalies normalized by its standard deviation. The area for average is enclosed by green line in the map of Figure 1.3-7.

1.3.4 Tropical cyclones over the western North Pacific and the South China Sea

In 2021, 22 tropical cyclones (TCs) with maximum wind speeds of ≥ 34 kt formed over the western North Pacific and the South China Sea (Figure 1.3-8, Table 1.3-1), which was below the normal of 25.1 (1991 – 2020 average). In particular, during August and September when the number of TC formations is at its highest, convective activity was low over ocean areas where many TCs form climatologically. A total of 8 TCs formed during this period, which was below the normal of 10.7. The lower number of formations during the peak period may have contributed to the reduced annual total.

A total of 12 TCs came within 300 km of the Japanese archipelago, which was similar to the normal of 11.7. A total of 3 of these made landfall on Japan. Among them, Tropical Storm Nepartak was the first to make landfall on Miyagi Prefecture and the second to make landfall on the Pacific side of the Tohoku region, following Tropical Storm Lionrock in 2016. Typhoon Chanthu was the first to make landfall on Fukuoka Prefecture since records began in 1951.

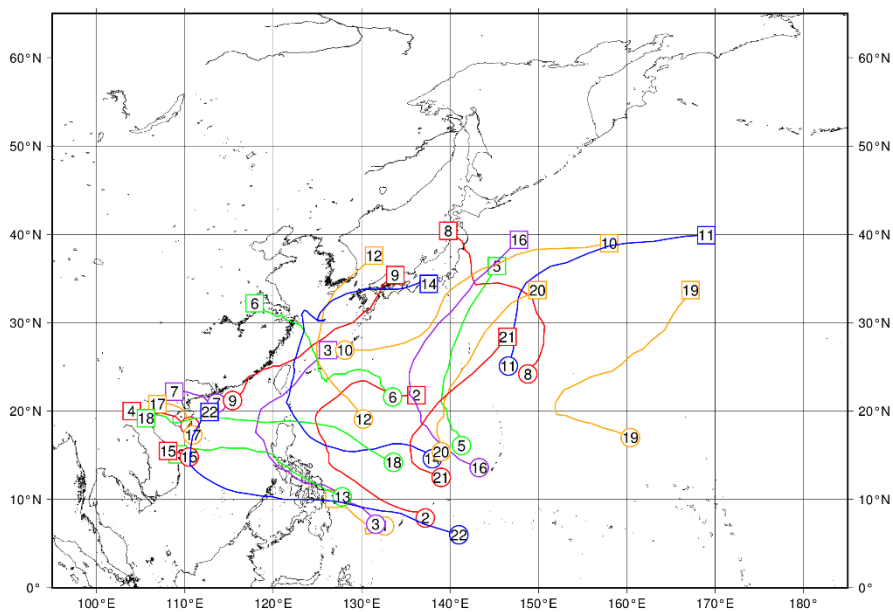


Figure 1.3-8 Tracks of TCs with maximum wind speeds of ≥ 34 kt in 2021

Numbered circles indicate positions of the TC formed (maximum wind speeds of ≥ 34 kt), and numbered squares indicate positions of the TC dissipated (maximum wind speeds lower than 34 kt). Source: RSMC Tokyo-Typhoon Center data

Table 1.3-1 TCs with maximum wind speeds of ≥ 34 kt in 2021 (Source: RSMC Tokyo-Typhoon Center data)

Number ID	Tropical Cyclone	Duration (UTC)	Maximum Wind ¹⁾ (kt)	Number ID	Tropical Cyclone	Duration (UTC)	Maximum Wind ¹⁾ (kt)
2101	DUJUAN	0000, 18 Feb - 1200, 21 Feb	40	2112	OMAIS	1200, 20 Aug - 0000, 24 Aug	45
2102	SURIGAE	1800, 13 Apr - 0000, 25 Apr	120	2113	CONSON	0000, 06 Sep - 1800, 11 Sep	50
2103	CHOI-WAN	1800, 30 May - 0600, 05 Jun	40	2114	CHANTHU	1200, 06 Sep - 0600, 18 Sep	115
2104	KOGUMA	1800, 11 Jun - 0600, 13 Jun	35	2115	DIANMU	0600, 23 Sep - 1800, 23 Sep	35
2105	CHAMPI	0000, 23 Jun - 1800, 27 Jun	65	2116	MINDULLE	1200, 23 Sep - 0000, 02 Oct	105
2106	IN-FA	1200, 17 Jul - 1800, 27 Jul	85	2117	LIONROCK	1800, 07 Oct - 0600, 10 Oct	35
2107	CEMPAKA	1800, 18 Jul - 0000, 22 Jul	70	2118	KOMPASU	0000, 08 Oct - 1200, 14 Oct	55
2108	NEPARTAK	1200, 23 Jul - 0600, 28 Jul	40	2119	NAMTHEUN	0000, 10 Oct - 0000, 17 Oct	50
2109	LUPIT	0000, 04 Aug - 0000, 09 Aug	45	2120	MALOU	1800, 24 Oct - 1200, 29 Oct	75
2110	MIRINAE	0600, 05 Aug - 0000, 10 Aug	50	2121	NYATOH	0000, 30 Nov - 0000, 04 Dec	100
2111	NIDA	0000, 04 Aug - 0000, 08 Aug	55	2122	RAI	0600, 13 Dec - 1800, 20 Dec	105

1) Estimated maximum 10-minute mean wind speed

Chapter 2 Climate Change

2.1 Greenhouse gases^{11,12}

- Atmospheric concentrations of carbon dioxide are increasing.
- Atmospheric concentrations of methane have shown an ongoing increase (with the exception of a stationary phase from 1999 to 2006).
- Atmospheric concentrations of nitrous oxide are increasing.
- Among halocarbons, atmospheric concentrations of chlorofluorocarbons are decreasing, while those of hydrofluorocarbons are increasing.

JMA operates the World Data Centre for Greenhouse Gases (WDCGG)¹³ to collect, maintain and provide data on greenhouse gases for related monitoring on a global scale under the Global Atmosphere Watch (GAW) Programme of the World Meteorological Organization (WMO). Analysis of data reported to WDCGG shows that the global mean concentration of greenhouse gases with strong impacts on global warming (in particular, carbon dioxide (CO₂), methane (CH₄) and nitrous oxide (N₂O)) continues to increase (Table 2.1-1).

In Japan, JMA monitors surface-air concentrations of greenhouse gases via three observation stations at Ryori in Ofunato, Minamitorishima in the Ogasawara Islands and Yonagunijima in the Nansei Islands. JMA research vessels are used to observe oceanic and atmospheric CO₂ in sea areas near Japan and in the western North Pacific. In addition, sampling of greenhouse gases in upper-air areas using cargo aircraft was commenced in 2011 (Figure 2.1-1).

Table 2.1-1 Atmospheric concentrations of major greenhouse gases (2020)¹⁴

	Atmospheric mole fraction			Absolute increase from 2019	Relative increase from 2019	Lifetime
	Pre-industrial level around 1750	Global mean in 2020	Relative increase from Pre-industrial level			
Carbon dioxide	About 278 ppm	413.2 ppm	+ 49 %	+2.5 ppm	+0.61 %	-
Methane	About 729 ppb	1,889 ppb	+159 %	+11 ppb	+0.59 %	11.8 years
Nitrous oxide	About 270 ppb	333.2 ppb	+ 23 %	+1.2 ppb	+0.36 %	109 years

¹¹ Part of this section shows observational outcomes for the period until 2020, as greenhouse gas observation data for 2021 were not yet fully available at the time of publication.

¹² Information on greenhouse gas monitoring is published on JMA's website.
https://www.data.jma.go.jp/ghg/info_ghg_e.html (Atmospheric greenhouse gases)

¹³ See the WDCGG website for more information.
<https://gaw.kishou.go.jp/>

¹⁴ Data on the annual mean mole fraction in 2020 and its absolute and relative differences from the previous year are from WMO (2021), while data on pre-industrial levels and lifetime are from IPCC (2021). The lifetime of gas as referred to here describes the time scale over which a local instantaneous increment of gas decays. The increase from pre-industrial levels is calculated from mole fractions for the pre-industrial era and 2020.

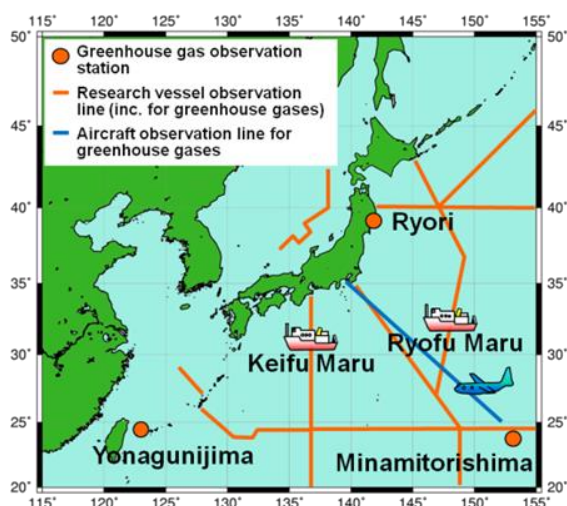


Figure 2.1-1 JMA's greenhouse gas observation network

Observation stations at Ryori, Minamitorishima and Yonagunijima and regular monitoring routes of research vessel and cargo aircraft

2.1.1 Concentration of carbon dioxide

(1) Concentration of global atmospheric carbon dioxide

The global mean concentration of atmospheric CO₂ shows a trend of increase with ongoing seasonal variations (Figure 2.1-2 (a)), primarily due to influences associated with human activity such as fossil fuel combustion and deforestation. Some anthropogenic CO₂ is absorbed by the terrestrial biosphere and the oceans, while the rest remains in the atmosphere. As most major sources of CO₂ are located in the Northern Hemisphere, concentrations tend to be higher in the mid- and high latitudes there and lower in the Southern Hemisphere (Figure 2.1-3).

The seasonal variability of CO₂ concentration is generally attributable to terrestrial biosphere activity. In summer, active plant photosynthesis consumes masses of CO₂, while emissions from plant respiration and organic-matter decomposition become dominant in winter. As a result, the annual maximum concentration is observed from March to April in the Northern Hemisphere and from September to October in the Southern Hemisphere. Seasonal variations exhibit larger amplitudes in the mid- and high latitudes of the Northern Hemisphere than in the ocean-rich Southern Hemisphere (Figure 2.1-3). Accordingly, the global mean CO₂ concentration usually peaks around April, reflecting the seasonal variations of the Northern Hemisphere.

WDCGG analysis shows that global mean surface CO₂ concentration increased by 2.5 ppm from 2019 to 2020, reaching as much as 413.2 ppm (Table 2.1-1). The most recent 10-year average annual growth rate is 2.4 ppm/year, as opposed to the corresponding value of 1.5 ppm/year for the 1990s.

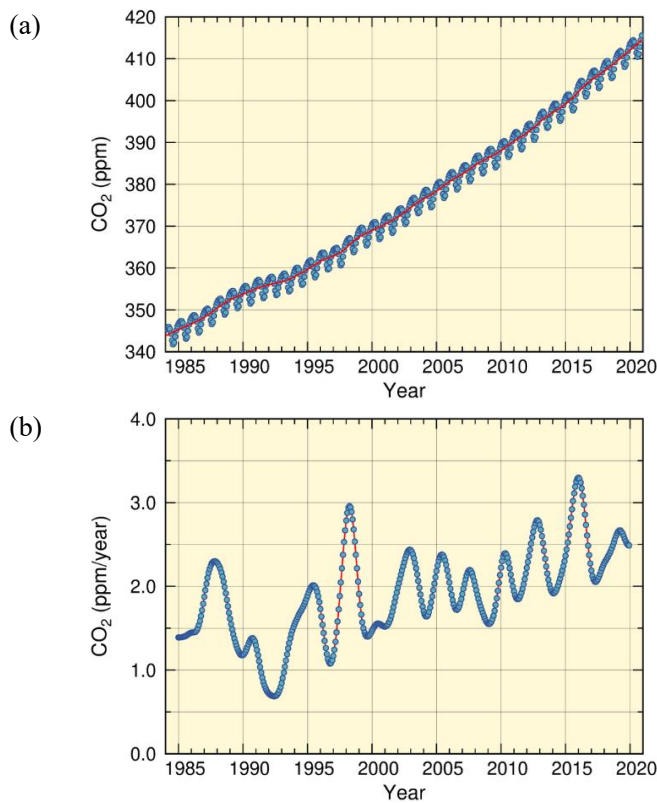


Figure 2.1-2 Global mean concentration of atmospheric CO₂ (a) and annual growth rate (b)
 In the upper panel the blue dots are monthly values, and the red line represents the corresponding sequence after removal of seasonal variations. From the latter, the growth rate is derived and shown in the lower panel. Graph content is based on analysis of observation data reported to WDCGG using the method of WMO (2009). Data contributors are listed in WMO (2022).

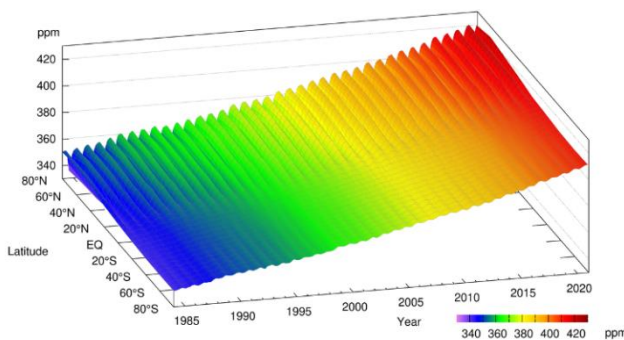


Figure 2.1-3 Latitudinal distribution of atmospheric CO₂ concentrations
 The data set and analysis method are as per Figure 2.1-2.

The growth rate of CO₂ concentration exhibits significant interannual variations (Figure 2.1-2 (b)). Major increases in concentration often coincide with El Niño events, largely because the terrestrial biosphere emits more CO₂ than usual under such conditions. In particular, El Niño events bring about high temperatures and droughts in tropical areas and elsewhere, thereby promoting plant respiration and organic-matter decomposition in soil and hindering plant photosynthesis (Keeling *et al.*, 1995; Dettinger and Ghil, 1998).

Figure 2.1-4 illustrates net CO₂ uptake by the terrestrial biosphere as estimated using the method of Le Quéré *et al.* (2016). Here, CO₂ uptake is defined as the amount of anthropogenic emissions minus the increment of atmospheric concentration and the amount of uptake by oceans. The low uptake by the terrestrial biosphere in 2015 and 2016 is generally attributed to the 2014 – 2016 El Niño event (WMO, 2018b). The annual net CO₂ uptakes in 2015 and 2016 were both lower than the 10-year average of 2.6 ± 1.2 GtC/year for the period 2010 – 2019. Similar suppression of net CO₂ uptake was observed in association with the El Niño events of 1997/1998 and 2002/2003. An exception was observed from 1991 to 1992, when net CO₂ uptake by the terrestrial biosphere was large despite the presence of an El Niño event. This is attributable to the eruption of Mt. Pinatubo in June 1991, which triggered worldwide low temperatures and inhibited CO₂ emissions from organic-matter decomposition in soil (Keeling *et al.*, 1996; Rayner *et al.*, 1999).

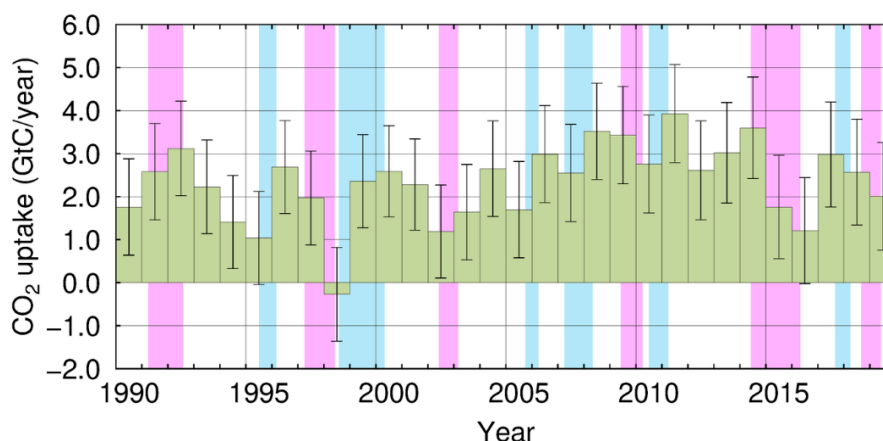


Figure 2.1-4 Annual net CO₂ uptake by the terrestrial biosphere

In this analysis, the net CO₂ uptake is estimated by subtracting the annual increment of atmospheric CO₂ and the amount of uptake by oceans from the amount of anthropogenic emissions. The amount of anthropogenic emissions stemming from fossil fuel combustion, cement production (including cement carbonation sinks) and land-use change is based on Friedlingstein *et al.* (2021). The annual increment of atmospheric CO₂ is the annual mean of the monthly means shown in Figure 2.1-2 (b). Oceanic uptake is based on Iida *et al.* (2021; see also Section 2.12.1 (2)), and incorporates emissions associated with the natural carbon cycle, corresponding to 0.6 GtC/year (IPCC, 2021). Error bars indicate 68% confidence levels. El Niño and La Niña periods are shaded in red and blue, respectively. A negative CO₂ uptake equates to an emission.

(2) Concentration of atmospheric carbon dioxide in Japan

Concentrations of atmospheric CO₂ at all three of Japan's observation stations have shown a continuous increase along with seasonal variations (Figure 2.1-5 (a)). The amplitude of these variations is greater at Ryori than at the other stations because it tends to be larger in higher latitudes of the Northern Hemisphere in association with significant seasonal variations in terrestrial biosphere activity in the mid- and high latitudes (see Figure 2.1-1). Although Yonagunijima and Minamitorishima have similar latitudes, the former tends to observe higher concentrations and seasonal variations with larger amplitudes because of its greater proximity to the Asian continent, which is characterized by major anthropogenic emissions and an extensive biosphere. The annual mean CO₂ concentration in 2021 was 419.5 ppm at Ryori, 416.9 ppm at Minamitorishima and 419.2 ppm at Yonagunijima (based on preliminary estimations). The increase from the previous year was 2.0 to 3.2 ppm/year, which is comparable to the mean annual absolute increase over the last 10 years. It has been reported that fossil fuel-related emissions of carbon dioxide in 2020 decreased by about 5.4% from 2019 due to COVID-19 restrictions, while those for 2021 are expected to increase by about 4.9% from 2020 (Friedlingstein *et al.*, 2021). Concentrations of atmospheric CO₂ also continue to increase (see also News I).

Figure 2.1-5 (b) shows growth rates of CO₂ concentrations observed at the three observation stations. High rates have been observed in most cases during the periods of El Niño events. As a recent example, a sharp increase in CO₂ concentration was observed in association with the event that ran from summer 2014 to spring 2016.

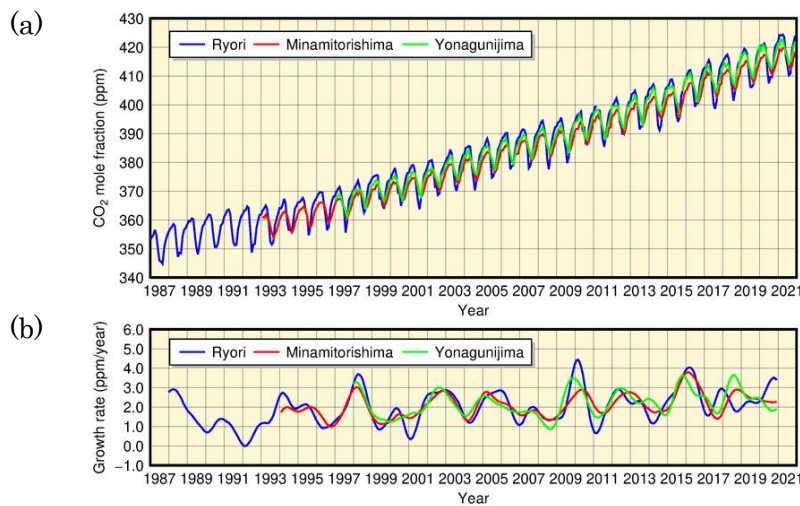


Figure 2.1-5 Monthly mean concentrations (a) and corresponding growth rates (b) of atmospheric CO₂ observed at Ryori (blue), Minamitorishima (red) and Yonagunijima (green)
The method used to calculate the growth rate is described in WMO (2009).

(3) Concentration of carbon dioxide in the upper air

Since 2011, JMA has monitored upper-air CO₂ concentrations using cargo aircraft with support from Japan Ministry of Defense, with air samples taken along the route from Atsugi Air Base (35.45°N, 139.45°E) to Minamitorishima Island (24.29°N, 153.98°E) during level flight at an altitude of approximately 6 km and during descent¹⁵ to the island once a month (Tsuboi *et al.*, 2013; Niwa *et al.*, 2014).

Figure 2-1.6 shows measured and averaged concentrations for samples collected during level flight in black and blue dots, respectively. Monthly mean concentrations at the ground-based station on the island are also shown in red. The dashed curves in blue and red represent components after removal of seasonal cycles for aircraft and Minamitorishima, respectively. Concentrations exhibit a gradual increase over time in the upper air as well as on the surface, although values tend to be lower in the former.

Figure 2-1.7 shows the vertical dependence of average seasonal cycles based on air samples collected during descent in addition to level-flight data and ground-based data. To allow direct comparison, these monthly values are calculated by averaging concentrations after removal of long-term trends in surface observation data. At each level, the information shows similar seasonal variations with higher values from winter to spring and lower values from summer to fall, while significant vertical dependence with lower values toward higher altitudes is observed from winter to spring. Consequently, the amplitude of seasonal cycles is smaller in the upper air.

Figure 2-1.8 shows concentrations for samples taken during descent minus the daily mean value recorded at the ground-based station on the flight date for February (left) and August (right). While concentrations are lower toward higher altitudes in February, there is no clear vertical dependence in August.

The above results suggest that parts of surface air affected by the terrestrial biosphere in continental regions are transported to the ground and upper levels of the island, and that air transport behavior varies with seasons and altitudes. The characteristic of strong vertical dependence from winter to spring and weak dependence from summer to fall is also identified in data from other aircraft observations around North America and Asia (Sweeney *et al.*, 2015; Umezawa *et al.*, 2018).

¹⁵ Although some air samples are taken during ascent flights from Minamitorishima Island, all vertical samplings are referred to here as descent samplings.

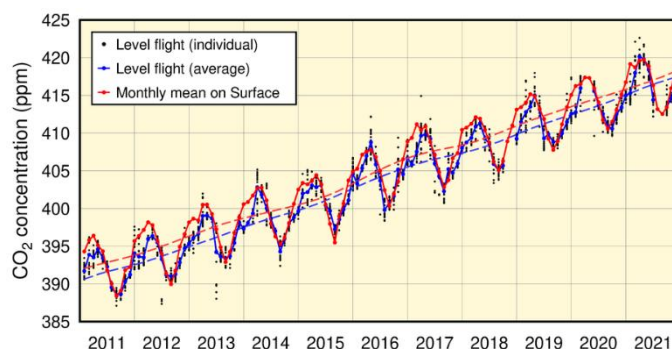


Figure 2.1-6 Measured and averaged CO₂ concentrations for air samples collected during level flight (at a height of approx. 6 km) of cargo aircraft along the route from Atsugi Air Base to Minamitorishima (black and blue dots, respectively) and monthly mean concentrations at the Minamitorishima ground-based station (red dots). Blue and red dashed lines represent components after the removal of seasonal cycles from the series of blue and red dots, respectively. The analysis is based on WMO (2009).

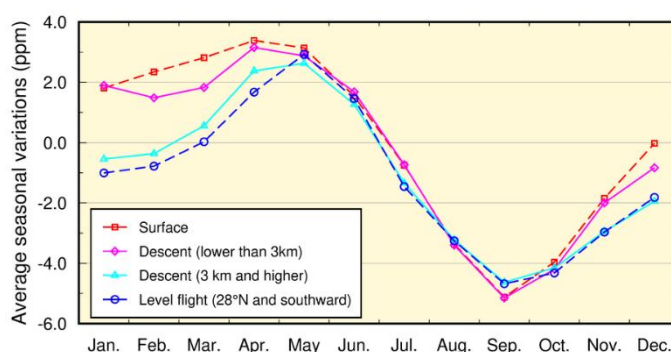


Figure 2.1-7 Vertical dependence of average seasonal cycles around Minamitorishima for monthly mean concentrations on the surface (red), concentrations for air samples taken during level flight at latitudes 28°N and southward (blue), and those taken during descent with altitudes less than 3 km (magenta) and otherwise (cyan). Monthly values are calculated by averaging concentrations after removal of long-term trends (components without seasonal cycles) for surface observation data (the red dashed line in Figure 2.1-6).

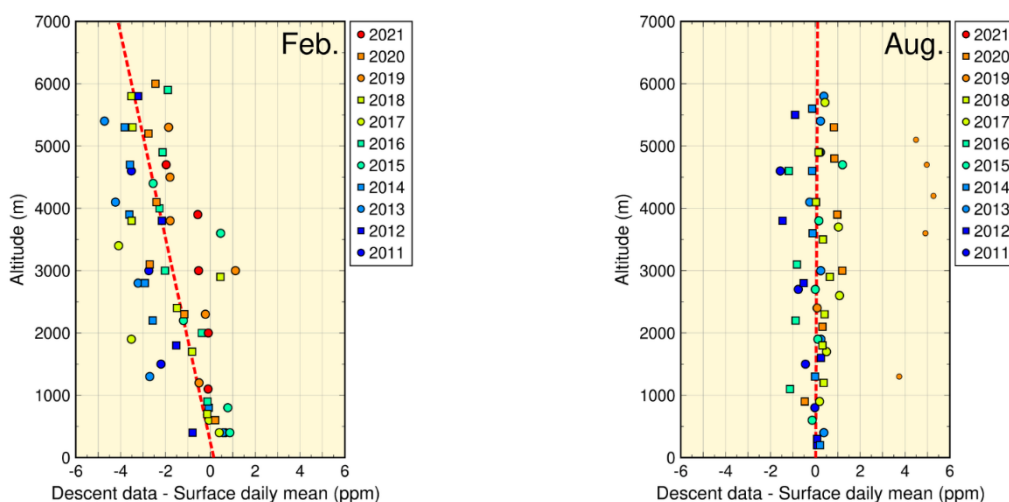


Figure 2.1-8 Vertical variations of CO₂ concentrations over Minamitorishima. Circles and squares show concentrations of air samples taken during descent to the island minus the daily mean value recorded at the ground-based station on the flight date. Symbol colors and shapes represent observation years. Dashed red lines show the vertical gradient of the symbols as determined using the least squares method. To determine representative characteristics for the observation area, outlier data (small symbols) beyond the 3 sigma of the residual standard deviation from the fitted line are excluded from calculation for the vertical gradient. On the flight date in August 2019, daily mean concentration on the surface was 4 – 5 ppm lower than that during descent because continental air masses with low CO₂ concentrations were transported to areas near the ground around Minamitorishima. It should be noted that observations for August 2021 were missing.

2.1.2 Concentration of methane

(1) Concentration of global atmospheric methane

The global mean concentration of atmospheric CH₄ has been increasing since at least the mid-1980s when worldwide monitoring began, except for a stationary phase from 1999 to 2006 (Figure 2.1-9). IPCC (2021) reported that anthropogenic emissions from the oil and gas sectors declined through the 1990s, and that concurrent emission changes from fossil fuels and the agricultural sector may be responsible for the greater concentrations observed since 2007. Meanwhile, large uncertainties still remain in relation to CH₄ emissions from wetlands and biomass combustion driven by El Niño Southern Oscillation and variations in hydroxyl radicals¹⁶, which contribute to CH₄ destruction.

WDCGG analysis shows that the global mean concentration of CH₄ in 2020 was 1,889 ppb, which is the highest since records began (Table 2.1-1).

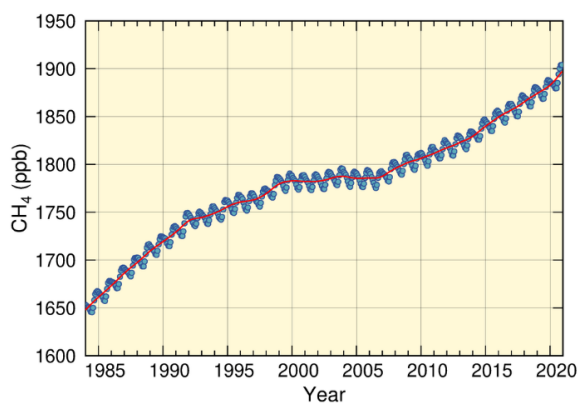


Figure 2.1-9 Global mean concentration of atmospheric CH₄

The blue dots are monthly values, and the red line represents the corresponding sequence after the removal of seasonal variations. Graph content is based on analysis of observation data reported to WDCGG based on the method of WMO (2009). Data contributors are listed in WMO (2022).

Figure 2.1-10 shows the latitudinal dependence of CH₄ concentrations. Values are lower in the tropics than in the high and mid-latitudes of the Northern Hemisphere because CH₄ is mostly emitted from land areas in the Northern Hemisphere, and disappears due to reaction with hydroxyl radicals over tropical oceans during transportation to the Southern Hemisphere. In summer, more CH₄ is destroyed because more hydroxyl radicals are produced as a result of enhanced ultraviolet radiation and water vapor. This reaction contributes to seasonal variations of CH₄ concentrations in both hemispheres, with lower values in summer and higher values in winter (Figures 2.1-9 and 2.1-10).

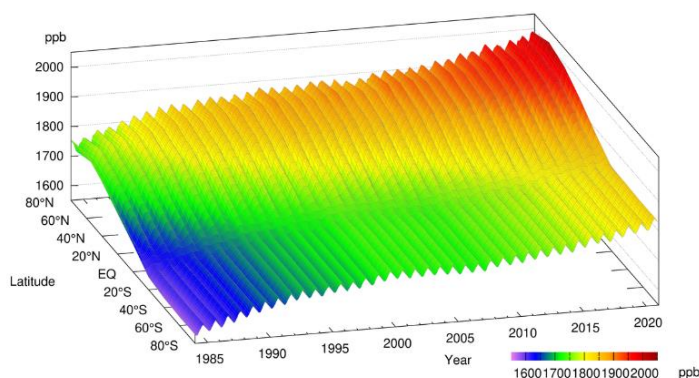


Figure 2.1-10 Latitudinal distribution of atmospheric CH₄ concentrations

The data set and analysis method are as per Figure 2.1-9.

¹⁶ Hydroxyl radicals are highly reactive chemicals generated by the reaction of atomic oxygen, which is derived from UV photolysis of ozone, with airborne water vapor. It is particularly abundant at low latitudes, where UV radiation is strong and water vapor is plentiful.

The remarkable increase observed in global mean atmospheric concentrations of CH₄ since the industrial era (+159%) has been much more rapid than that of CO₂ (+49%) (Table 2.1-1). This is partly because around 40% of CH₄ released into the atmosphere is of natural origin (wetlands, termites, etc.) and around 60% is from human-related activity sources (ruminants, rice paddies, fossil fuel mining, landfill, biomass burning, etc.), and anthropogenic emissions of CH₄ exceed natural emissions. The long-term trend of CH₄ concentration depends on various factors of uncertainty, including anthropogenic/natural emissions and chemical reactions. Accordingly, further development of the global CH₄ observation network is required.

(2) Concentration of atmospheric methane in Japan

Atmospheric CH₄ concentrations at all of Japan's three observation stations exhibit a trend of increase with seasonal variations in the same way as the global mean concentration (Figure 2.1-11 (a)). Ryori usually observes the highest concentration among the three stations because it is located in the northern part of Japan, where CH₄ sources in the Asian continent are more influential and reaction with hydroxyl radicals is less marked. Although Yonagunijima and Minamitorishima are located at similar latitudes, the former tends to record higher concentrations in winter because CH₄ sources on the Asian continent have a stronger impact there in winter as a result of continental air mass expansion. In summer, meanwhile, a hydroxyl radical-rich maritime air mass covers both stations, and similarly low concentrations are observed. Since 2010, Yonagunijima has occasionally observed concentrations as high as those of Ryori in winter. The annual mean CH₄ concentration in 2021 was 1,983 ppb at Ryori, 1,931 ppb at Minamitorishima and 1,950 ppb at Yonagunijima, all of which are the highest on record (based on preliminary estimations).

The growth rate of atmospheric CH₄ concentration exhibits interannual variations that differ significantly from station to station (Figure 2.1-11 (b)).

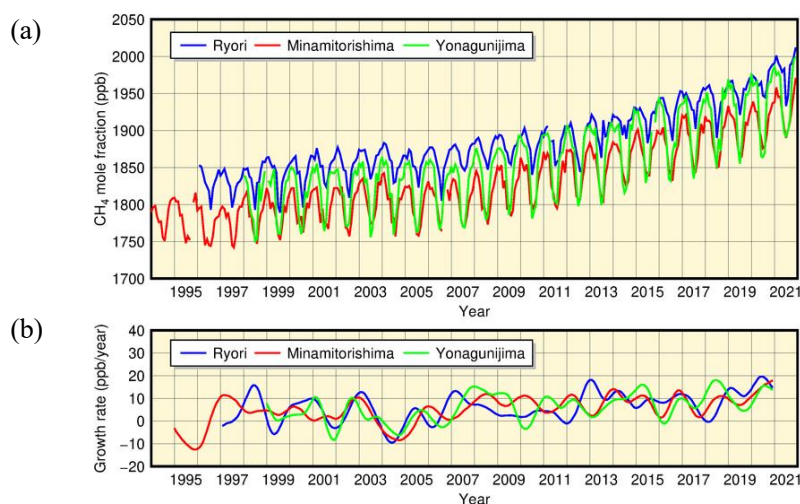


Figure 2.1-11 Monthly mean concentrations (a) and corresponding growth rates (b) of atmospheric CH₄ observed at Ryori (blue), Minamitorishima (red) and Yonagunijima (green)
The method for calculating the growth rate is described in WMO (2009).

2.1.3 Concentration of nitrous oxide

Figure 2.1-12 shows that the global mean concentration of atmospheric N₂O has been continuously increasing. The annual mean concentration in 2020 was 333.2 ppb, which was 23% above the pre-industrial level of 270 ppb (Table 2.1-1). Around 60% of N₂O released into the atmosphere is of natural origin (oceans, soil, etc.), and around 40% is from human activity-related sources (biomass burning, nitrate fertilizers, various industrial processes, etc.). Seasonal variations of N₂O concentrations are lower than those of CO₂ and CH₄ because N₂O has a longer lifetime (109 years). The hemispheric mean concentration is approximately 1 ppb higher in the Northern Hemisphere than in the Southern Hemisphere (Figure 2.1-13) because there are more sources of

anthropogenic emissions in the former. This interhemispheric difference is, however, much smaller than those observed with CO₂ and CH₄.

The atmospheric N₂O concentration at Ryori exhibits characteristics similar to those of the global mean (Figure 2.1-14). The annual mean concentration in 2021 at Ryori was 336.7 ppb (based on preliminary estimations).

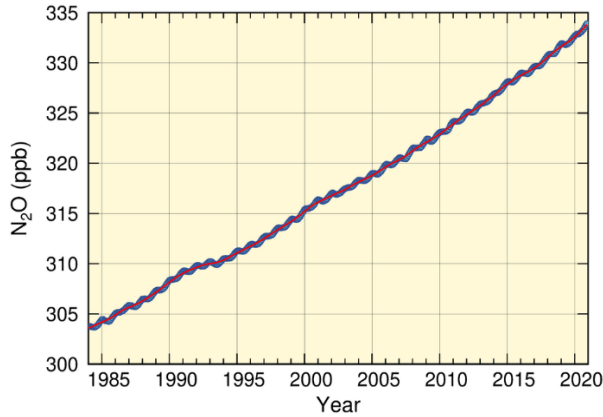


Figure 2.1-12 Global mean concentration of atmospheric N₂O

The blue dots are monthly values, and the red line represents the corresponding sequence after the removal of seasonal variations. Graph content is based on analysis of observation data reported to WDCGG based on the method of WMO (2009). Data contributors are listed in WMO (2022).

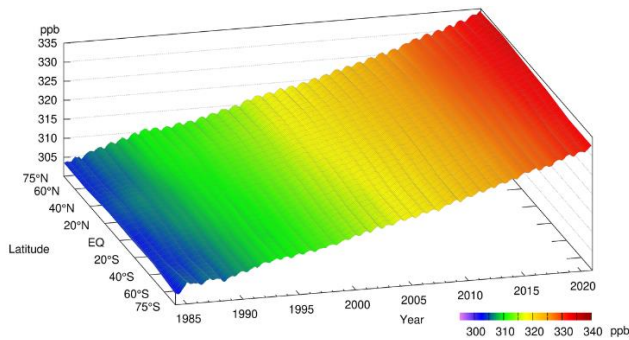


Figure 2.1-13 Latitudinal distribution of atmospheric N₂O concentrations

The data set and analysis method are as per Figure 2.1-12.

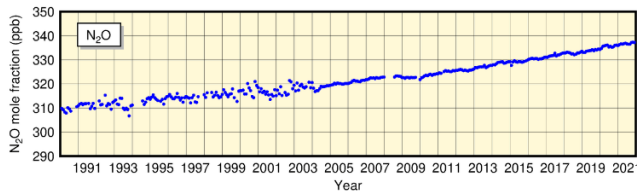


Figure 2.1-14 Monthly mean concentrations of atmospheric N₂O at Ryori

Improvement of observation equipment in 2004 resulted in improved stability of measurements.

2.1.4 Concentration of halocarbons

Halocarbons are generally carbon compounds containing halogens such as chlorine and bromine, many of which are powerful greenhouse gases whose atmospheric concentrations have increased rapidly since the second half of the 20th century due to artificial production. Although their atmospheric concentrations are only around a millionth those of CO₂, their greenhouse effect per unit mass is several thousand times greater.

Chlorofluorocarbons (CFCs: CFC-11, CFC-12 and CFC-113 among others), which are compounds of carbon, fluorine and chlorine, and other halogenated gases are ozone-depleting substances (ODSs). They are regulated under the 1987 Montreal Protocol on Substances that Deplete the Ozone Layer and its Amendments and Adjustments.

Hydrofluorocarbons (a halocarbon variety consisting of carbon compounds containing fluorine and hydrogen, referred to here as HFCs) have no effects on stratospheric ozone depletion and have been used as substitutes for CFCs. However, the Kigali Amendment of 2016 added HFCs to the list of substances subject to regulation under the Montreal Protocol (effective as of 2019) due to their significant greenhouse effects.

(1) Global concentration of halocarbons

Global concentrations of atmospheric CFCs increased rapidly until the 1980s before entering a decreasing trend in the 1990s (Figure 2.1-15). The concentration of CFC-11 peaked in 1992 – 1994, and has since shown a decreasing tendency. The concentration of CFC-12 increased until around 2003, and has also since shown a decreasing tendency. The concentration of CFC-113 reached its maximum in around 1993 in the Northern Hemisphere and around 1996 in the Southern Hemisphere. Differences in the concentrations of these gases between the Northern Hemisphere, where most emissions sources are located, and the Southern Hemisphere, which has significantly fewer sources, have decreased since the 1990s in contrast to the situation of the 1980s. These observations indicate that the CFC emission controls under the Montreal Protocol have been effective.

However, a slowdown in the decline of CFC-11 concentrations has been observed since 2012, with a rate of decrease approximately two thirds of that seen from 2002 to 2012. Results from numerical model calculation suggest that this is attributable to increased global CFC-11 emissions with main sources probably located in eastern Asia (WMO, 2018a; WMO, 2018b; Montzka *et al.*, 2018; Rigby *et al.*, 2019). Since 2018, ground-based observations and numerical model calculation results have suggested a resumed trend of decline in CFC-11 emissions from East Asia (Park *et al.*, 2021), and global ground-based observations have also shown an accelerated decrease in the growth rate of atmospheric CFC-11 concentrations since 2019 (Montzka *et al.*, 2021).

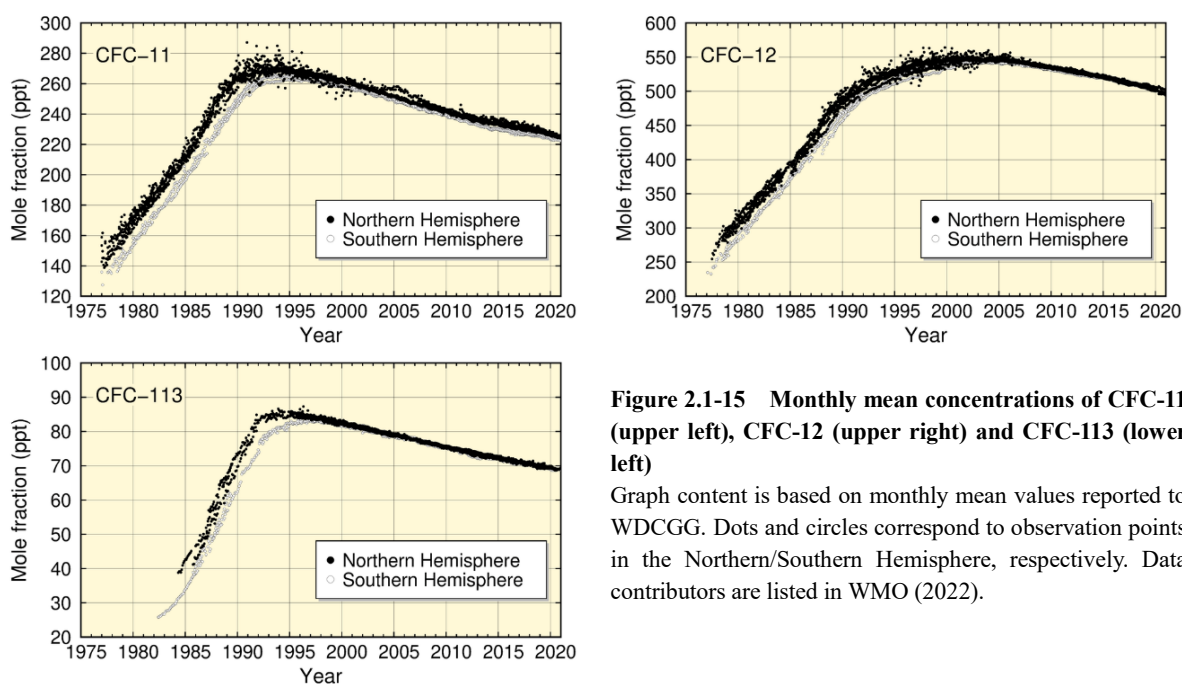


Figure 2.1-15 Monthly mean concentrations of CFC-11 (upper left), CFC-12 (upper right) and CFC-113 (lower left)

Graph content is based on monthly mean values reported to WDCGG. Dots and circles correspond to observation points in the Northern/Southern Hemisphere, respectively. Data contributors are listed in WMO (2022).

As with CFCs, atmospheric concentrations of HFCs are higher in the Northern Hemisphere, where there are more emissions sources than in the Southern Hemisphere (Figure 2.1-16). Atmospheric concentrations of HFC-134a continue to increase, while those of HFC-152a have levelled off in recent years. Atmospheric concentrations of HFC-152a show remarkable seasonal variations.

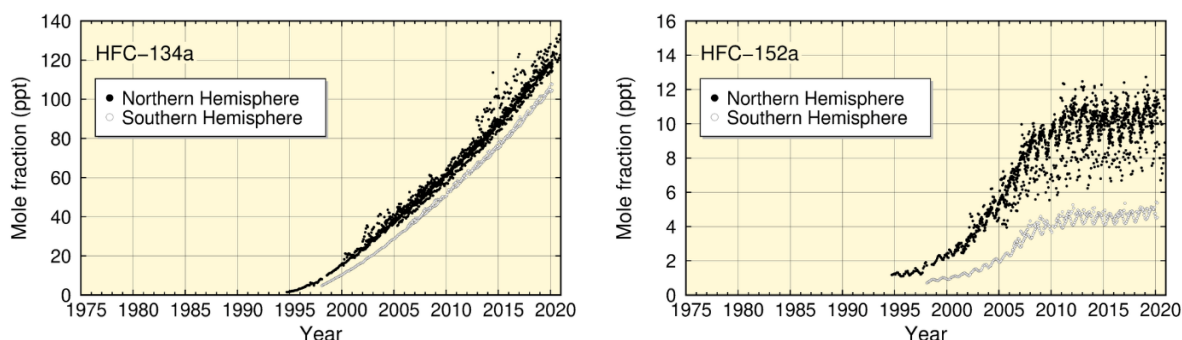


Figure 2.1-16 Monthly mean concentrations of HFC-134a (left) and HFC-152a (right)
The dataset and analysis method are as per Figure 2.1-15.

(2) Concentrations of halocarbons in Japan

Concentrations of CFC-11, CFC-12 and CFC-113 at Ryori have shown decreasing tendencies since reaching maxima in various years (Figure 2.1-17). The concentration of CFC-11 peaked at about 270 ppt in 1993 – 1994, and has since decreased. The distinct peak of concentration observed in 2011 is considered attributable to emissions from polyurethane foam insulation materials released by the Great East Japan Earthquake and the subsequent hugely destructive tsunami of 11 March 2011 (Saito *et al.*, 2015). The rate of increase in CFC-12 concentration slowed around 1995, and a gradual decrease has been seen since 2005. There was no clear tendency of increase or decrease in the concentration of CFC-113 until 2001, but a decreasing tendency has been seen since then.

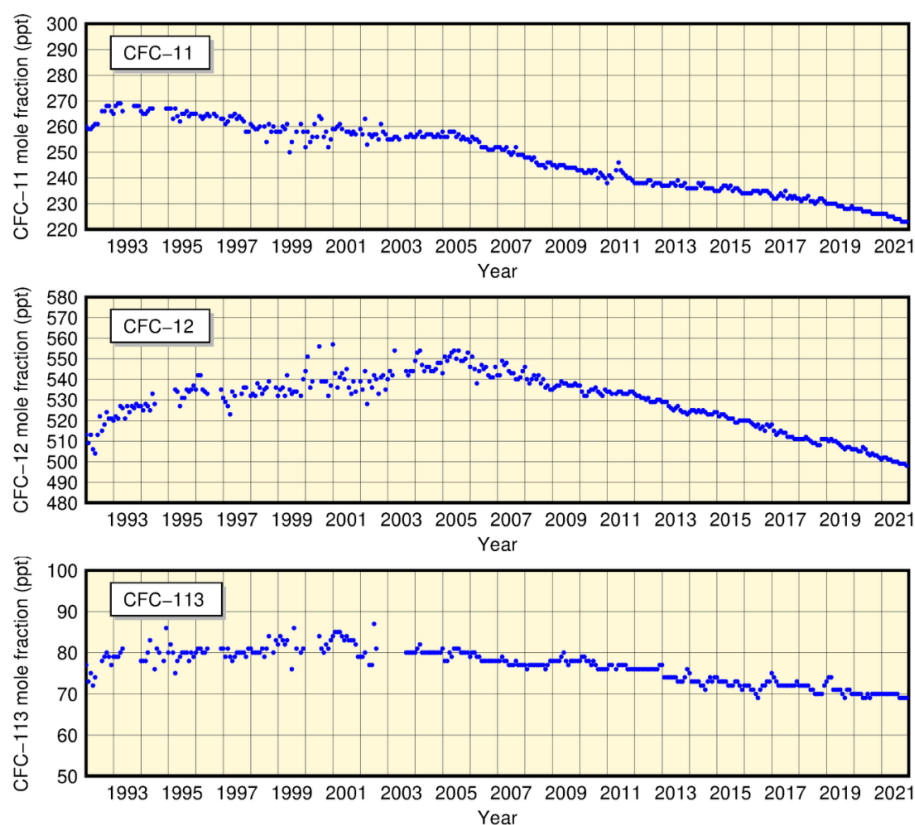


Figure 2.1-17 Monthly mean atmospheric concentrations of CFC-11 (top), CFC-12 (middle) and CFC-113 (bottom) at Ryori

Improvement of observation equipment in September 2003 resulted in improved stability of measurements.

The Japan Meteorological Agency began observing atmospheric HFC concentrations at Minamitorishima in April 2020. The results show that values for HFC-134a and HFC-152a are similar to those at other observation sites in the Northern Hemisphere in the context of global observation (Figure 2.1-18). In particular, atmospheric concentrations of HFC-152a show remarkable seasonal variations with higher concentrations from winter to spring and lower concentrations from summer to fall. Against this background, ongoing long-term monitoring is considered important.

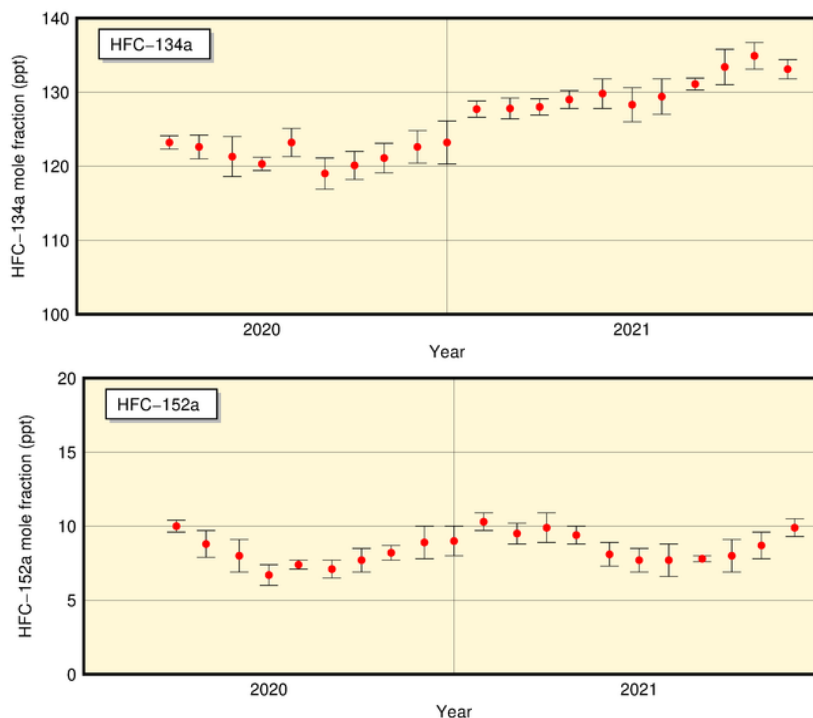


Figure 2.1-18 Monthly mean atmospheric concentrations of HFC-134a (top) and HFC-152a (bottom) at Minamitorishima

Observation of atmospheric HFC concentrations was started in April 2020 at Minamitorishima.

2.2 Aerosols and surface radiation¹⁷

- In Japan, background atmospheric turbidity coefficient values (which depend on concentrations of aerosols, water vapor and other constituents in the air) have returned to approximate levels seen before the eruption of Mt. Agung in 1963. This is mainly because of no large-scale eruptions impacting the global climate since that of Mt. Pinatubo in 1991.
- The number of days when any meteorological station in Japan observed Kosa was 16 in 2021, and the total number of stations reporting its occurrence during the year was 55.

2.2.1 Aerosols

Interannual variations in the atmospheric turbidity coefficient¹⁸, which is calculated from direct solar radiation¹⁹ measurements taken at five stations in Japan excluding the fluctuation component of the troposphere, shows clear impacts of stratospheric aerosols resulting from volcanic eruptions (Figure 2.2-1). The increased turbidity coefficients observed for several years after 1963 and during the periods of 1982 – 1983 and 1991 – 1993 were caused by the eruptions of Mt. Agung (Indonesia) in 1963, Mt. El Chichón (Mexico) in 1982 and Mt. Pinatubo (Philippines) in 1991, respectively. The increased turbidity stems from the persistent presence of sulfate aerosol in the stratosphere resulting from huge amounts of sulfur dioxide (SO₂) released by the volcanic eruptions. The turbidity coefficient has now returned to approximately the same level as that observed before the eruption of Mt. Agung because no large-scale eruptions have occurred since that of Mt. Pinatubo.

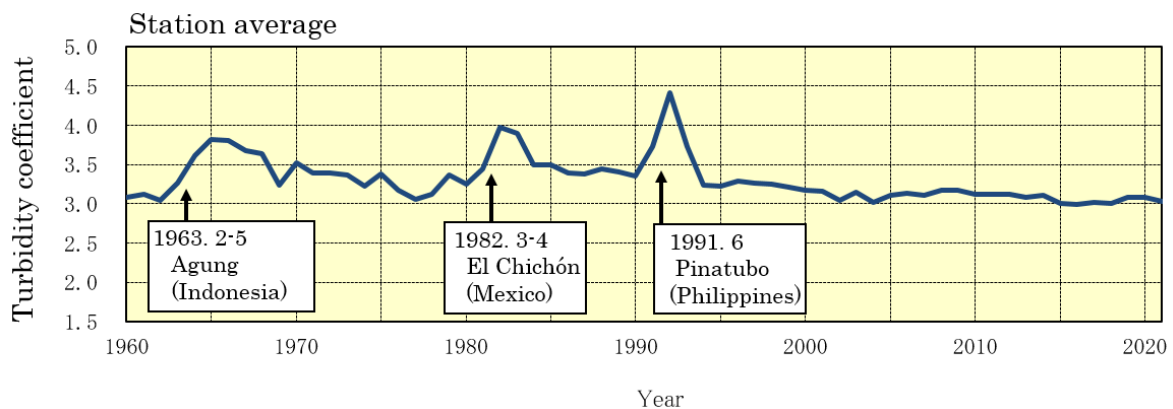


Figure 2.2-1 Time-series representation of annual mean atmospheric turbidity coefficients (1960 – 2021)

To eliminate the influence of variations in tropospheric constituents such as water vapor, dust and air pollutants, the annual mean atmospheric turbidity coefficient is calculated using the minimum turbidity coefficient for each month. Arrows indicate significant volcanic eruptions.

¹⁷ See the Glossary for terms relating to aerosols. Information on surface radiation and Kosa is published on JMA's website. <https://www.data.jma.go.jp/env/kosahp/en/kosa.html> (Aeolian Dust (Kosa))

https://www.data.jma.go.jp/env/radiation/en/info_rad_e.html (Solar and Infrared Radiation)

¹⁸ The atmospheric turbidity coefficient indicates the ratio of the atmospheric optical depth affected by aerosols, water vapor and trace gases in the atmosphere to that uninfluenced by constituents other than air molecules such as oxygen and nitrogen in the atmosphere. Larger values indicate greater amounts of turbid matter in the air.

¹⁹ Direct solar radiation is the incident solar energy acting on the earth's surface from the sun. The atmospheric turbidity coefficient (also known as the Feussner-Dubois turbidity coefficient) can be calculated from direct solar radiation amounts.

2.2.2 Kosa (Aeolian dust)

Kosa (Aeolian dust) is a kind of aerosol blown up from semi-arid areas of the Asian continent and transported by westerly winds to Japan. A total of 11 JMA meteorological stations (as of 31 December 2021) perform Kosa monitoring. The phenomenon is recorded when visually observed by station staff. The number of days when any meteorological station in Japan observed Kosa was 16 in 2021 (Figure 2.2-2), and the total number of stations reporting its occurrence during the year was 55 (Figure 2.2-3).

The number of days on which Kosa was observed shows no discernible trend during the period from 1967 to 2021. The annual total number of stations reporting observation is very likely to have increased (statistically significant at a confidence level of 90%) during the same period, as this trend is reflected in the rich body of observation data available for the 2000 – 2010 period. As the phenomenon shows significant interannual variability, ongoing data collection is necessary to clarify related trends.

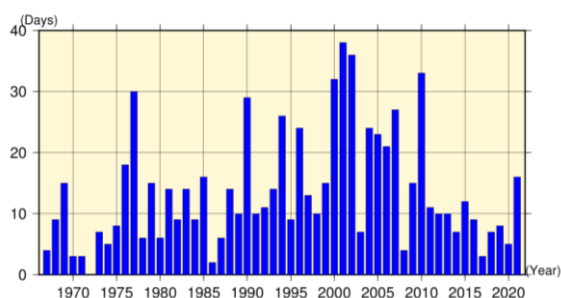


Figure 2.2-2 Number of days when any station in Japan observed Kosa (1967 – 2021) based on the 11 stations that were active for the whole period

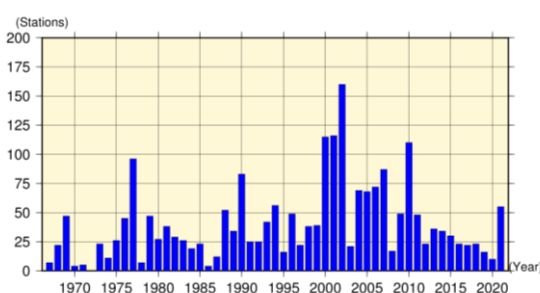


Figure 2.2-3 Annual total number of stations observing Kosa in Japan (1967 – 2021) based on the 11 stations that were active for the whole period

2.2.3 Solar radiation and downward infrared radiation

The earth's radiation budget is a source of energy for climate change, and monitoring of its variations is important. To this end, JMA conducts measurements of direct solar radiation, diffuse solar radiation and downward infrared radiation²⁰ at five stations in Japan (Abashiri, Tsukuba, Fukuoka, Ishigakijima and Minamitorishima) (Figure 2.2-4).

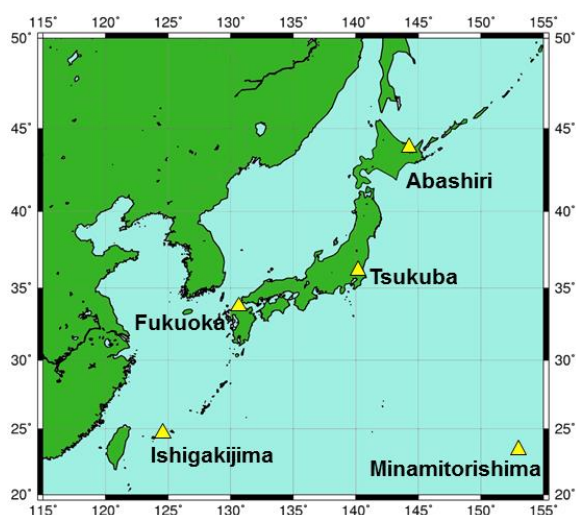


Figure 2.2-4 JMA's solar radiation and infrared radiation observation network

JMA conducts observation of direct solar, diffuse solar and downward infrared radiation at five stations (Abashiri, Tsukuba, Fukuoka, Ishigakijima and Minamitorishima).

²⁰ Downward infrared radiation is the incident infrared radiation acting on the earth's surface from all directions in the sky. It is emitted from clouds and atmospheric constituents such as water vapor and carbon dioxide in proportion to the fourth power of their temperature, and can be used as an index of global warming.

(1) Global solar radiation

Reports indicate that global solar radiation²¹ decreased from around 1960 to the late 1980s before increasing rapidly from the late 1980s to around 2000, and no obvious changes have been observed in most regions of the world (Ohmura, 2009). In Japan, global solar radiation declined from the late 1970s to around 1990 before increasing from around 1990 to the early 2000s. Since then, data from measurements at the five observation stations show no obvious changes. These long-term variations are consistent with those reported globally (Figure 2.2-5).

Variations are considered to stem mainly from changes in anthropogenic aerosols in the atmosphere, and to be partly attributed to changes in cloud cover and cloud characteristics (Wild, 2009). Norris and Wild (2009) quantitatively estimated the cause of the increase in global solar radiation observed in Japan from around 1990 to the beginning of the 2000s. According to their estimates, two thirds of the increase was due to reduced anthropogenic aerosols in the atmosphere and the other third was due to reduced cloud cover. These results imply that the presence of anthropogenic aerosols has a profound effect on solar radiation variations. Results produced by Kudo et al. (2012) indicated that the solar radiation increase was mainly caused by changes in the optical characteristics of aerosols due to changes in the aerosol composition of the atmosphere.

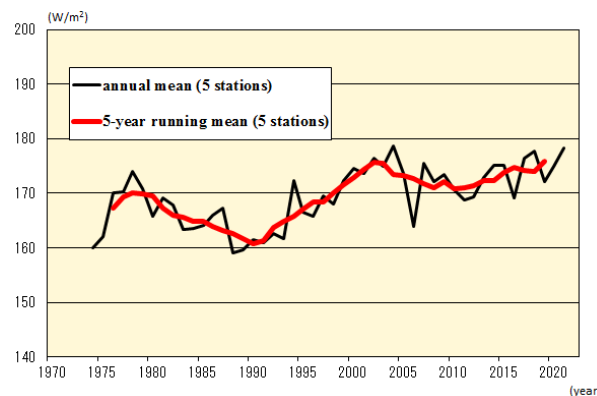


Figure 2.2-5 Time-series representations of annual (black line) and five-year-running (red line) means of global solar radiation at five stations in Japan (Abashiri, Tsukuba, Fukuoka, Ishigakijima and Minamitorishima)

Annual means are based only on monthly mean calculation from more than 20 daily datasets. Before March 2010 (before February 2021 at Abashiri and before December 1987 at Tsukuba), observation was global pyranometer-based, while values have since been derived from the sum of direct and diffused pyranometer observations.

(2) Downward infrared radiation

Atmospheric concentrations of carbon dioxide and other greenhouse gases, which cause global warming, show increasing yearly trends. Observation of downward infrared radiation is effective for the evaluation of global warming because signals of global warming due to increased greenhouse gases are seen more clearly from increased downward infrared radiation than from increased surface temperatures. While general circulation model experiments suggest that two decades of downward infrared radiation monitoring are necessary to detect statistically significant increases with a confidence level of 95%, analysis of in situ observation data covering about a decade has shown an overall increase (Wild and Ohmura, 2004).

In Japan, downward infrared radiation has been monitored since the early 1990s at Tsukuba. Analysis of

²¹ Global solar radiation is the total incident solar energy arriving on a horizontal plane from all directions in the sky, and is the sum of direct solar radiation and diffuse solar radiation (the incident solar energy, except from the direction of the sun, acting on the earth's surface after being scattered by the atmosphere and clouds from all directions in the sky). It is observed either with a pyranometer or as the sum of direct and diffused pyranometer observation results. Data from the latter method are used as much as possible in Figure 2-2.5.

the data obtained shows an increasing trend at a rate of about 0.3 W/m^2 per year during the period from 1993 to 2021 (Figure 2.2-6). This is consistent with the trend seen in the results of analysis using data from 20 BSRN²² stations worldwide ($+0.3 \text{ W/m}^2$ per year during the period from 1992 to 2009) (WCRP, 2010).

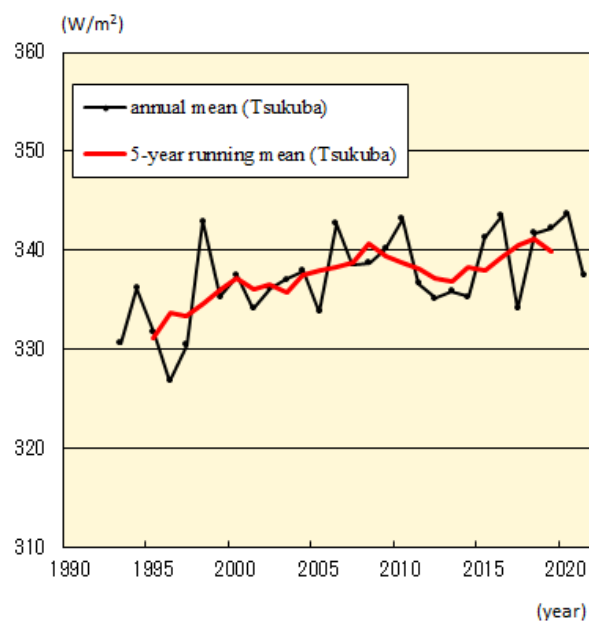


Figure 2.2-6 Time-series representations of annual (black line) and five-year-running (red line) means of downward infrared radiation at Tsukuba

²² The BSRN (Baseline Surface Radiation Network) is a global observation network for measuring high-precision surface radiation balance on an ongoing basis. JMA operates five BSRN stations in Japan (Abashiri, Tsukuba, Fukuoka, Ishigakijima and Minamitorishima) and one in Antarctica (Syowa Station).

2.3 Temperature²³

- The annual anomaly²⁴ of the global average surface temperature in 2021 was +0.22°C, the 6th highest since 1891. On a longer time scale, it is virtually certain that the annual global average surface temperature has risen at rates of 0.73°C per century.
- The annual anomaly of the average temperature over Japan was +0.61°C, the 3rd highest since 1898. On a longer time scale, it is virtually certain that the annual average temperature over Japan has risen at rates of 1.28°C per century.
- It is virtually certain that the annual number of days with maximum temperatures of 35 °C or higher ($T_{\max} \geq 35^{\circ}\text{C}$) and that with minimum temperatures of 25°C or higher ($T_{\min} \geq 25^{\circ}\text{C}$) have increased, while the annual number of days with minimum temperatures below 0°C ($T_{\min} < 0^{\circ}\text{C}$) has decreased.

2.3.1 Global surface temperature

The annual anomaly of the global average surface temperature in 2021 (i.e., the combined average of the near-surface air temperature over land and the SST) was +0.22°C above the 1991 – 2020 average. This was the 6th highest since 1891 (Figure 2.3-1). The years from 2014 to 2021 were the top-eight warmest on record in terms of global temperature. The global average temperature fluctuates on different time scales ranging from years to decades. On a longer time scale, it is virtually certain that the global average surface temperature has risen at a rate of 0.73°C per century²⁵ (statistically significant at a confidence level of 99%²⁶).

The surface temperature anomalies over the Northern Hemisphere and the Southern Hemisphere were +0.35°C (the 5th highest) and +0.09°C (the 9th highest) above the 1991 –2020 average, respectively (Figure 2.3-2). It is virtually certain that average surface temperatures over the Northern Hemisphere and the Southern Hemisphere have risen at rates of 0.77°C and 0.68°C per century, respectively (both statistically significant at a confidence level of 99%).

Linear temperature trends for 5° × 5° latitude/longitude grid boxes indicate that most areas of the world, especially in the high latitudes of the Northern Hemisphere, have experienced long-term warming (Figure 2.3-3). These long-term trends in annual average temperatures can be largely attributed to global warming caused by increased concentrations of greenhouse gases such as CO₂. On a shorter time scale, temperatures fluctuate due to the influence of natural climate dynamics over different time scales ranging from years to decades.

²³ Monthly, seasonal and annual estimates of mean temperatures averaged over the globe and Japan are published on JMA’s website.

<https://www.data.jma.go.jp/cpdinfo/temp/index.html> (Japanese)

<https://www.data.jma.go.jp/tcc/tcc/products/gwp/gwp.html> (English)

²⁴ In this report, the 30-year baseline for anomalies was updated from the 1981 – 2010 average to the 1991 – 2020 average.

²⁵ IPCC AR6 (IPCC, 2021) reported that the global surface temperature from 2001 to 2020 was 0.99°C (with a very likely assessment range of 90 – 100%, or a 90% interval, of 0.84 – 1.10°C) higher than the period from 1850 to 1900. IPCC AR6 values and those in this report show no remarkable difference in rise on a long-term time scale but have been higher since the mid-1990s. Exact correspondence is not observed due to calculation differences and the statistical period examined.

²⁶ For evaluation and clarification of the significance statistics used here, see “Explanatory note on detection of statistical significance in long-term trends” at the end of the report.

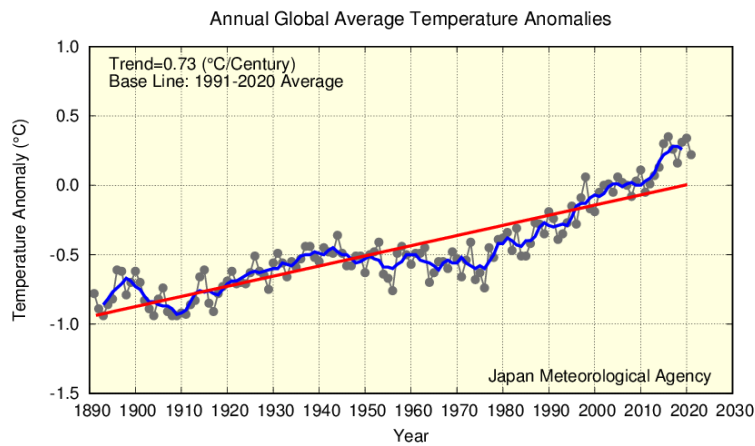


Figure 2.3-1 Annual anomalies in the global surface temperature (i.e., the combined average of the near-surface air temperature over land and the SST) from 1891 to 2021.

Anomalies are deviations from the baseline (i.e., the 1991 – 2020 average). The thin black line with dots indicates surface temperature anomalies for each year. The blue line indicates the five-year running mean, and the red line indicates the long-term linear trend.

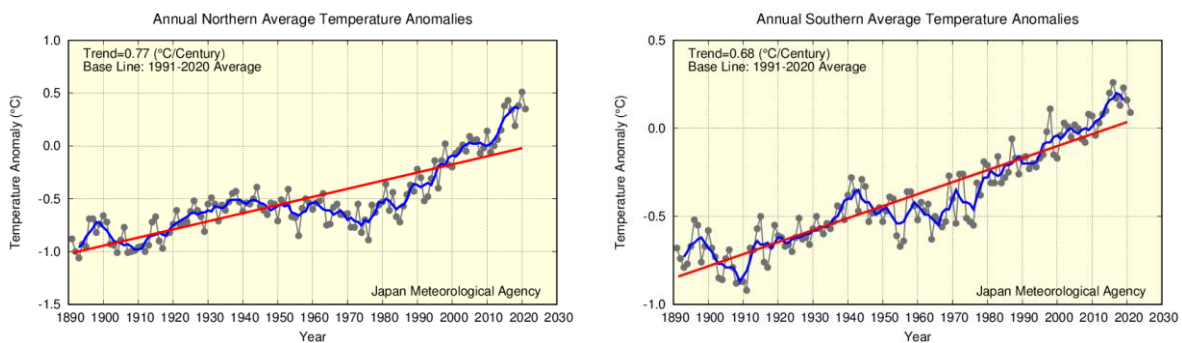


Figure 2.3-2 Annual anomalies in surface temperature (i.e., the combined average of the near-surface air temperature over land and the SST) from 1891 to 2021 for the Northern Hemisphere (left) and for the Southern Hemisphere (right).

Anomalies are deviations from the baseline (i.e., the 1991 – 2020 average). The thin black line with dots indicates surface temperature anomalies for each year. The blue line indicates the five-year running mean, and the red line indicates the long-term linear trend.

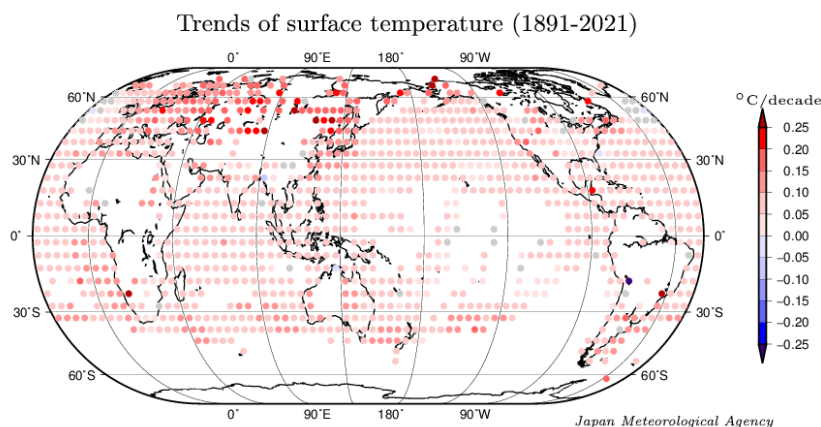


Figure 2.3-3 Linear temperature trends for 5° × 5° latitude/longitude grid boxes for the period of 1891 to 2021

The grid boxes with gray circles have no statistically significant trend (not statistically significant at a confidence level of 90%). Blank areas indicate those with insufficient data to analyze long-term trends.

2.3.2 Surface temperature over Japan

Long-term changes in the surface temperature over Japan are analyzed using observational records dating back to 1898. Table 2.3-1 lists the meteorological stations whose data are used to derive annual mean surface temperatures.

Table 2.3-1 Observation stations whose data are used to calculate surface temperature anomalies over Japan

Miyazaki and Iida were relocated in May 2000 and May 2002, respectively, and their temperatures have been adjusted to eliminate the influence of the relocation.

Element	Observation stations
Temperature (15 stations)	Abashiri, Nemuro, Suttsu, Yamagata, Ishinomaki, Fushiki, Iida, Choshi, Sakai, Hamada, Hikone, Tadotsu, Miyazaki, Naze, Ishigakijima

The mean surface temperature in Japan for 2021 is estimated to have been + 0.61°C above the 1991 – 2020 average, which is the 3rd highest since 1898 (Figure 2.3-4). The surface temperature fluctuates on different time scales ranging from years to decades. On a longer time scale, it is virtually certain that the annual mean surface temperature over Japan has risen at a rate of 1.28°C per century (statistically significant at a confidence level of 99%). Similarly, it is virtually certain that the seasonal mean temperatures for winter, spring, summer and autumn have risen at rates of about 1.20, 1.53, 1.16 and 1.27°C per century, respectively (all statistically significant at a confidence level of 99%).

It is noticeable from Figure 2.3-4 that the annual mean temperature remained relatively low before the 1940s, started to rise and reached a local peak around 1960, entered a cooler era through to the mid-1980s and then began to show a rapid warming trend in the late 1980s. The warmest years on record have all been observed since the 1990s.

The high temperatures seen in recent years have been influenced by fluctuations over different time scales ranging from years to decades, as well as by global warming resulting from increased concentrations of greenhouse gases such as CO₂.

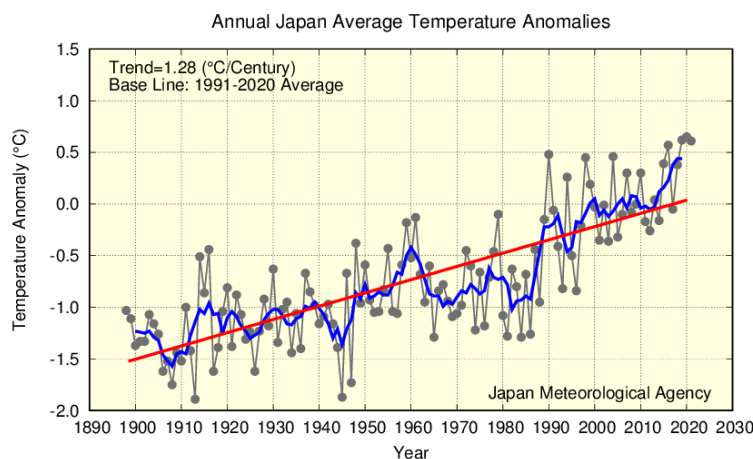


Figure 2.3-4 Annual surface temperature anomalies from 1898 to 2021 in Japan.

Anomalies are deviations from the baseline (i.e., the 1991 – 2020 average). The thin black line indicates the surface temperature anomaly for each year. The blue line indicates the five-year running mean, and the red line indicates the long-term linear trend.

2.3.3 Long-term trends of extreme temperature events in Japan

This section describes long-term trends of extremely high/low-temperature events in Japan, as derived from analysis of temperature records from the 15 observation stations. Though monthly mean temperatures of the stations in Miyazaki and Iida have been adjusted to eliminate the influence of their relocation, records from these two stations are not used for analysis of daily temperatures due to the difficulty of adjustment in regard to the relocation.

(1) Long-term trends of monthly extreme temperatures

It is virtually certain that the frequency of extremely high monthly temperatures has increased during the period from 1901 to 2021, while that of extremely low monthly temperatures has decreased (both statistically significant at the confidence level of 99%) (Figure 2.3-5). The frequency of extremely high monthly temperatures has largely increased since about 1990.

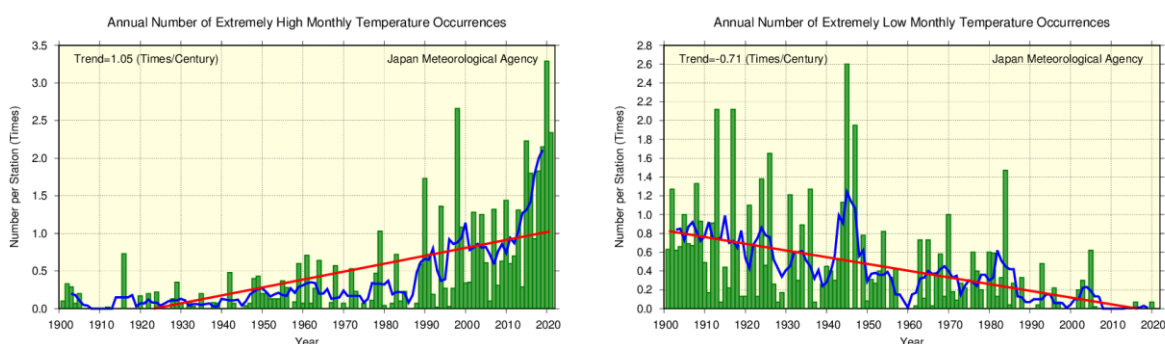


Figure 2.3-5 Annual number of extremely high/low monthly mean temperature occurrences from 1901 to 2021

The graphs show the annual number of occurrences of the highest/lowest first-to-forth values for each month during the period from 1901 to 2021. The green bars indicate the annual occurrences of extremely high/low monthly mean temperatures divided by the total number of monthly observation data sets available for the year (i.e., the average occurrence per station). The blue line indicates the five-year running mean, and the straight red line indicates the long-term linear trend.

(2) Annual number of days with maximum temperatures of $\geq 30^{\circ}\text{C}$ and $\geq 35^{\circ}\text{C}$

The annual number of days with maximum temperatures (T_{\max}) of $\geq 30^{\circ}\text{C}$ and $T_{\max} \geq 35^{\circ}\text{C}$ is virtually certain to have increased during the period from 1910 to 2021 (both statistically significant at a confidence level of 99%) (Figure 2.3-6). Especially, the annual number of days with $T_{\max} \geq 35^{\circ}\text{C}$ has largely increased since about mid-1990s.

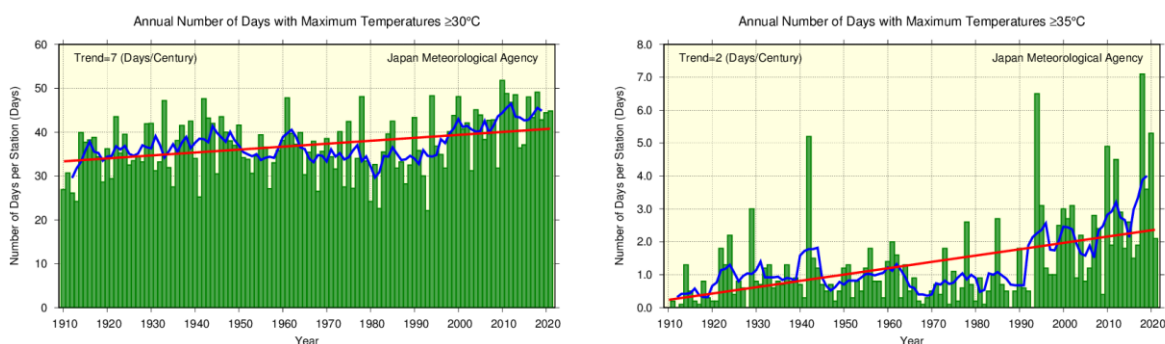


Figure 2.3-6 Annual number of days with maximum temperatures of $\geq 30^{\circ}\text{C}$ and $\geq 35^{\circ}\text{C}$ from 1910 to 2021

The green bars indicate the annual number of days per station for each year. The blue line indicates the five-year running mean, and the straight red line indicates the long-term linear trend.

(3) Annual number of days with minimum temperatures of $< 0^{\circ}\text{C}$ and $\geq 25^{\circ}\text{C}$

It is virtually certain that the annual number of days with minimum temperatures²⁷ (T_{\min}) of $< 0^{\circ}\text{C}$ has decreased, while the annual number of days with $T_{\min} \geq 25^{\circ}\text{C}$ has increased during the period from 1910 to 2021 (both statistically significant at a confidence level of 99%) (Figure 2.3-7).

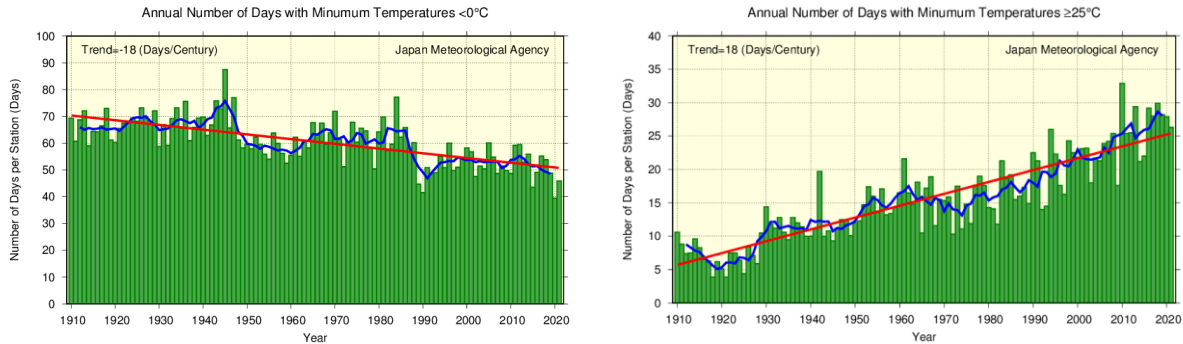


Figure 2.3-7 Annual number of days with minimum temperatures of $< 0^{\circ}\text{C}$ and $\geq 25^{\circ}\text{C}$ from 1910 to 2021
As per Figure 2.3-6.

2.3.4 *Urban heat island effect at urban stations in Japan*

The long-term trends of annual average temperatures are more pronounced for urban observation stations whose data are homogeneous over a long period (Sapporo, Sendai, Tokyo, Yokohama, Niigata, Nagoya, Kyoto, Osaka, Hiroshima, Fukuoka, Kagoshima) than for the average of the 15 rural observation stations (Table 2.3-2 and Figure 2.3-8). Although values varied by location, annual mean temperatures at urban stations (by way of example) were around $0.4 - 1.7^{\circ}\text{C}$ higher than the 15 station averages.

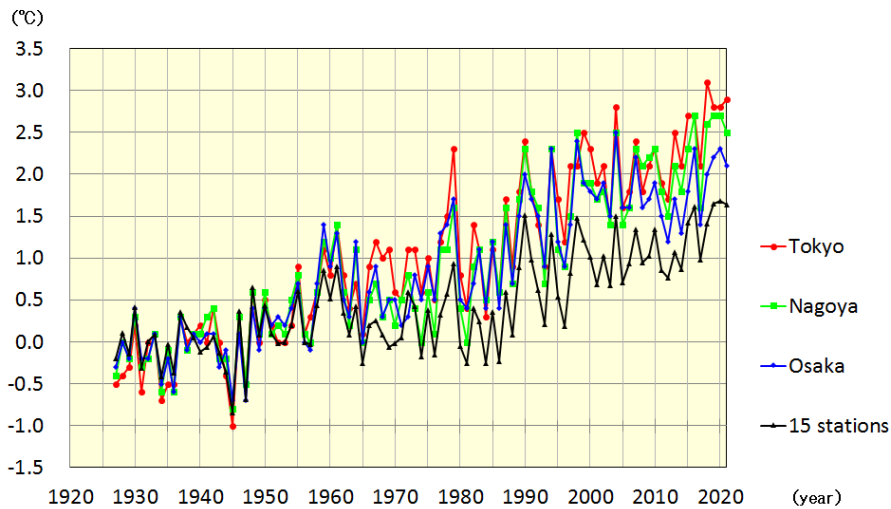


Figure 2.3-8 Annual temperature anomalies at Tokyo, Nagoya and Osaka and values averaged over 15 rural stations in Japan from 1927 to 2021

Anomalies are deviations from the baseline (i.e., the 1927 – 1956 average). Values averaged between 1927 and 1956 for respective stations all equal zero.

²⁷ In JMA statistics, daily maximum and minimum temperatures were observed at the daily boundary of 9:00 for the period 1953 – 1963. Systematic differences caused by a change in the daily boundary time are discussed in Fujibe (1999) and elsewhere. Estimation from monthly differences in daily minimum temperatures between the 9:00 and 24:00 daily boundaries based on observation for the period 2009 – 2020 indicates that the daily minimum temperature can be expected to be about 0.4 to 0.6°C higher than current values depending on the location and month. The number of days with $T_{\min} < 0^{\circ}\text{C}$ is estimated to be about 4.6 higher and that with $T_{\min} \geq 25^{\circ}\text{C}$ about 0.5 lower than the values for each year in the graph (the average number of days for each of 13 locations nationwide) during the period 1953 – 1963.

Table 2.3-2 Long-term trends of annual and seasonal average temperatures at urban stations in Japan

These figures are based on data from 1927 to 2021. The trend of the 15 rural station averages (Table 2.3-1) is also listed. Values shown in italics are not statistically significant at a confidence level of 90%. For stations with asterisks (5 urban stations, and Iida and Miyazaki among the 15 rural stations), trends are calculated after adjustment to eliminate the influence of relocation.

Station	Long-term temperature trend (°C/century)														
	Average					Daily maximum					Daily minimum				
	Ann	Win	Spr	Sum	Aut	Ann	Win	Spr	Sum	Aut	Ann	Win	Spr	Sum	Aut
Sapporo	2.7	3.2	3.0	1.9	2.6	1.1	1.5	1.8	0.7	0.6	4.4	5.5	4.7	3.3	4.2
Sendai	2.5	3.0	3.0	1.5	2.5	1.4	1.7	1.9	1.1	1.1	3.2	3.6	3.8	2.1	3.3
Tokyo*	3.3	4.3	3.4	2.1	3.3	1.9	2.2	2.3	1.4	1.8	4.5	5.9	4.6	3.0	4.4
Yokohama	2.8	3.6	3.1	1.9	2.8	2.6	2.9	3.1	1.9	2.4	3.5	4.6	3.8	2.3	3.5
Niigata*	2.1	2.3	2.6	1.4	1.9	2.0	2.7	2.8	0.9	1.8	2.2	2.4	2.7	1.9	2.0
Nagoya	2.9	3.1	3.2	2.3	3.1	1.5	1.7	1.9	1.1	1.4	3.9	3.9	4.4	3.2	4.3
Kyoto	2.7	2.7	3.1	2.3	2.8	1.2	1.0	1.8	1.1	1.0	3.8	3.8	4.1	3.3	4.0
Osaka*	2.6	2.7	2.7	2.0	2.9	2.2	2.2	2.5	2.0	2.1	3.5	3.2	3.5	3.2	4.0
Hiroshima*	2.0	1.7	2.4	1.5	2.5	1.0	0.8	1.7	1.1	0.6	3.1	2.8	3.4	2.6	3.9
Fukuoka	3.1	3.0	3.4	2.2	3.7	1.8	1.9	2.3	1.4	1.8	4.9	4.4	5.8	3.6	6.0
Kagoshima*	2.5	2.6	2.8	1.9	2.9	1.4	1.3	1.7	1.0	1.4	3.9	3.6	4.4	3.2	4.6
15 station averages*	1.6	1.7	2.0	1.2	1.5	1.2	1.3	1.8	0.9	0.9	1.9	1.9	2.2	1.7	1.9

As it can be assumed that the long-term trends averaged over the 15 rural stations reflect large-scale climate change, the differences in the long-term trends of urban stations from the average of the 15 stations largely represent the influence of urbanization.

Detailed observation reveals that the long-term trends²⁸ are more significant in winter, spring and autumn than in summer and more pronounced for minimum temperatures than for maximum temperatures at every urban observation station.

Records from urban stations whose data are not affected by relocation are used to determine long-term trends for the annual number of days with minimum temperatures of $< 0^{\circ}\text{C}$ and $\geq 25^{\circ}\text{C}$ and maximum temperatures of $\geq 30^{\circ}\text{C}$ and $\geq 35^{\circ}\text{C}$. The number of days with $T_{\min} < 0^{\circ}\text{C}$ is very likely to have decreased with statistical significance at all urban stations, and the number with $T_{\min} \geq 25^{\circ}\text{C}$, $T_{\max} \geq 30^{\circ}\text{C}$ and $T_{\max} \geq 35^{\circ}\text{C}$ is very likely to have increased with statistical significance at most stations except Sapporo (Table 2.3-3).

²⁸ The effect of the change in the daily boundary time for the period 1953 – 1963 (discussed in the previous footnote) is estimated to be negligible in the long-term trend of daily mean minimum temperatures at the 15 sites, as an example.

Table 2.3-3 Long-term trends for the annual number of days with minimum temperatures of $< 0^{\circ}\text{C}$ and $\geq 25^{\circ}\text{C}$ and maximum temperatures of $\geq 30^{\circ}\text{C}$ and $\geq 35^{\circ}\text{C}$.

These figures are based on data from 1927 to 2021. The trend of the 13 rural station averages (Table 2.3-1 excluding Iida and Miyazaki) is also listed. Values shown in italics are not statistically significant at a confidence level of 90%.

Station	Annual number of days			
	Trend (days/decade)			
	$T_{\min} < 0^{\circ}\text{C}$	$T_{\min} \geq 25^{\circ}\text{C}$	$T_{\max} \geq 30^{\circ}\text{C}$	$T_{\max} \geq 35^{\circ}\text{C}$
Sapporo	-4.5	0.0	<i>0.3</i>	<i>0.0</i>
Sendai	-5.9	0.5	1.1	0.1
Yokohama	-5.9	3.1	2.2	0.3
Nagoya	-6.8	3.8	1.3	1.0
Kyoto	-7.1	3.7	1.4	1.4
Fukuoka	-4.8	4.7	1.2	1.1
13 station averages	-2.1	1.8	0.6	0.2

2.4 Precipitation²⁹

- The annual anomaly³⁰ of global precipitation (for land areas only) in 2021 was +29 mm.
- The annual anomaly of precipitation in 2021 was +213.4 mm in Japan. Annual precipitation over Japan shows no discernible long-term trend.
- The annual number of days with daily and hourly extreme precipitation has increased in Japan, while that with wet days has decreased.

2.4.1 Global precipitation over land

Annual precipitation (for land areas only) in 2021 was +29 mm (the 5th heaviest) above the 1991 – 2020 average, and has fluctuated periodically since 1901. In the Northern Hemisphere, records show large amounts of rainfall in the 1950s and after the mid-2000s (Figure 2.4-1). No long-term trends are observed because there are few observation data from the early statistical period and the margin of error is relatively large.

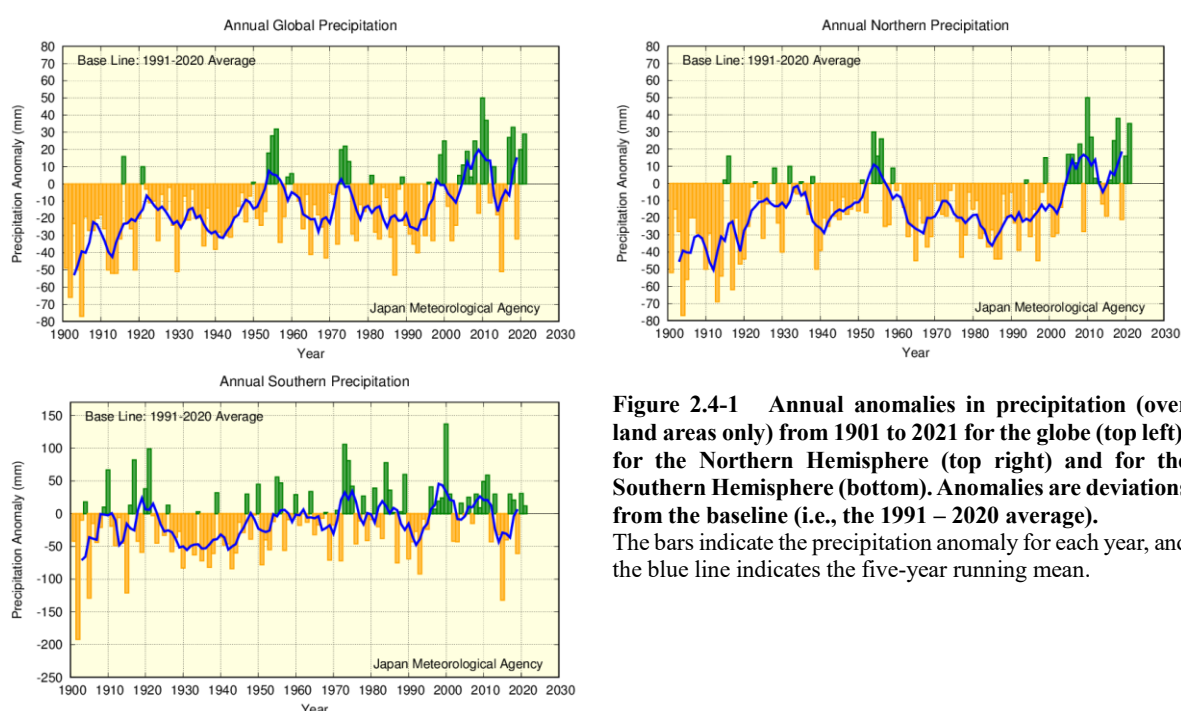


Figure 2.4-1 Annual anomalies in precipitation (over land areas only) from 1901 to 2021 for the globe (top left), for the Northern Hemisphere (top right) and for the Southern Hemisphere (bottom). Anomalies are deviations from the baseline (i.e., the 1991 – 2020 average). The bars indicate the precipitation anomaly for each year, and the blue line indicates the five-year running mean.

2.4.2 Precipitation over Japan

This section describes long-term trends in precipitation over Japan as derived from analysis of precipitation records from 51 observation stations (Table 2.4-1).

Annual precipitation in 2021 was +213.4 mm (the 10th heaviest since 1898) above the 1991 – 2020 average. Japan experienced relatively large amounts of rainfall until the mid-1920s, around the 1950s and after the 2010s. The annual figure exhibits greater variability for the period from the 1970s to the 2000s (Figure 2.4-2).

²⁹ Data on annual precipitation around the world and in Japan are published on JMA's website.

³⁰ In this report, the 30-year baseline for anomalies was updated from the 1981 – 2010 average to the 1991 – 2020 average.

Table 2.4-1 List of 51 observation stations whose data are used to calculate precipitation anomalies and long-term trends in Japan

Element	Observation stations
Precipitation (51 stations)	Asahikawa, Abashiri, Sapporo, Obihiro, Nemuro, Suttsu, Akita, Miyako, Yamagata, Ishinomaki, Fukushima, Fushiki, Nagano, Utsunomiya, Fukui, Takayama, Matsumoto, Maebashi, Kumagaya, Mito, Tsuruga, Gifu, Nagoya, Iida, Kofu, Tsu, Hamamatsu, Tokyo, Yokohama, Sakai, Hamada, Kyoto, Hikone, Shimonoseki, Kure, Kobe, Osaka, Wakayama, Fukuoka, Oita, Nagasaki, Kumamoto, Kagoshima, Miyazaki, Matsuyama, Tadotsu, Kochi, Tokushima, Naze, Ishigakijima, Naha

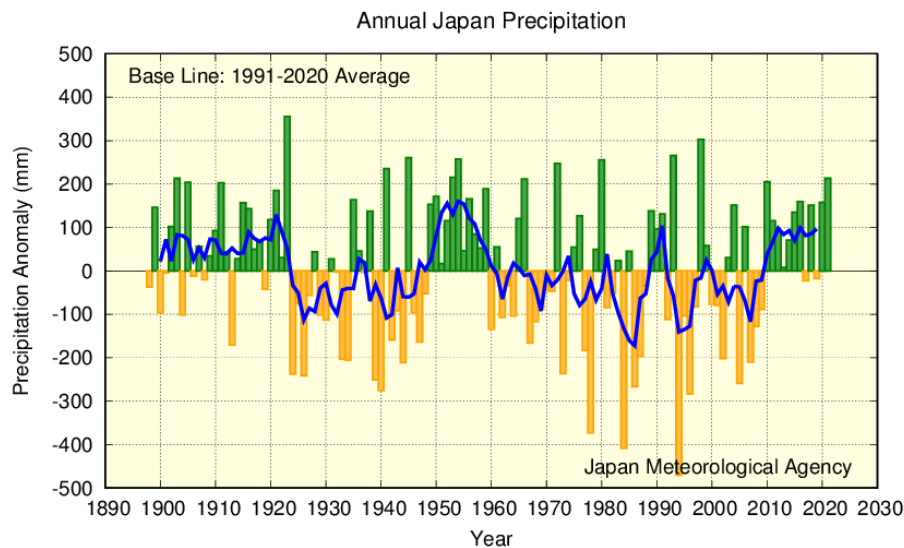


Figure 2.4-2 Annual anomalies in precipitation from 1898 to 2021 in Japan. Anomalies are deviations from the baseline (i.e., the 1991 – 2020 average)

The bars indicate the precipitation anomaly for each year, and the blue line indicates the five-year running mean.

2.4.3 Long-term trends of extreme precipitation events in Japan

(1) Extremely wet/dry months³¹

This part describes long-term trends in frequencies of extremely wet/dry months and heavy daily precipitation events in Japan based on analysis of precipitation data from 51 observation stations.

It is virtually certain that the frequency of extremely dry months increased during the period from 1901 to 2021 (statistically significant at a confidence level of 99%) (Figure 2.4-3 left). There has been no discernible trend in the frequency of extremely wet months (Figure 2.4-3 right).

³¹ Here, judgment of extremely heavy/light precipitation is based on the fourth-highest/lowest monthly values on record over the 121-year period from 1901 to 2021. The frequency of occurrence of the highest/lowest to the fourth-highest/lowest values over this period is once approximately every 30 years, which is close to JMA’s definition of extreme climate events as those occurring once every 30 years or longer (See the Glossary for terms relating to Extreme climate event).

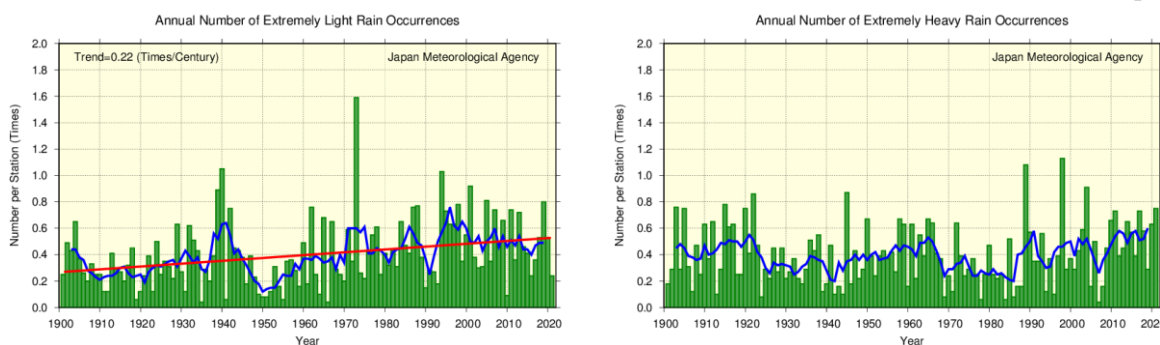


Figure 2.4-3 Annual number of extremely wet/dry months from 1901 to 2021

The graphs show the annual number of occurrences of the first-to-forth heaviest/lightest precipitation values for each month during the period from 1901 to 2021. The green bars indicate annual occurrences of extremely heavy/light monthly precipitation divided by the total number of monthly observation data sets available for the year (i.e., the average occurrence per station). The blue line indicates the five-year running mean, and the straight red line indicates the long-term linear trend.

(2) Annual number of days with precipitation of ≥ 100 mm, ≥ 200 mm and ≥ 1.0 mm

The annual number of days with precipitation of ≥ 100 mm and ≥ 200 mm are virtually certain to have increased during the period from 1901 to 2021 (both statistically significant at a confidence level of 99%) (Figure 2.4-4) . The annual number of days with precipitation of ≥ 1.0 mm (Figure 2.4-5) is virtually certain to have decreased over the same period (statistically significant at a confidence level of 99%). These results suggest decrease in the annual number of wet days including light precipitation and in contrast, an increase in extremely wet days.

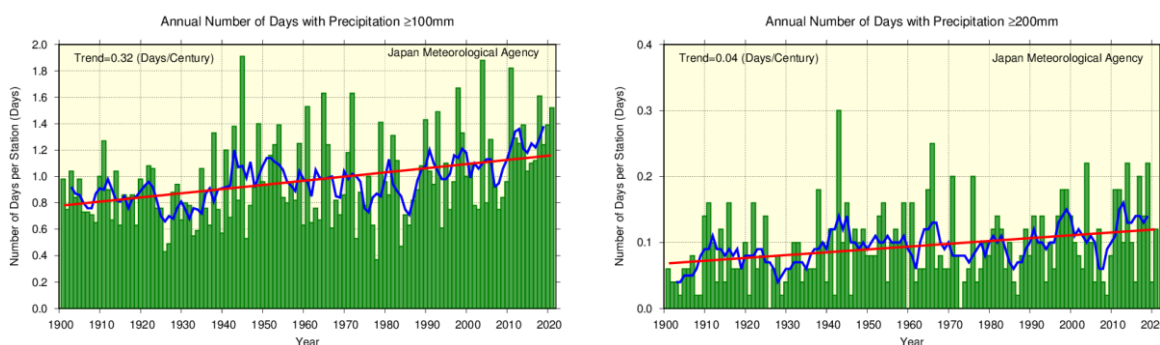


Figure 2.4-4 Annual number of days with precipitation ≥ 100 mm and ≥ 200 mm from 1901 to 2021

The green bars indicate the annual number of days per station for each year. The blue line indicates the five-year running mean, and the straight red line indicates the long-term linear trend.

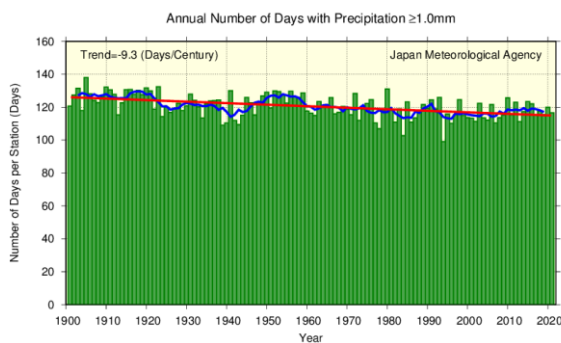


Figure 2.4-5 Annual number of days with precipitation of ≥ 1.0 mm from 1901 to 2021

As per figure 2.4-4 .

(3) Heavy rainfall frequency based on AMeDAS data

JMA operationally observes precipitation at about 1,300 unmanned regional meteorological observation

stations all over Japan (collectively known as the Automated Meteorological Data Acquisition System, or AMeDAS). Observation was started in the latter part of the 1970s at many points, and observation data covering the approximately 45-year period through to 2021 are available³². Although the period covered by AMeDAS observation records is shorter than that of Local Meteorological Observatories or Weather Stations (which have observation records for the past 100 years or so), there are around eight times as many AMeDAS stations as Local Meteorological Observatories and Weather Stations combined. Hence, AMeDAS is better equipped to capture heavy precipitation events that take place on a limited spatial scale.

It is virtually certain that the annual numbers of events with precipitation of ≥ 50 mm and ≥ 80 mm per hour have increased (both statistically significant at a confidence level of 99%) (Figure 2.4-6). For the annual number of days with precipitation of ≥ 50 mm per hour, the number averaged for the last 10 years of the records (2012 – 2021) is about 327 on a per-1,300-station basis, which is about 1.4 times as many as that averaged for the first 10 years (1976 – 1985) of about 226.

The annual number of days with precipitation of ≥ 200 mm and ≥ 400 mm is extremely likely to have increased (both statistically significant at a confidence level of 95%) (Figure 2.4-7).

As the frequency of extreme precipitation events is low and the period covered by observation records is still relatively short, the addition of future observations to the data series is expected to increase the reliability of statistical trend detection.

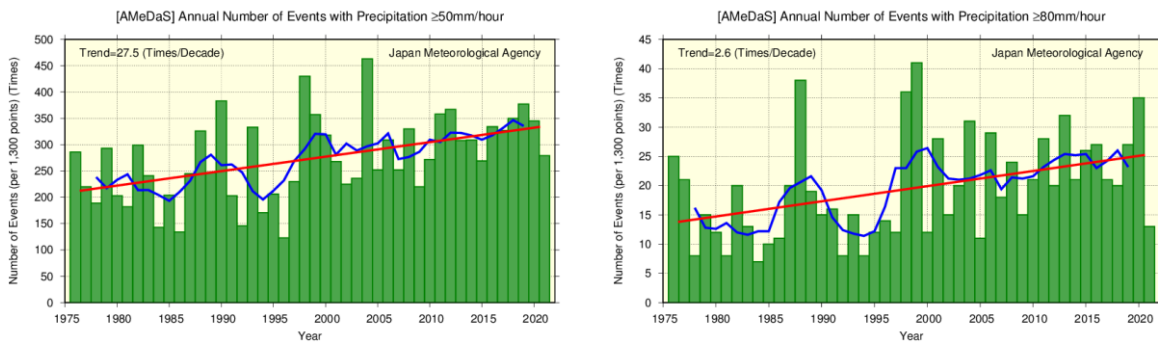


Figure 2.4-6 Annual number of events with precipitation of ≥ 50 mm per hour and ≥ 80 mm per hour from 1976 to 2021
The green bars indicate the annual number of events per 1,300 AMeDAS stations for each year. The blue line indicates the five-year running mean, and the straight red line indicates the long-term liner trend.

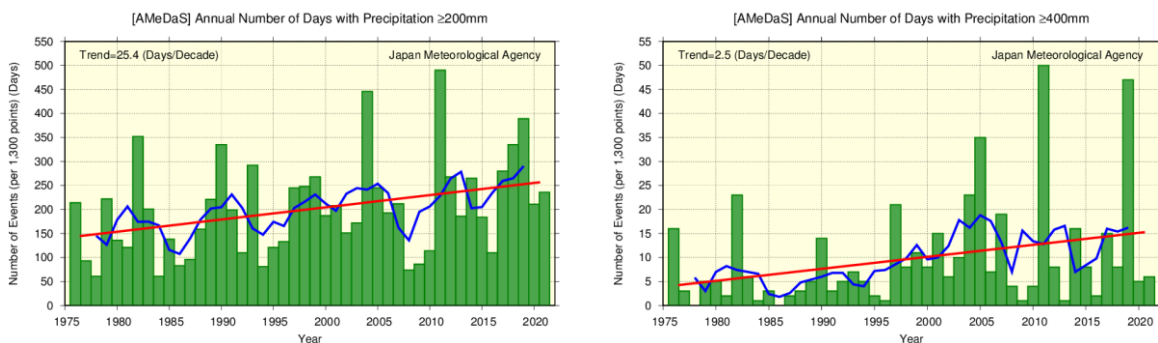


Figure 2.4-7 Annual number of days with precipitation of ≥ 200 mm and ≥ 400 mm from 1976 to 2021
The green bars indicate the annual number of days per 1,300 AMeDAS stations for each year. The blue line indicates the five-year running mean, and the straight red line indicates the long-term liner trend.

³² The number of AMeDAS station was about 800 in 1976, and had gradually increased to about 1,300 now. To account for these numerical differences, the annual number of precipitation events needs to be converted to a per-1,300-station basis. Data from wireless robot precipitation observation stations previously deployed in mountainous areas are also excluded.

(4) Heavy rainfall intensity based on AMeDAS data

Changes in the intensity of annual maximum 24-, 48- and 72-hour precipitation over Japan were analyzed using data from 637 AMeDAS stations where ongoing observation was conducted from 1976 to 2021. Annual data are averages of ratios against the baseline (the 1991 – 2020 average).

It is extremely likely that annual maximum 24-, 48- and 72-hour precipitation increased at rates of 3.3%, 3.8% and 3.7% per decade (each statistically significant at a confidence level of 95%), respectively (Figure 2.4-8).

As for the relation between temperature and water vapor amounts, it is widely accepted that saturated water vapor amounts increase by approximately 7% for each 1°C increment in air temperature. The trend of increased intensity in extreme precipitation events in Japan may be attributable to a long-term increasing trend of the amount of water vapor in the atmosphere associated with a background of long-term temperature rising due to global warming. As per Section (3), the addition of future observations to the data series is expected to increase the reliability of statistical trend determination.

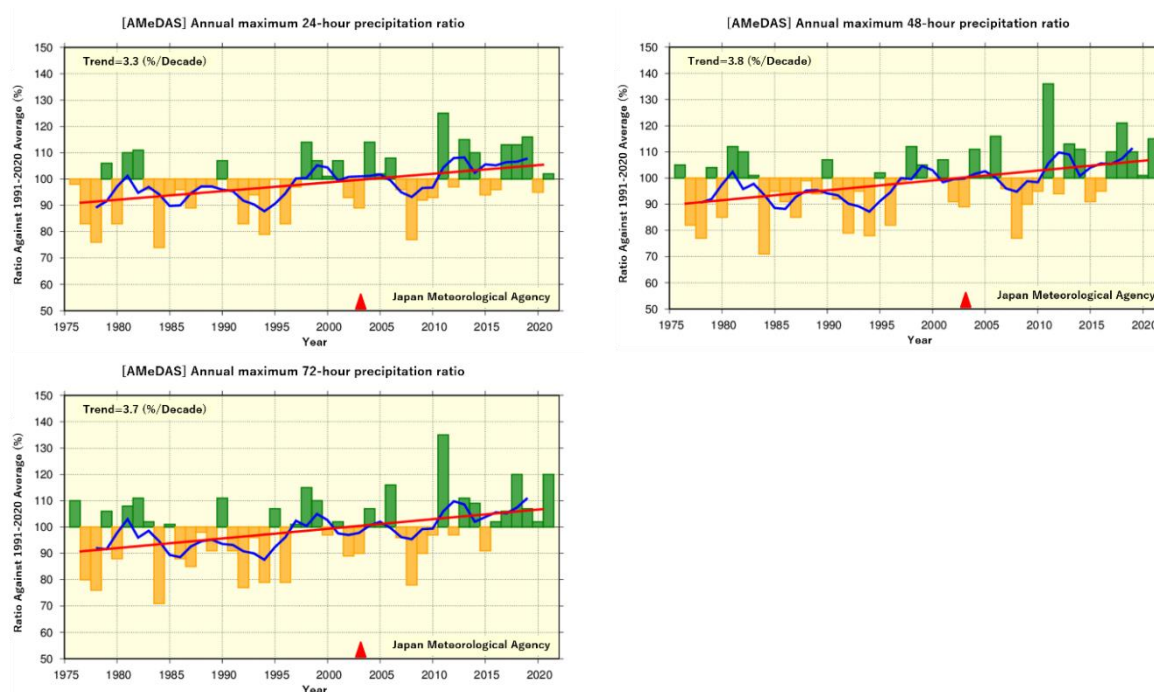


Figure 2.4-8 Annual maximum precipitation ratios (%) for 24-hour (top left) , 48-hour (top right) and 72-hour (bottom) periods over Japan for the period from 1976 to 2021

Annual averages for each year are presented as ratios against the baseline (i.e., the 1991 – 2020 average). The green and yellow bars indicate the annual maximum precipitation ratios for each year based on 637 AMeDAS stations where ongoing observation was conducted from 1976 to 2021. The blue line indicates the five-year running means, and the straight red line indicates the long-term linear trend. Red triangles (▲) indicate the change in observational periodicity for hourly precipitation from every hour to every 10 minutes in 2003³³.

³³ As of 1 Jan. 2003, annual maximum precipitation is determined from 10-minute data as opposed to the previous hourly data. This creates a systematic difference ▲ (e.g., annual maximum daily precipitation ≥ 50 mm tends to average 8 mm more than before.)

2.5 Snow depth and snow cover

- Snow depth on the Sea of Japan side is extremely likely to have decreased.
- It is extremely likely that a decreasing trend is observed in the interannual variability of the total snow cover extent in the Northern Hemisphere for January, June and the period from September to December and in Eurasia for the period from January to March, June and the period from September to December.
- In winter 2020/2021, there were more days of snow cover than normal over northern China and the eastern USA, and fewer over eastern Europe and western China.

2.5.1 Snow depth in Japan

Long-term trends in the annual maximum snow depth (represented in terms of a ratio against the 1991 – 2020 average) in Japan since 1962³⁴ are analyzed using observational records from stations located on the Sea of Japan coast (Table 2.5-1).

Table 2.5-1 Observation stations whose data are used to calculate snow depth ratios in Japan

Region	Observation stations
Sea of Japan side of northern Japan	Wakkanai, Rumoi, Asahikawa, Sapporo, Iwamizawa, Suttu, Esashi, Kutchan, Wakamatsu, Aomori, Akita, Yamagata
Sea of Japan side of eastern Japan	Wajima, Aikawa, Niigata, Toyama, Takada, Fukui, Tsuruga
Sea of Japan side of western Japan	Saigo, Matsue, Yonago, Tottori, Toyooka, Hikone, Shimonoseki, Fukuoka, Oita, Nagasaki, Kumamoto

The annual maximum snow depth ratio in 2021 was 120% relative to the 1991 – 2020 average for the Sea of Japan side of northern Japan, 200% for the same side of eastern Japan, and 152% for the same side of western Japan (Figure 2.5-1). On a longer time scale, the annual maximum snow depth ratio from 1962 on each area is extremely likely to have decreased (statistically significant at a confidence level of 95%). The annual maximum snow depth reached a local peak in the early 1980s followed by a sharp decline until around the early 1990s. The decline was particularly striking on the Sea of Japan side of eastern and western Japan.

As annual maximum snow depth fluctuates greatly and the period covered by observation records is still relatively short, addition of future observations to the data series is expected to increase the reliability of statistical trend determination.

³⁴ Annual statistical data here are focused on winter (e.g., the value for 1976 is from data for August 1975 – July 1976).

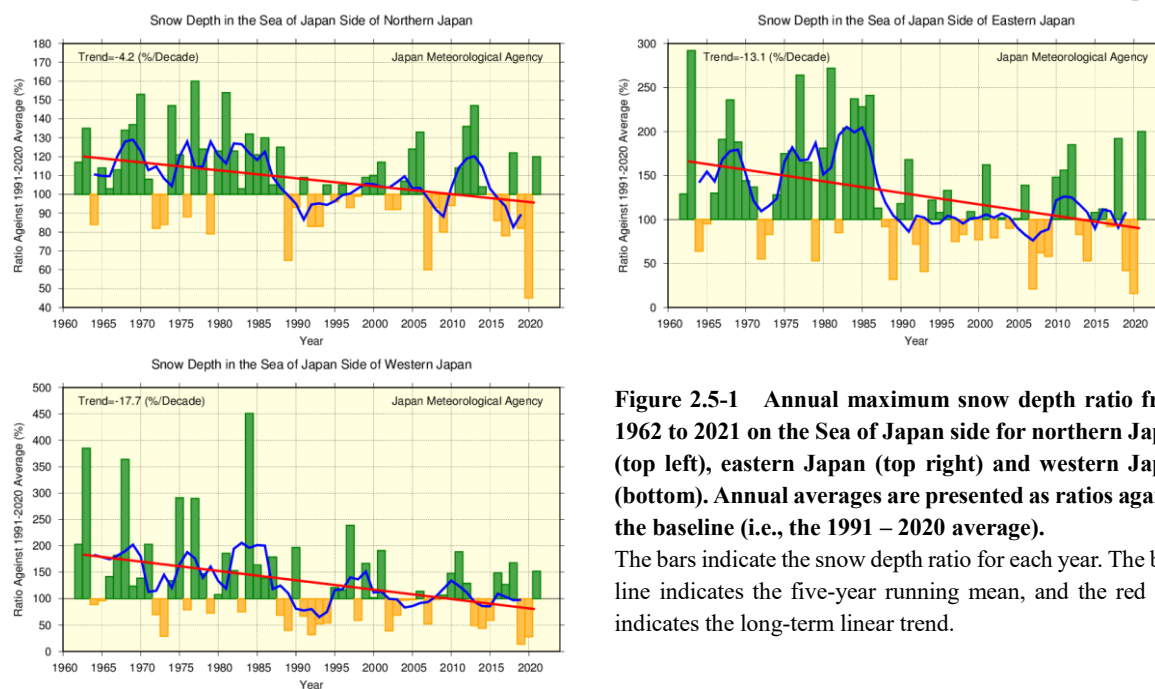


Figure 2.5-1 Annual maximum snow depth ratio from 1962 to 2021 on the Sea of Japan side for northern Japan (top left), eastern Japan (top right) and western Japan (bottom). Annual averages are presented as ratios against the baseline (i.e., the 1991 – 2020 average).

The bars indicate the snow depth ratio for each year. The blue line indicates the five-year running mean, and the red line indicates the long-term linear trend.

2.5.2 Snow cover in the Northern Hemisphere

JMA monitors snow-cover variations in the Northern Hemisphere using analysis data from satellite observations³⁵ based on its own algorithm. The average seasonal migration of snow cover in the Northern Hemisphere normally peaks around January - February and decreases in spring.

In the Northern Hemisphere (north of 30°N), it is extremely likely (statistically significant at a confidence level of 95%) that a decreasing trend is observed in the interannual variability of the total snow cover extent over the 34-year period from 1988 to 2021 for January, June and the period from September to December, while no discernible trend is seen for the period from February to May (Figure 2.5-2 (a) and (c)). In Eurasia (north of 30°N from 0° to 180°E), it is extremely likely (statistically significant at a confidence level of 95%) that a decreasing trend is observed in the interannual variability of the total snow cover for the period from January to March, June and the period from September to December, while no discernible trend is seen for the period from April to May and the period from July to August (Figure 2.5-2 (b) and (d)). In winter (December to February) 2020/2021, there were more days of snow cover than normal over northern China and the eastern USA, and fewer over eastern Europe and western China (Figure 2.5-2 (e)). In November 2021, there were fewer days of snow cover than normal over North America (Figure 2.5-2 (f)).

The albedo of snow-covered ground (i.e., the ratio of solar radiation reflected by the surface) is higher than that of snow-free ground. The variability of snow cover has an impact on the earth's surface energy budget and radiation balance, and therefore on the climate. In addition, snow absorbs heat from its surroundings and melts, thereby providing soil moisture and related effects on the climate system. The variability of atmospheric circulation and oceanographic conditions affects the amount of snow cover, which exhibits a close and mutual association with climatic conditions. Snow-cover variations in Eurasia and other parts of the Northern Hemisphere may affect climate conditions in Japan, but the mechanisms behind such a potential influence remain unclear. The accumulation of future observation data in addition to the current body of information and the implementation of related research are expected to increase the reliability of statistical work to identify

³⁵ The Defense Meteorological Satellite Program (DMSP) polar-orbiting satellites of the USA, equipped with the Special Sensor Microwave/Imager (SSM/I) and the Special Sensor Microwave Imager Sounder (SSMIS), and the Japan Aerospace Exploration Agency (JAXA) Global Change Observation Mission – Water (GCOM-W) satellite, equipped with the Advanced Microwave Scanning Radiometer 2 (AMSR2)

trends of snow cover extent and help to elucidate how snow-cover variations affect climate conditions.

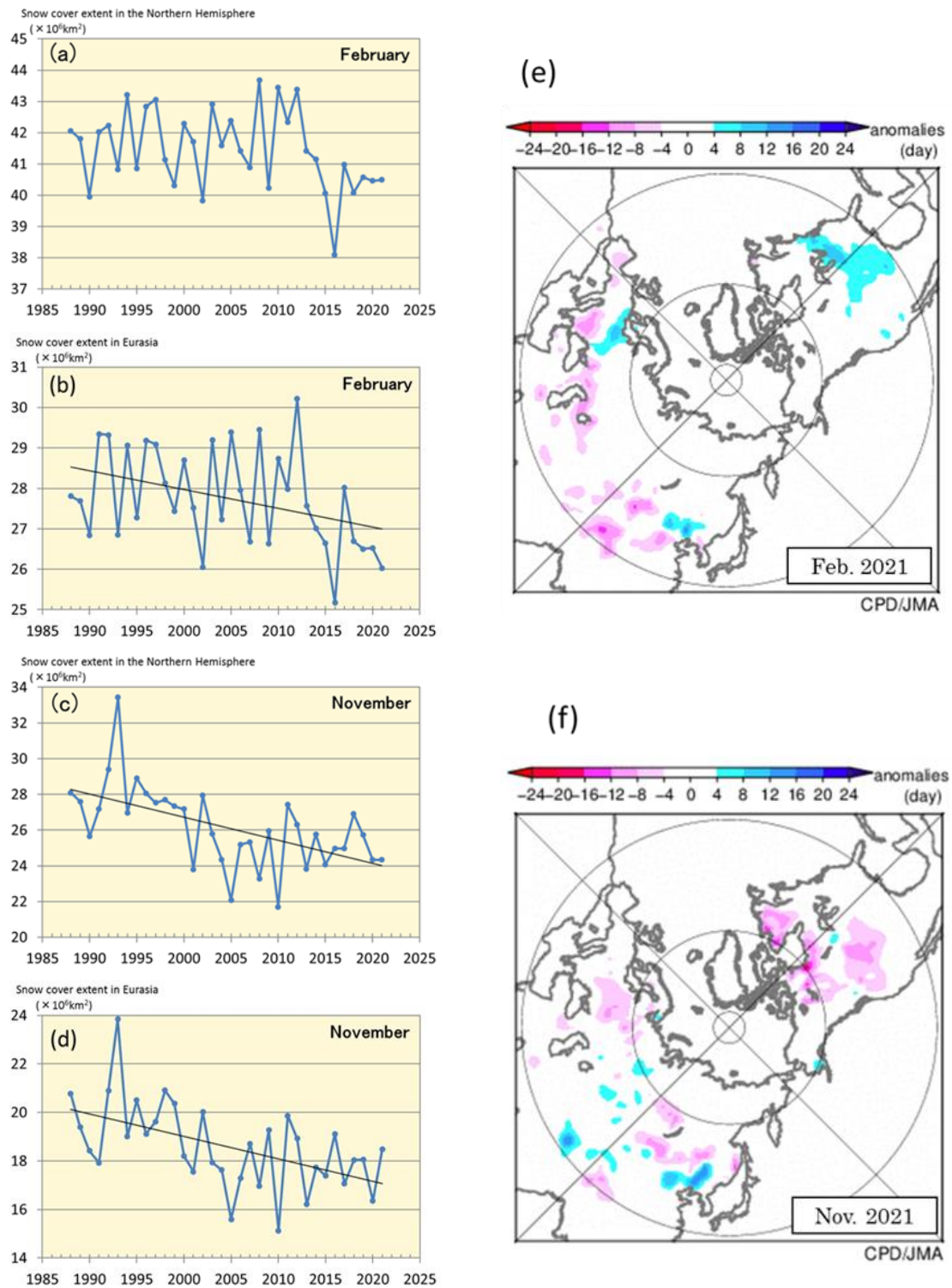


Figure 2.5-2 Interannual variations in the total area of monthly snow cover (km^2) in the Northern Hemisphere (north of 30°N) for (a) February and (c) November and in Eurasia (north of 30°N , from 0° to 180°E) for (b) February and (d) November from 1988 to 2021, and anomalies in the number of days with snow cover for (e) February and (f) November in 2021

(a) - (d): The blue lines indicate the total snow cover area for each year, and the black lines show linear trends (statistically significant at a confidence level of 95%).

(e) - (f): Blue (red) shading indicates more (fewer) days of snow cover.

The base period for the normal is 1991 – 2020.

2.6 Tropical cyclones over the western North Pacific and the South China Sea

Sea

- A total of 22 tropical cyclones (TCs) with maximum wind speeds of 34 kt³⁶ or higher formed over the western North Pacific and the South China Sea in 2021, which was below normal.
- The numbers of formations show no significant long-term trend.

In 2021, 22 tropical cyclones (TCs) with maximum wind speeds of ≥ 34 kt formed over the western North Pacific and the South China Sea (Figure 2.6-1), which was below normal (i.e., the 1991 – 2020 average) of 25.1. The numbers of formations show no discernible long-term trend during the analysis period from 1951 to 2021, while they have often been below normal from the latter half of the 1990s to the early 2010s. Numbers of TCs with maximum wind speeds of ≥ 34 kt approaching and making landfall in Japan were 12 and 3 (Figure 2.6-1), both of which were near normal of 11.7 and 3.0, respectively. The numbers of TCs approaching Japan also show no discernible long-term trend during the same period from 1951 to 2021.

IPCC AR6 WG1 (August 2021) reported that the number of Category 4 – 5³⁷ TCs with wind speeds exceeding 58 m/s in the western North Pacific had increased since the 1980s, and that the latitude of peak intensity had shifted northward (medium confidence). As long-term trends of strong TCs in the Northwest Pacific were not evaluated with a high degree of confidence in the latest IPCC report, ongoing higher-quality observation and monitoring of long-term trends in results are needed.

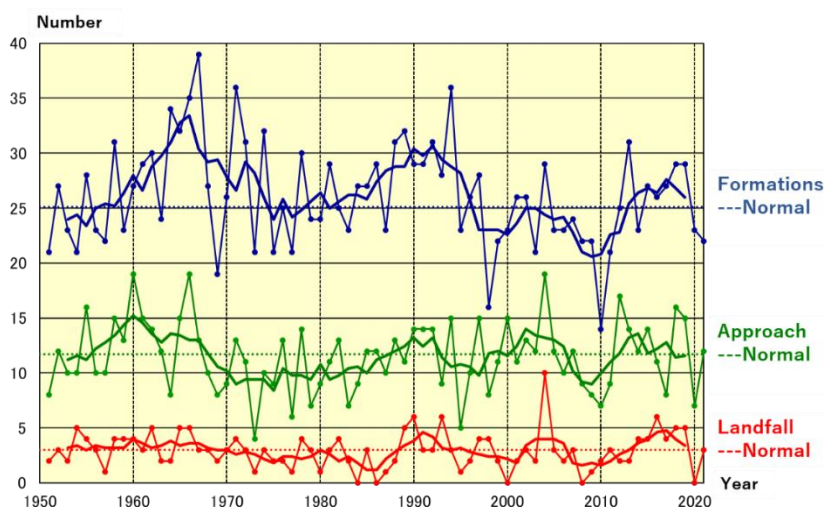


Figure 2.6-1 Time-series of the numbers of TCs with maximum wind speeds of ≥ 34 kt forming in the western North Pacific and the South China Sea (blue), approaching (green) and making landfall in Japan (red) from 1951 to 2021. The thin and thick lines represent annual and five-year running means, respectively.

³⁶ One knot (kt) is about 0.51 m/s

³⁷ "Category 4-5" mentioned here is classifications for hurricane intensity. JMA's evaluation of tropical cyclone intensity is based on 10-minute average wind speeds, while that for hurricanes is based on 1-minute values.

2.7 Phenology of cherry blossoms and acer leaves in Japan

- It is virtually certain that cherry blossoms have been flowering earlier.
- It is virtually certain that acer leaves have been changing color later.

JMA implements phenological observation to monitor seasonal progress, geographical variations and long-term changes in relation to the climate. Observation covers the first/full flowering and foliage color changes in several types of flora.

As part of its phenological monitoring, JMA observes cherry blossoms at 58 stations and acer leaves at 51 stations. Figure 2.7-1 shows interannual changes in the first reported dates of cherry blossom flowering and acer leaf color change between 1953 and 2021. The former exhibits a long-term advancing trend at a rate of 1.1 days per decade, while the latter shows a delaying trend at a rate of 3.1 days per decade (99% level of confidence for both cases). Table 2.7-1 compares climatological normals (based on 30-year averages) of the first reported date of cherry blossom flowering between 1961 – 1990 and 1991 – 2020 at stations in major Japanese cities. These phenomena are closely related to the surface mean temperature in the period before the event, and long-term warming is considered to be a major factor behind the trends observed.

IPCC AR6 WG1 reports several long-term trends in plant phenology. By way of example, peak blooming of cherry blossoms in Kyoto has been increasingly earlier in recent decades based on historical records covering several hundred years (Aono and Saito, 2010)

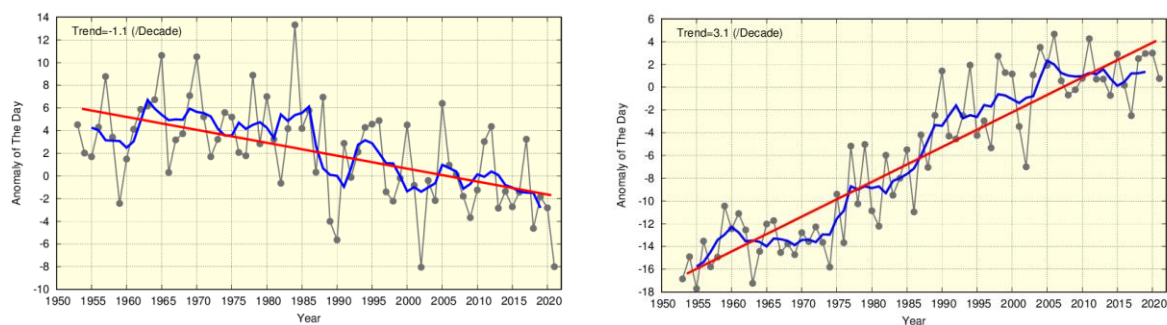


Figure 2.7-1 First reported dates of cherry blossom flowering (left) and acer leaf color change (right)

The black lines show annual anomalies of the first reported date averaged over all observation stations nationwide based on the normals for 1991 – 2020, and the blue lines indicate five-year running means. The red lines show the linear trend (cherry blossoms: -1.1 days per decade; acer leaves: $+3.1$ days per decade).

Table 2.7-1 Comparison of first reported dates of cherry blossom flowering

Differences in climatological normals for the first reported date of cherry blossom flowering between 1991 – 2020 and 1961 – 1990 at stations in major Japanese cities

	1961-1990 average	1991-2020 average	Difference (days)		1961-1990 average	1991-2020 average	Difference (days)
Kushiro	May 19	May 16	-3	Osaka	Apr 1	Mar 27	-5
Sapporo	May 5	May 1	-4	Hiroshima	Mar 31	Mar 25	-6
Aomori	Apr 27	Apr 22	-5	Takamatsu	Mar 31	Mar 27	-4
Sendai	Apr 14	Apr 8	-6	Fukuoka	Mar 28	Mar 22	-6
Niigata	Apr 13	Apr 8	-5	Kagoshima	Mar 27	Mar 26	-1
Tokyo	Mar 29	Mar 24	-5	Naha	Jan 16	Jan 16	0
Nagoya	Mar 30	Mar 24	-6	Ishigakijima	Jan 15	Jan 18	+3

2.8 Sea surface temperature³⁸

- The annual mean global average sea surface temperature (SST) in 2021 was 0.13° C above the 1991 - 2020 average, and was the sixth highest since 1891.
- The global average SST has risen at a rate of about +0.56°C per century.
- Globally integrated ocean heat content (OHC) exhibits a long-term increase.
- OHC has exhibited a higher rate of increase since the mid-1990s.
- Annual average SSTs around Japan have risen by +1.19°C per century.

2.8.1 Global sea surface temperature

The annual mean global average SST in 2021 was 0.13°C above the 1991 – 2020 average. This was the sixth highest since 1891. The years from 2014 to 2021 represent the top-eight warmest since 1891.

The linear trend from 1891 to 2021 shows an increase of +0.56°C per century (Figure 2.8-1). Although magnitudes of the long-term SST trend vary by area, it is extremely likely that SSTs have increased in many parts of the world's oceans (Figure 2.8-2). Global average SSTs and global average surface temperatures (Section 2.3) are affected by natural climate variability on inter-annual to inter-decadal time scales as well as by global warming.

On a multi-year time scale, global average SSTs showed a rising trend from the middle of the 1970s to around 2000, before remaining largely static until the early 2010s and thereafter re-assuming an upward trend (Figure 2.8-1, blue line). This is partly because rising trends overlap with decadal-to-multi-decadal variations in the climate system. It is important to estimate the contribution of these internally induced natural variations in order to properly understand global warming. In the next section, the Pacific Decadal Oscillation (PDO) is presented as a typical example of decadal variability observed in SSTs.

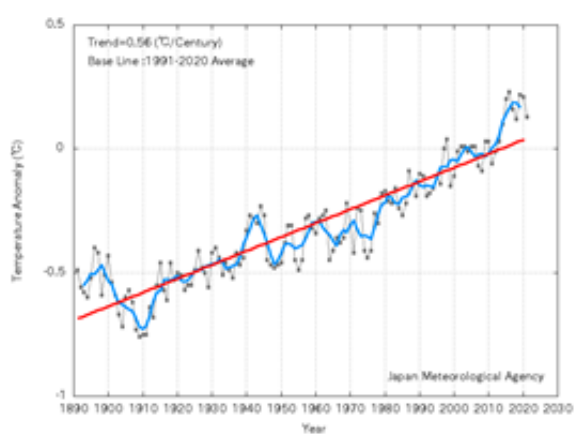


Figure 2.8-1 Time-series representation of global average sea surface temperature anomalies from 1891 to 2021

The black, blue and red lines indicate annual anomalies, the five-year running mean and the long-term linear trend, respectively. Anomalies are deviations from the 1991 – 2020 average.

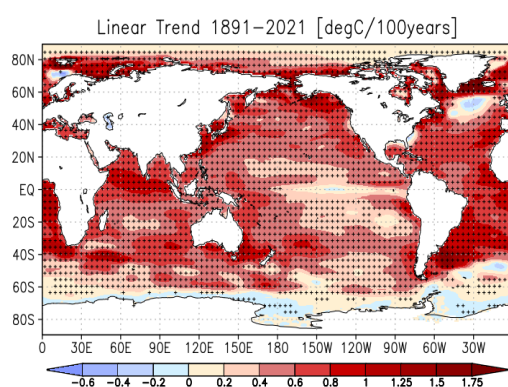


Figure 2.8-2 Linear trend of annual mean sea surface temperature during the period from 1891 to 2021 (°C per century)

Plus signs indicate statistically significant trends with a confidence level of 95%.

³⁸ The results of analysis regarding tendencies of SSTs worldwide and around Japan are published on JMA's website.

https://www.data.jma.go.jp/kaiyou/english/long_term_sst_global/glb_warm_e.html

https://www.data.jma.go.jp/kaiyou/english/long_term_sst_japan/sea_surface_temperature_around_japan.html

2.8.2 Global ocean heat content

Oceans have a significant impact on the global climate because they cover about 70% of the earth’s surface and have high heat capacity. IPCC AR6 WG1 (IPCC, 2021) said that approximately 90% of heat energy in the earth’s system was present in oceans since 1970.

It is virtually certain that globally integrated ocean heat content (OHC) from 0 to 2,000 m exhibits a long-term increase (statistically significant at a confidence level of 99%) (Figure 2.7-3). OHC had risen by approximately $45 \times 10^{22}\text{J}$ in 2021 relative to 1955. Since the mid-1990s, the rate of increase ($9.9 \times 10^{22}\text{J}$ per decade for 1993 –2021) has risen ($3.9 \times 10^{22}\text{J}$ per decade for 1955 – 1993). The Intergovernmental Panel on Climate Change Special Report on the Ocean and Cryosphere in a Changing Climate (IPCC, 2019) and IPCC (2021) also reported an accelerated increase of ocean heat uptake.

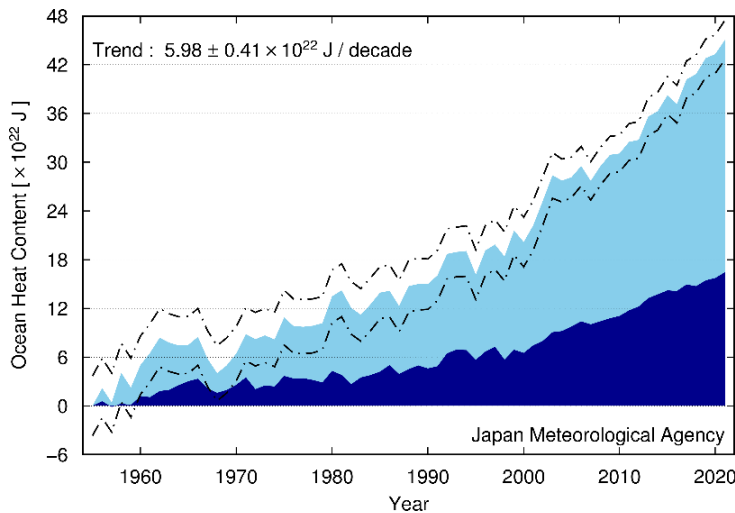


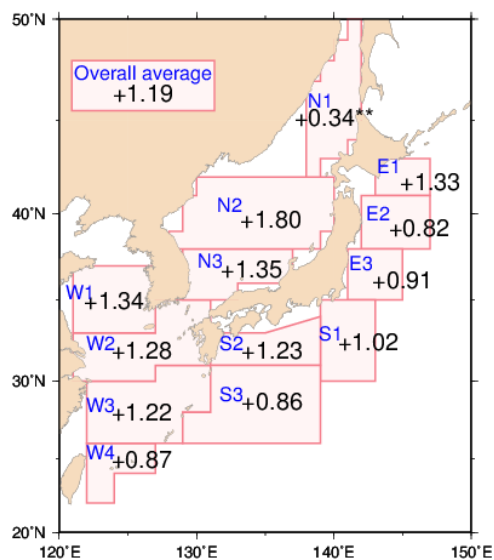
Figure 2.8-3 Time-series representation of globally integrated ocean heat content relative to 1955

The light- and dark-blue areas show annual means for global integrals of 0 to 700 m and 700 to 2,000 m, respectively, for ocean heat content relative to 1955. The dot-dash lines indicate a 95% confidence level for ocean heat content above 2,000 m.

2.8.3 Sea surface temperature (around Japan)

Figure 2.8-4 shows increase rates of area-averaged annual mean SSTs for 13 areas around Japan. The average SST of all areas around Japan has risen by $+1.19^\circ\text{C}$ per century, which is higher than the corresponding value for the North Pacific ($+0.55^\circ\text{C}$ per century).

It is virtually certain (statistically significant at a confidence level of 99%) that SSTs have risen by between $+0.82$ and $+1.80^\circ\text{C}$ per century in the sea off Kushiro, the sea off Sanriku, eastern and southern parts of the sea off Kanto, the sea off Shikoku and Tokai, east of Okinawa, the central and southwestern parts of the Sea of Japan, the Yellow Sea, the East China Sea, and the sea around the Sakishima Islands (areas E1-3, S1-3, N2-3, and W1-4). It is very likely (statistically significant at a confidence level of 90%) that SSTs in the northeastern part of the Sea of Japan (area N1) have risen by $+0.34^\circ\text{C}$ per century.



Area number	Area name
E1	Sea off Kushiro
E2	Sea off Sanriku
E3	Eastern part of the sea off Kanto
S1	Southern part of the sea off Kanto
S2	Sea off Shikoku and Tokai
S3	East of Okinawa
N1	Northeastern part of the Sea of Japan
N2	Central part of the Sea of Japan
N3	Southwestern part of the Sea of Japan
W1	Yellow Sea
W2	Northern part of the East China Sea
W3	Southern part of the East China Sea
W4	Sea around the Sakishima Islands

Figure 2.8-4 Increase rates of area-averaged annual mean SSTs around Japan from 1900 to 2021 (°C per century)
 Areas with no symbol and those marked with [**] have statistical significant trend at confidence levels of 99% and 90 %.

2.9 El Niño/La Niña³⁹ and PDO (Pacific Decadal Oscillation)⁴⁰

- The La Niña event that emerged in summer 2020 continued until spring 2021. Characteristics of past La Niña events have also been observed in the equatorial Pacific since autumn 2021.
- Negative PDO index values were generally observed from around 2000 to the early 2010s, and positive values persisted in the late 2010s.

2.9.1 El Niño/La Niña

An El Niño event is a phenomenon in which sea surface temperatures (SSTs) are above normal over the equatorial Pacific from near the date line to the coast of South America for around a year. In contrast, a La Niña event is a phenomenon in which SSTs are below normal over the same area. Both events occur every few years, causing changes in global atmospheric circulations which result in abnormal weather conditions worldwide. In Japan, cooler summers and warmer winters tend to appear during El Niño events, while hotter summers and colder winters tend to appear during La Niña events.

Figure 2.9-1 shows a time-series representation of SST deviations from climatological means based on a sliding 30-year period for the El Niño monitoring region (5°N – 5°S, 150°W – 90°W) and SST deviations from reference values based on linear extrapolation with respect to the latest sliding 30-year period for the tropical western Pacific region (Eq. – 15°N, 130 – 150°E) since 2011. SSTs in the El Niño monitoring region were below related reference values from June 2020 to May 2021 and from October 2021 onward, and were near these values from June to September 2021. SSTs in the tropical western Pacific were above related reference values from June 2020 to April 2021 and from August to November 2021, and near or below these values from May to July 2021 and in December 2021. These variations are consistent with the presence of La Niña conditions from summer 2020 to spring 2021 and from autumn 2021 onward.

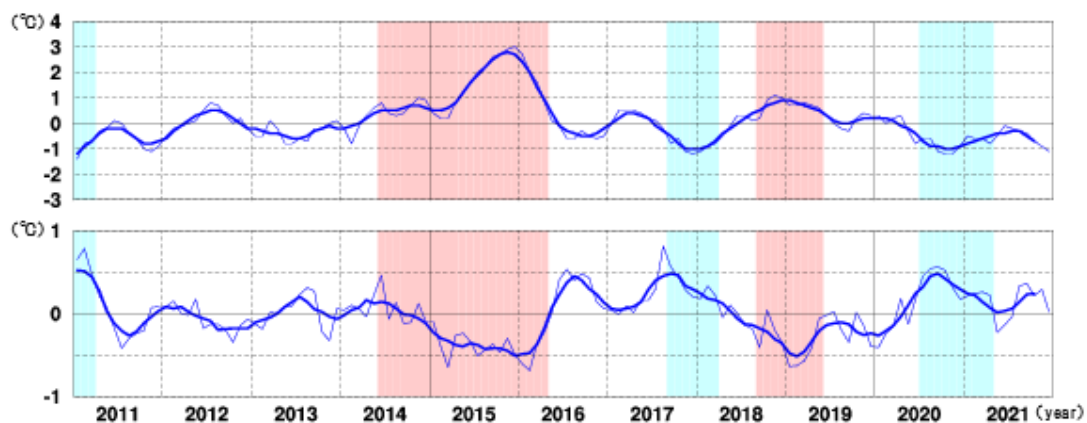


Figure 2.9-1 Time-series representations of SST deviations from the climatological mean based on a sliding 30-year period for the El Niño monitoring region (top) and SST deviations from reference values based on linear extrapolation with respect to the latest sliding 30-year period for the Western Pacific (bottom)

Thin lines indicate monthly means, and smooth thick curves indicate the five-month running mean.
Red shading denotes El Niño periods, and blue shading denotes La Niña periods.

³⁹ See the Glossary for terms relating to El Niño phenomena. Monthly diagnosis reports, ENSO monitoring products, ENSO indices and El Niño outlooks are published on JMA's website.

<https://ds.data.jma.go.jp/tcc/tcc/products/elnino/index.html>

⁴⁰ The PDO index time series is published on JMA's website.

<https://ds.data.jma.go.jp/tcc/tcc/products/elnino/decadal/pdo.html>

2.9.2 Pacific Decadal Oscillation

SST variability is also observed on time scales ranging from one to several decades in addition to El Niño/La Niña events, whose time scale is several years, and long-term trends associated with global warming. Among these, the atmosphere and oceans tend to co-vary with a period of more than ten years in the North Pacific in a phenomenon known as the Pacific Decadal Oscillation (PDO). When SSTs are lower (higher) than their normals in the central part of the North Pacific, those in its part along the coast of North America are likely to be higher (lower) than their normals. This seesaw pattern changes slowly, and appears repeatedly with a period of more than ten years. The PDO index, which is defined by the SST anomaly pattern in the North Pacific, is used as a measure of phase and strength of the oscillation. Since both the PDO index and SST anomaly patterns associated with PDO are estimated based on monthly mean SST anomalies, it is noted that they include relatively short-timescale variabilities such as El Niño/La Niña events in addition to decadal to multi-decadal components.

When the PDO index is positive (negative), SSTs in the central part of the North Pacific are likely to be lower (higher) than their normals in addition to those along the coast of North America, and those in the equatorial part from near the date line to the coast of South America are likely to be higher (lower) than normal. This tendency is analogous to the patterns observed in El Niño (La Niña) events (Figure 2.9-2). Additionally, sea level pressures (SLPs) in the high latitudes of the North Pacific are likely to be lower (higher) than their normals in the same time (Figure 2.9-3). This indicates that the Aleutian Low is stronger (weaker) than its normal in winter and spring. These atmospheric variations affect meteorological conditions mainly in North America. When the PDO index is positive, winter temperatures tend to be high in the northwestern part of North America and the northern part of South America, and low in the southeastern part of the USA and in parts of China (Mantua and Hare, 2002).

The PDO index was generally positive from the late 1920s to the early 1940s and from the late 1970s to around 2000, and was generally negative from the late 1940s to the mid-1970s and from around 2000 to the early 2010s. Positive values persisted in the late 2010s (Figure 2.9-4).

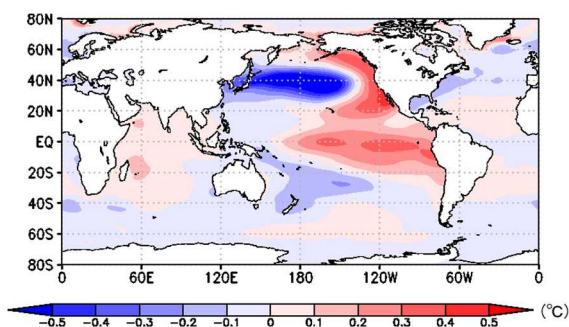


Figure 2.9-2 Typical SST anomaly patterns in the positive phase of the PDO

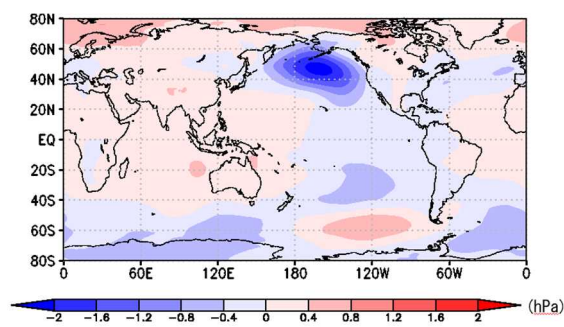


Figure 2.9-3 Typical SLP anomaly patterns in the positive phase of the PDO

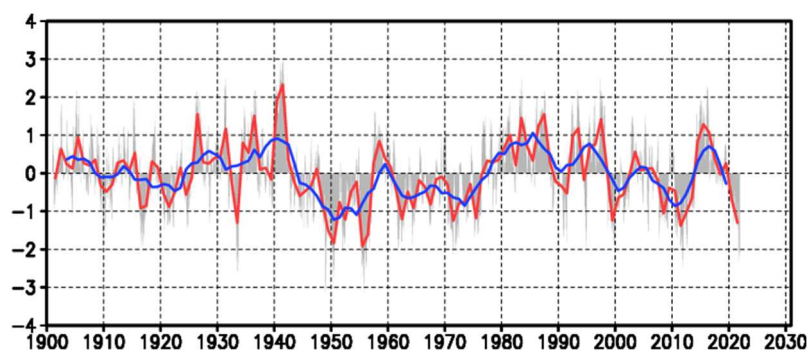


Figure 2.9-4 Time-series of the PDO index

The red line represents annual mean values for the PDO index, the blue line represents five-year running mean values, and the gray bars represent monthly values.

2.10 Sea levels around Japan⁴¹

- No significant long-term trend of sea level rise has been observed around Japan over the last 100 years.
- A trend of sea level rise has been observed since the 1980s.

Sea levels in Japanese coastal areas exhibited no significant rise from 1906 to 2021 (Figure 2.8-1).

This is attributed to variations over 10- to 20-year and 50-year-plus periods for the period from 1906 to 2021. The major factor behind sea level variations with 10- to 20-year periods is the variability of atmospheric circulation over the North Pacific. Westerlies in the mid-latitudes of the Northern Hemisphere are strengthened in boreal winter, and the consequent decadal variations in turn cause sea level variations in the central North Pacific. These propagate westward due to the earth's rotation, causing sea level rise around Japan. The high sea levels observed around 1950 were induced by a weakening of the Aleutian low.

However, a trend of sea level rise has been observed since the 1980s. The annual mean sea level around Japan in 2021 was 71 mm higher than the normal (i.e., the 1991 – 2020 average), making it the highest since 1906.

IPCC AR6 WG1 (IPCC, 2021) concluded: "heating of the climate system has caused global mean sea level rise through ice loss on land and thermal expansion from ocean warming. Global mean sea level increased by 0.20 [0.15 to 0.25] m⁴² between 1901 and 2018. The average rate of sea level rise was 1.3 [0.6 to 2.1] mm/year between 1901 and 1971, increasing to 1.9 [0.8 to 2.9] mm/year between 1971 and 2006, and further increasing to 3.7 [3.2 to 4.2] mm/year between 2006 and 2018 (high confidence). Human influence was very likely the main driver of these increases since at least 1971." In contrast to the globally averaged rate noted in the IPCC report, sea levels in coastal areas of Japan exhibited no significant rise from 1906 to 2018. Recent rates of rise around the country have been 2.9 [0.8 to 5.0] mm/year from 2006 to 2018. These figures are comparable to those observed for the global average in recent years.

Sea levels along the coast of Japan are predominantly variable with decadal cycles, but the contributions of these variations and changes associated with global warming have not been quantitatively evaluated. Continuous monitoring is needed to determine the long-term trend of sea level rise caused by global warming.

⁴¹ Sea levels around Japan are published on the JMA's website.
https://www.data.jma.go.jp/gmd/kaiyou/english/sl_trend/sea_level_around_japan.html

⁴² The values in square brackets show the 90% uncertainty range.

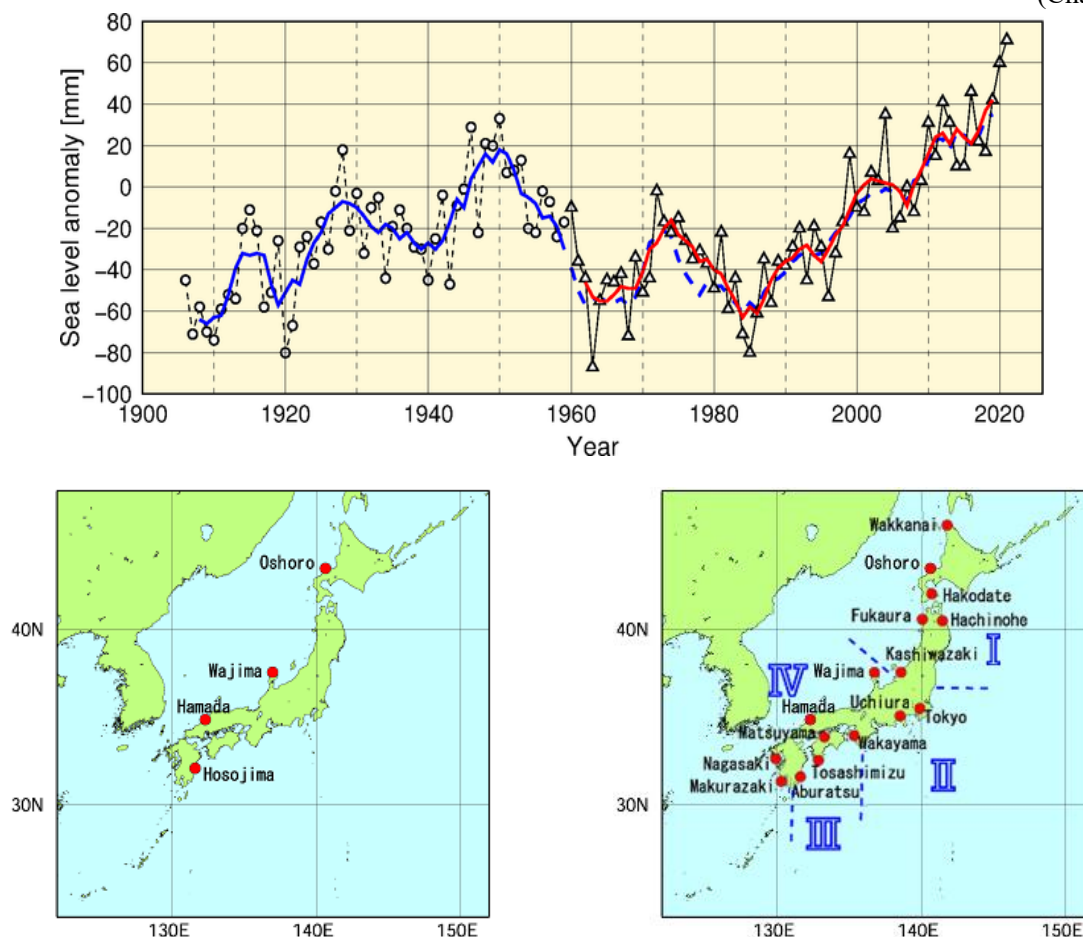


Figure 2.10-1 Time-series representation of annual mean sea levels (1906 – 2021) and locations of tide gauge stations

Tide gauge stations assessed as being affected to a lesser extent by crustal movement are selected. The four stations shown on the map on the left are used for the period from 1906 to 1959, and the sixteen shown on the right are used for the period since 1960. From 1906 to 1959, a time-series representation of mean annual mean sea level anomalies for the selected stations is shown. For the period since 1960, the nation's islands were then divided into four regions based on sea level variation characteristics, annual mean sea level anomalies were averaged for each of the regions, and the variations were plotted in the figure. The four regions are I: from Hokkaido to Tohoku district; II: from Kanto to Tokai district; III: from the Pacific coast of Kinki to that of Kyushu district; and IV: from Hokuriku to East China Sea coast of Kyushu district. Sea level variations are plotted on the chart as a time-series representation of annual mean sea level anomalies for each year, obtained using the 1991 to 2020 average as the normal. The solid blue line represents the five-year running mean of annual sea level anomalies averaged among the four stations shown in the lower left map, while the solid red line represents that averaged among the four divided regions in the lower right map. The dashed blue line represents the value averaged among the four stations shown in the lower left map for the same period shown by the solid red line (after 1960) for reference. The coefficient of correlation between the solid red line and the dashed blue line from 1962 to 2019 is as high as 0.99. Accordingly, the extent to which changing the tide gauge stations used in the monitoring affects the analysis of variance of sea level anomalies can be regarded as small. Among the tide gauge stations, those at Oshoro, Kashiwazaki, Wajima and Hosojima belong to the Geospatial Information Authority of Japan. Sea level data for the Tokyo station are available from 1968 onward. Sea level data for the period from 2011 to 2021 from Hakodate, Fukaura, Kashiwazaki, Tokyo and Hachinohe were not used due to possible influences from the 2011 off the Pacific coast of Tohoku Earthquake.

2.11 Sea ice⁴³

- The sea ice extent in the Arctic Ocean is decreasing.
- The annual maximum sea ice extent in the Antarctic Ocean is extremely likely to increase.
- The maximum sea ice extent in the Sea of Okhotsk shows a decreasing trend of $0.058 \times 10^6 \text{ km}^2$ per decade.

2.11.1 Sea ice in Arctic and Antarctic areas

Sea ice is formed when sea water in the Arctic and Antarctic freezes. As the albedo (reflection coefficient) of sea ice is greater than that of the ocean surface, sea ice extent reductions caused by global warming result in more solar energy absorption at the surface, which in turn accelerates global warming. Sea ice also affects deep-ocean circulation because the expelled salt as it forms increases the salinity (and therefore the density) of the water below it causing the water to sink.

It is virtually certain that there has been a long-term trend of decrease in sea ice extent in the Arctic Ocean since 1979 when continuous monitoring of sea ice using satellite sensors with similar properties started (statistically significant at a confidence level of 99%). In particular, the reduction in the annual minimum extent is notable. The rate of decrease in the annual minimum up to 2021 was $0.089 \times 10^6 \text{ km}^2$ per year. Meanwhile, it is extremely likely that there has been a long-term trend of increase in sea ice extent at a rate of $0.014 \times 10^6 \text{ km}^2$ per year in the annual maximum sea ice extent in the Antarctic Ocean (statistically significant at the confidence level of 95%) and it is very likely that there has been a long-term trend of increase in sea ice extent at a rate of $0.009 \times 10^6 \text{ km}^2$ per year in the annual mean sea ice extent in the Antarctic Ocean (statistically significant at the confidence level of 90%). There has been no discernible trend in the minimum sea ice extent in the Antarctic Ocean⁴⁴.

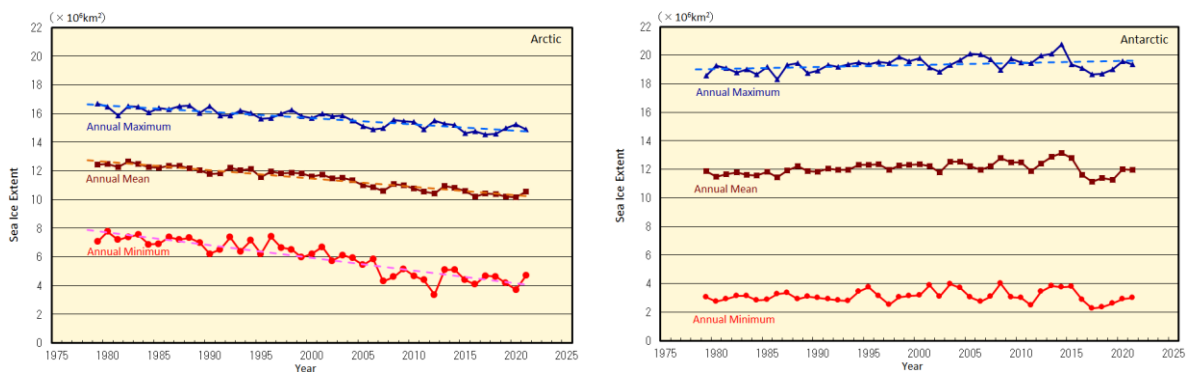


Figure 2.9-1 Time-series representations of annual maximum, annual mean, and annual minimum sea ice extent in the Arctic Ocean (including the Sea of Okhotsk and the Bering Sea) (left) and in the Antarctic Ocean (right) from 1979 to 2021

The solid blue, brown and red lines indicate the annual maximum, the annual mean, and the annual minimum sea ice extent, respectively. The dashed lines indicate the linear trends (statistically significant at the confidence level of 95%). Sea ice extents are calculated from brightness temperature data provided by NASA (the National Aeronautics and Space Administration) and NSIDC (the National Snow and Ice Data Center).

⁴³ Information on sea ice in the Arctic/Antarctic, and in the Sea of Okhotsk are published on JMA's website.

https://www.data.jma.go.jp/gmd/kaiyou/english/seaice_global/series_global_e.html (Arctic/Antarctic)

https://www.data.jma.go.jp/gmd/kaiyou/english/seaice_okhotsk/series_okhotsk_e.html (Sea of Okhotsk)

⁴⁴ It was reported in IPCC AR6 WG1 (2021) that there has been no significant trend in Antarctic sea ice area from 1979 to 2020 due to regionally opposing trends and large internal variability.

In 2021, the annual maximum Arctic sea ice extent was $14.91 \times 10^6 \text{ km}^2$ on March 8, marking the seventh-lowest value since 1979. The extent subsequently decreased during spring and summer in the Northern Hemisphere and reached its annual minimum of $4.71 \times 10^6 \text{ km}^2$ on September 11, marking the twelfth-lowest value since 1979. Meanwhile, the Antarctic sea ice extent was at its annual minimum of $3.01 \times 10^6 \text{ km}^2$ on February 17, marking the eighteenth-lowest value since 1979. The extent subsequently increased during the autumn and winter months of the Southern Hemisphere and reached its annual maximum of $19.34 \times 10^6 \text{ km}^2$ on August 30, marking the twenty-second-lowest (twenty-second-highest) value since 1979 (Figures 2.9-1, 2.9-2, 2.9-3).

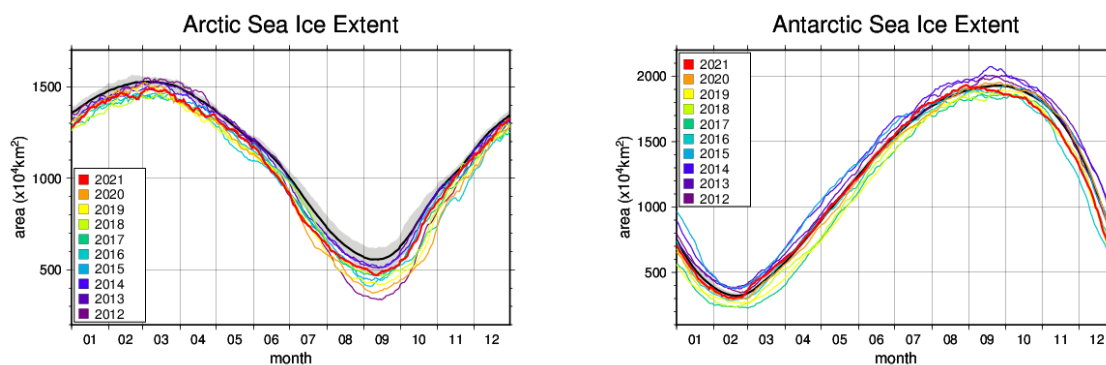


Figure 2.9-2 Annual variations of sea ice extent in the Arctic (left) and Antarctic (right) areas in 2021 (red line)
Black lines represent the normal, and shading represents the range of the normal.

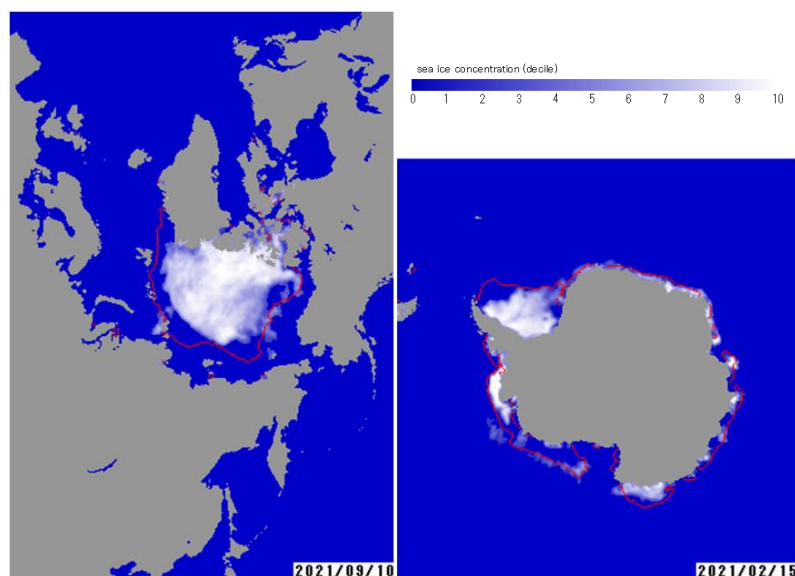


Figure 2.9-3 Annual minimum sea ice distribution for the Arctic and Antarctic

The figure on the left shows Arctic sea ice concentration on September 10 2021, and on the right is Antarctic sea ice concentration on February 15 2021. The red lines represent the normal sea ice edge for the relevant days.

2.11.2 Sea ice in the Sea of Okhotsk

The Sea of Okhotsk is the southernmost sea in the Northern Hemisphere where sea ice is observed across a wide area. The variation of the sea ice in the Sea of Okhotsk has effect on climate in coastal area facing the Sea of Okhotsk in Hokkaido and water quality of Oyashio.

The maximum⁴⁵ sea ice extent in the Sea of Okhotsk shows large interannual variations. However, it is virtually certain that it exhibited a long-term trend of decrease for the period from 1971 to 2021 (statistically significant at the confidence level of 99%). The maximum extent has decreased by $0.058 \times 10^6 \text{ km}^2$ per decade (corresponding to 3.7% of the Sea of Okhotsk's total area).

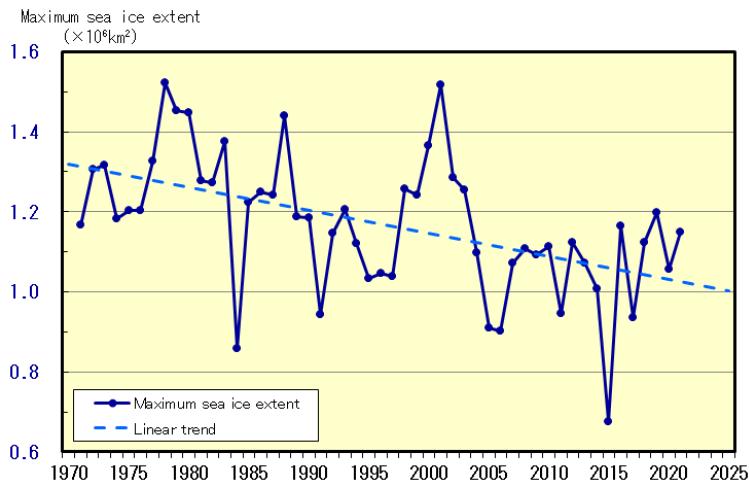


Figure 2.9-4 Time-series representations of maximum sea ice extent for the Sea of Okhotsk from 1971 to 2021

Straight line indicates the linear trend.

⁴⁵ The maximum sea ice extent: It shows sea ice extent that sea ice was the most expanding of every five days in the winter.

2.12 Ocean carbon dioxide and ocean acidification

- Concentrations of carbon dioxide in the air and in the oceans are increasing.
- Anthropogenic carbon dioxide is absorbed into the ocean and accumulates there.
- Oceanic acidity has increased due to accumulation of anthropogenic carbon dioxide.

The ocean acts as a large sink for CO₂ emitted as a result of human activity, and the chemical properties of seawater have changed due to the uptake and reserve of anthropogenic CO₂. Ocean acidification, known as the decrease in ocean pH (hydrogen ion exponents), is a particular issue of concern because it accelerates global warming by limiting the ocean's capacity of CO₂ uptake from the atmosphere and affects marine ecosystems by disturbing plankton growth. Numerical model experiments based on future CO₂ emission estimates show an ocean surface pH decrease of 0.16 – 0.44 from the end of the 19th century to the end of the 21st century (IPCC AR6: IPCC 2021). The CO₂ absorbed by the ocean is considered to have been transported into the ocean interior through ocean circulation and biological processes, and to be causing ocean acidification in the interior as well as in the surface layer (Doney et al., 2009).

2.12.1 Ocean carbon dioxide

(1) Ocean carbon dioxide in the western North Pacific

Based on data collected by JMA research vessels along the 137°E (3 – 34°N) and 165°E (5°S – 35°N) lines, oceanic and atmospheric $p\text{CO}_2$ are increasing in the western North Pacific area (Figures 2.12-1, 2.12-2). The growth rates for oceanic and atmospheric $p\text{CO}_2$ along the 137°E line from 1985 to 2021 were 1.5 – 2.1 and 1.8 – 2.0 $\mu\text{atm}/\text{year}$, respectively, while those along the 165°E line from 1996 to 2021 were 1.8 – 2.8 and 1.8 – 2.1 $\mu\text{atm}/\text{year}$, respectively. Oceanic $p\text{CO}_2$ exhibits seasonal variations, being higher in summer with higher SSTs and lower in winter with lower SSTs, and the range of variation is more volatile at higher latitudes along both lines. Meanwhile, atmospheric $p\text{CO}_2$ is constant and higher than those of oceanic $p\text{CO}_2$ except in summer. Consequently, the ocean absorbs atmospheric CO₂ emissions overall, other than in equatorial areas, resulting in a release of CO₂ into the atmosphere over the year because oceanic $p\text{CO}_2$ values are higher than those of atmospheric $p\text{CO}_2$.

The column inventory of ocean CO₂ was estimated using long-term time-series data on dissolved inorganic carbon from 1990s (Figure. 2.12-3). The column inventory rates of ocean CO₂ between the sea surface and 27.2 σ_θ (approx. 1,000 m in depth) along 137°E and 165°E are approximately 4 – 11 $\text{tC}\cdot\text{km}^{-2}\cdot\text{year}^{-1}$. The column inventory rates of ocean CO₂ around 20 – 30°N are higher than those at 10°N and 35°N. This is caused by the transport of CO₂ from the surface to the ocean interior by water masses known as North Pacific subtropical mode water and North Pacific intermediate water.

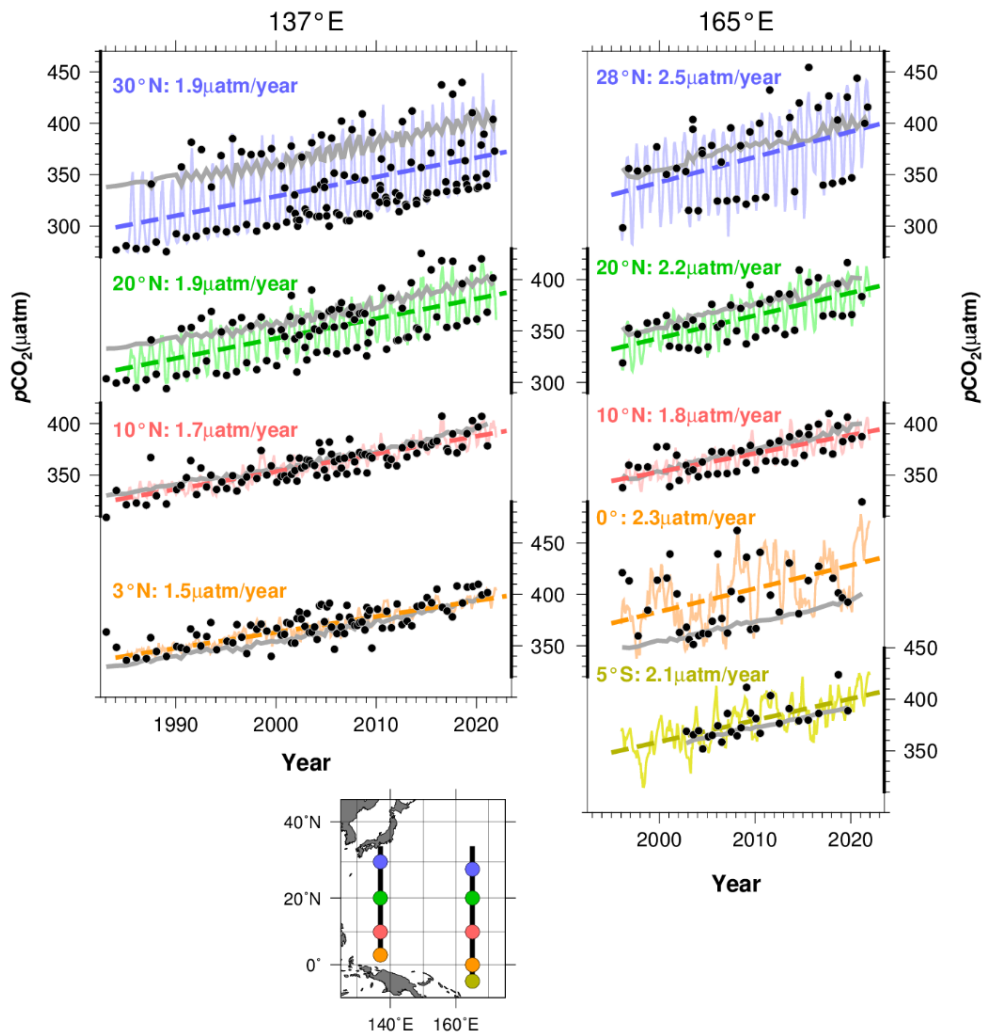


Figure 2.12-1 Annual changes in oceanic and atmospheric $p\text{CO}_2$ along the 137°E (left) and the 165°E (right) lines
 Black plots show oceanic $p\text{CO}_2$ observation values. Solid lines represent monthly oceanic $p\text{CO}_2$ values reconstructed using the method of Ishii et al. (2011), dashed lines show the long-term trend of oceanic $p\text{CO}_2$, and gray lines indicate the observed values of atmospheric $p\text{CO}_2$.

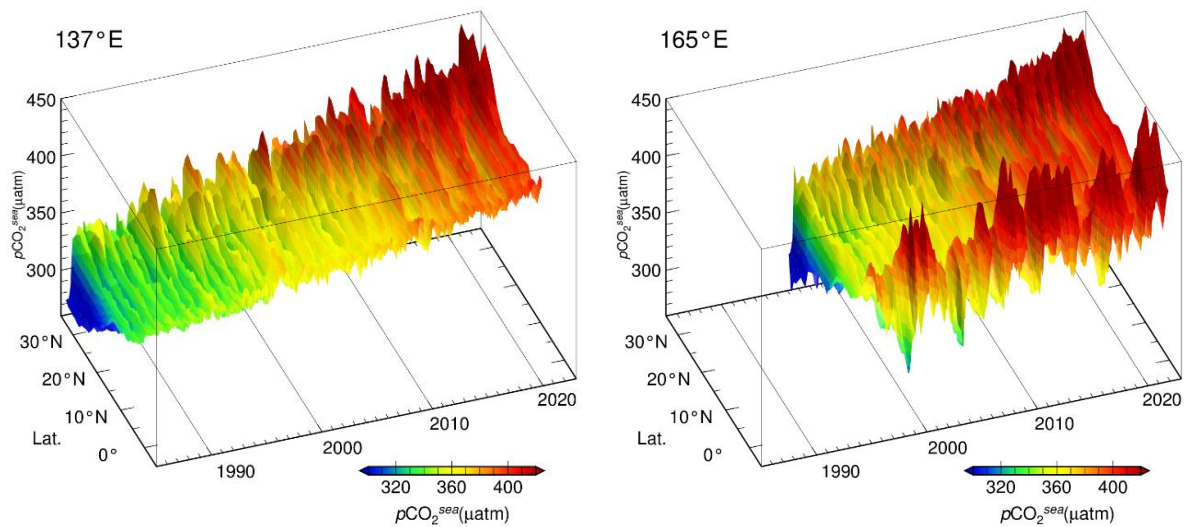


Figure 2.12-2 Time-latitude distribution of oceanic $p\text{CO}_2$ along the 137°E (left) and the 165°E (right) lines
 Colors indicate reconstructed monthly oceanic $p\text{CO}_2$ value. The part on the left shows oceanic $p\text{CO}_2$ along the 137°E (3-34°N) since 1985 and the part on the right shows oceanic $p\text{CO}_2$ along the 165°E (5°S-35°N) since 1996.

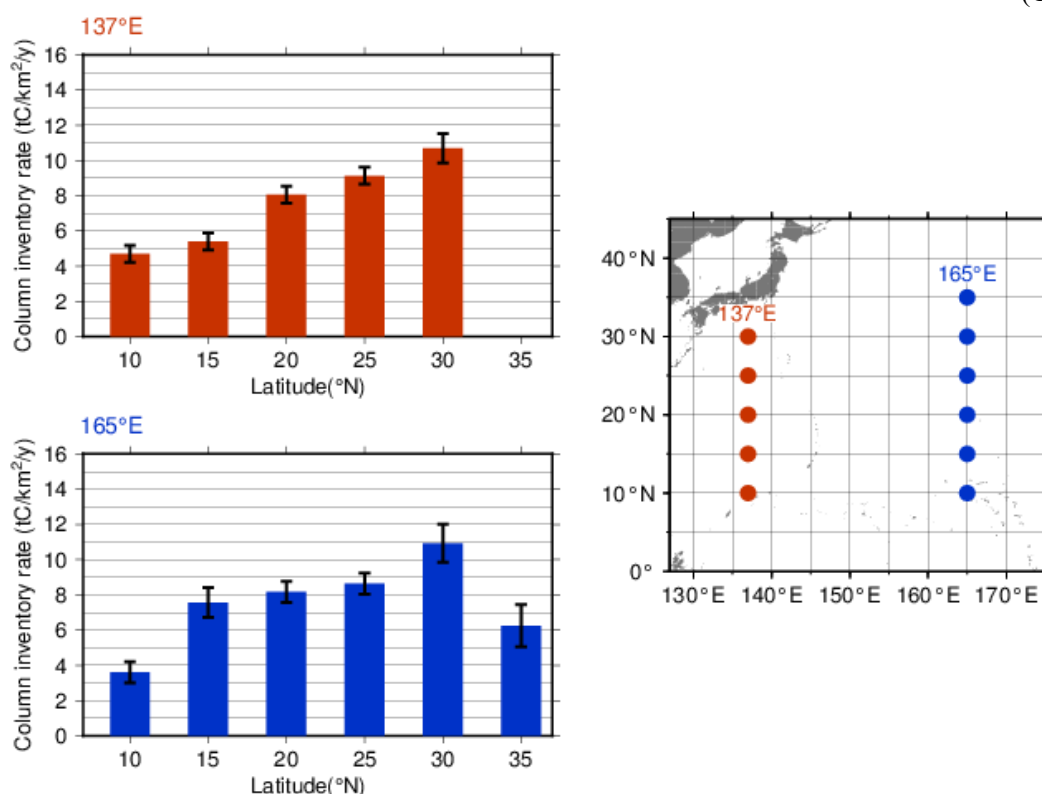


Figure 2.12-3 Changes in ocean CO₂ between the sea surface and 27.2 σ_{θ} (approx. 1,000 m in depth) along 137 and 165°E for the periods 1994 – 2021 and 1992 – 2021.

Error bars denote a 95% confidence level

(2) Global ocean carbon dioxide uptake

Analysis of observation data reveals relationships between surface ocean CO₂ concentrations and other oceanographic parameters such as sea surface temperature (SST), salinity and chlorophyll-a concentration, which differ by region. Global ocean CO₂ concentrations were estimated using datasets of such parameters based on these relationships, and CO₂ exchanges between the atmosphere and the ocean were calculated (Iida *et al.*, 2021). It was found that the ocean releases CO₂ into the atmosphere in equatorial regions and the northern Indian Ocean, where seawater with a high CO₂ concentration upwells and absorbs CO₂ in other regions (Figure 2.12-4 (a)). Lower SSTs in winter and biological CO₂ consumption in spring/autumn result in lower surface ocean CO₂ concentrations and therefore higher CO₂ uptake, especially in the mid-to-high latitudes. Figure 2.12-4 (b) and (c) show monthly and annual variations in global ocean CO₂ uptake, respectively. The estimated mean annual global ocean CO₂ uptake during 1990 to 2020 was 2.1 GtC per year. Considering natural CO₂ efflux of 0.6 GtC per year (IPCC, 2021), which results from riverine input to the oceans, the amount of ocean CO₂ uptake corresponds to 30 % of all anthropogenic CO₂ emission, which IPCC (2013) estimates to be 9.4 GtC per year. Global ocean CO₂ uptake is affected by the variability of global SST distribution and biological activity, and decreases/increases in boreal summer/winter (Figure 2.12-4 (b)). The estimated annual global ocean CO₂ uptake has increased during the period.

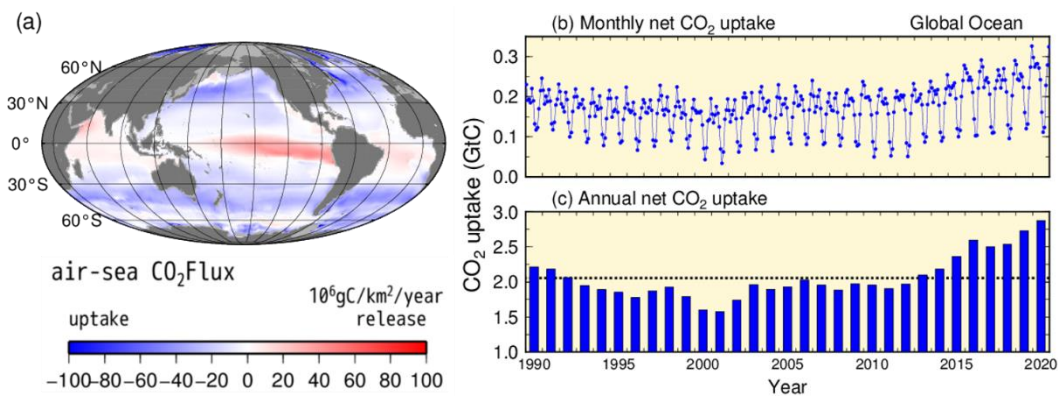


Figure 2.12-4 Distribution of global ocean CO₂ uptake/release for 2020 (a) and time-series representations of monthly (b) and annual (c) CO₂ uptake from 1990 to 2020

The blue/red area in the map on the left (a) indicates ocean uptake/release of CO₂ from/into the atmosphere. The grey area shows the border of the region analyzed. The dotted line in graph (c) shows the 2.1 GtC average for the period from 1990 to 2020.

2.12.2 Ocean acidification

(1) Ocean acidification around Japan

To monitor the long-term variability of ocean acidification, JMA has analyzed monthly sea surface pH values since 1998 based on data from its oceanographic observations and related database content. The results show a clear trend of in-situ pH decrease in seas around Japan ranging from 0.016 per decade around Kyushu and Okinawa to 0.023 per decade in the Sea of Japan. The average trend in sea areas around Japan is 0.020 per decade. These values are similar to observed rates of pH decrease in worldwide open oceans as recorded in the IPCC special report (SROCC; IPCC, 2019).

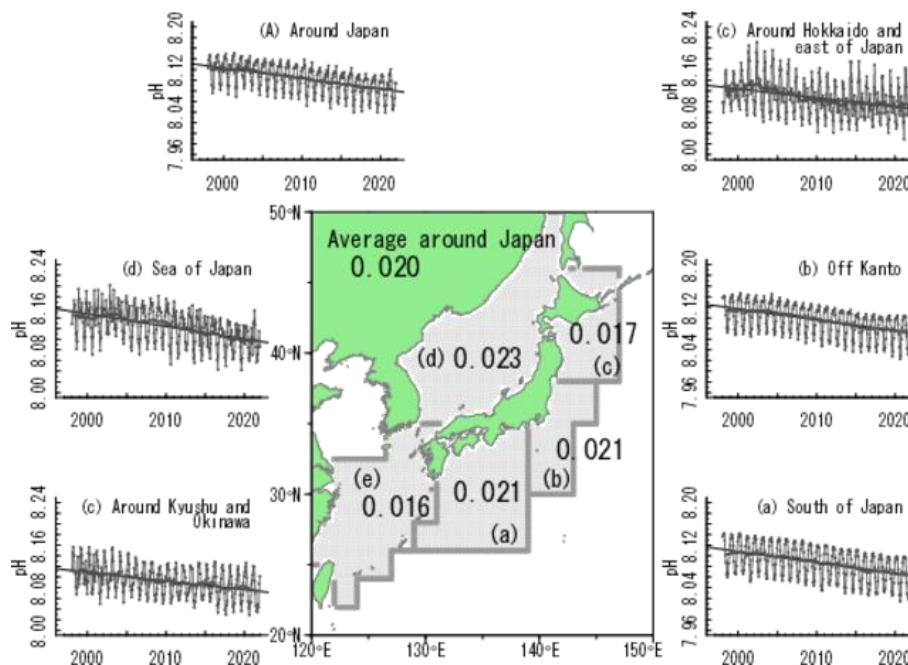


Figure 2.12-5 Long-term trends of pH in sea areas around Japan

Black points with lines, bold lines and thin lines indicate average pH values, yearly running means and long-term trends in areas (a) to (e), and the average around Japan, respectively.

(2) Ocean acidification in the western North Pacific

JMA monitors long-term trends in surface and interior ocean pH along repeat hydrographic lines at 137°E and 165°E, and performs analysis to determine the average decrease in surface ocean pH throughout the Pacific using data on oceanic CO₂ concentration and related factors. The results clearly show a decreasing trend in surface ocean pH for the whole Pacific, and 0.014 to 0.021 and 0.016 to 0.028 per decade at individual stations on the 137°E and 165°E lines, respectively (Figures 2.12-6 and 2.12-7). Ocean interior pH along these lines also shows decreasing trends of 0.011 to 0.031 per decade (Figure 2.12-8) with higher rates in the northern than the southern subtropics due to greater accumulation of anthropogenic CO₂ in the former.

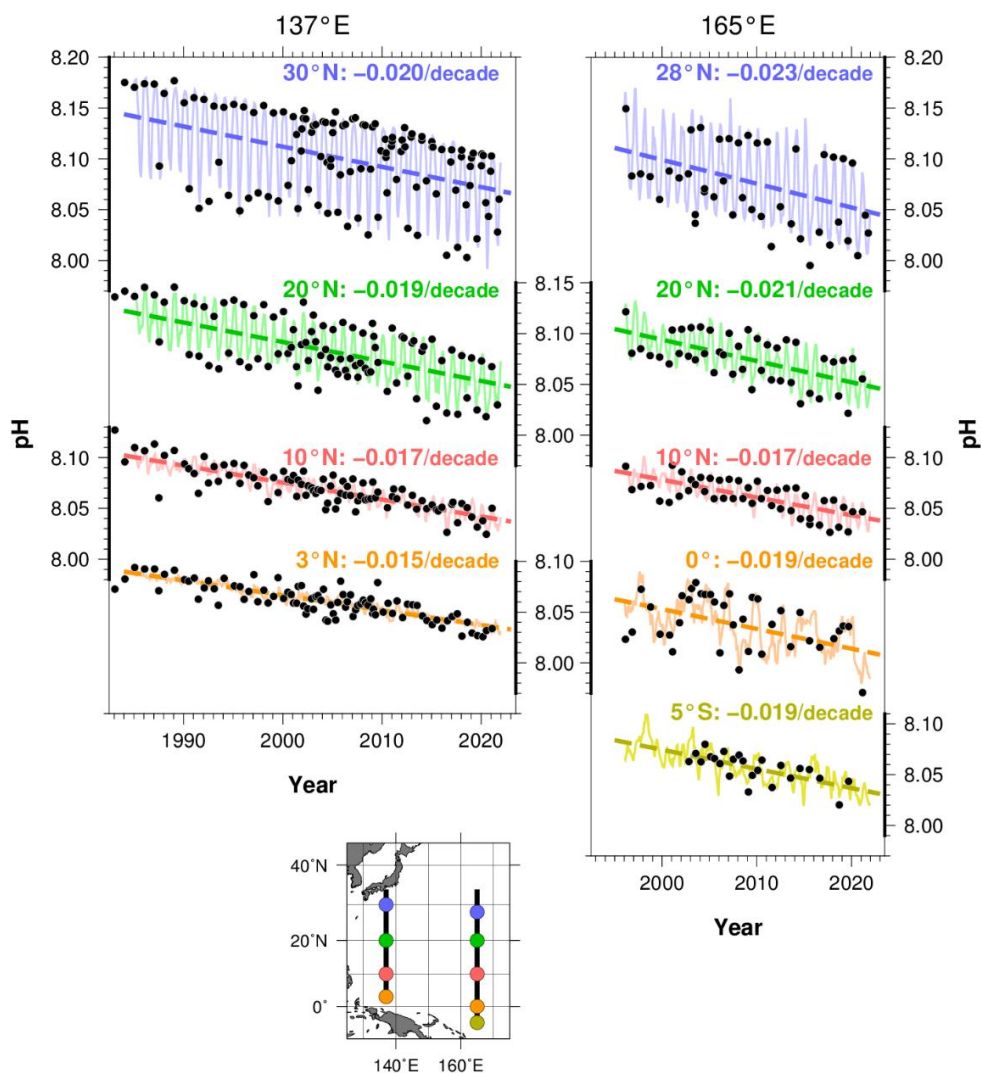


Figure 2.12-6 Long-term trends of pH at each latitude in JMA's repeat hydrographic lines at 137°E (left) and 165°E (right)

Black plots show pH observation values based on $p\text{CO}_2$ observation data. Solid lines represent monthly pH values reconstructed using the method of Ishii et al. (2011), dashed lines show the long-term trend of pH, and numbers indicate rates of change at each latitude.

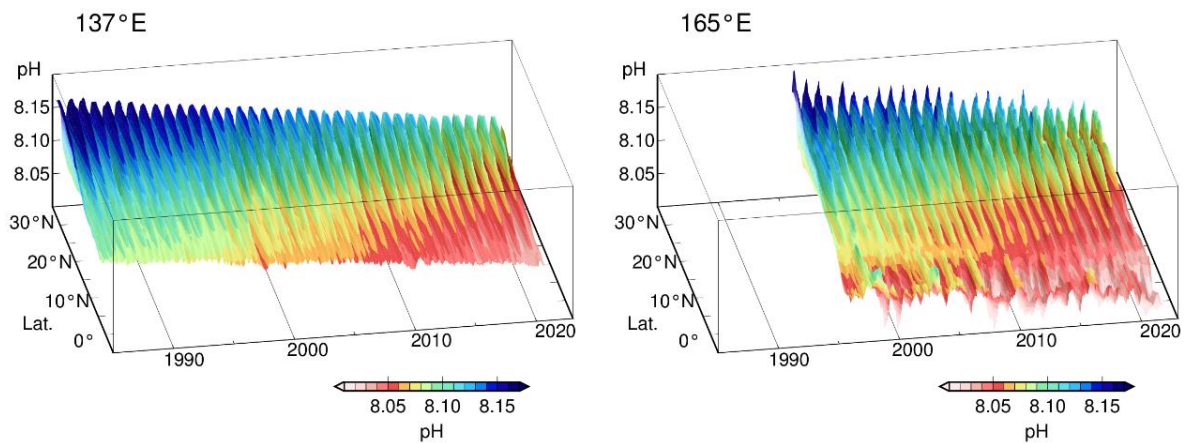


Figure 2.12-7 Time-latitude distribution of pH along the 137°E (left) and the 165°E (right) lines
 Colors indicate reconstructed monthly pH values. The part on the left shows pH along 137°E (3-34°N) since 1985, and the part on the right shows pH along 165°E (5°S-35°N) since 1996.

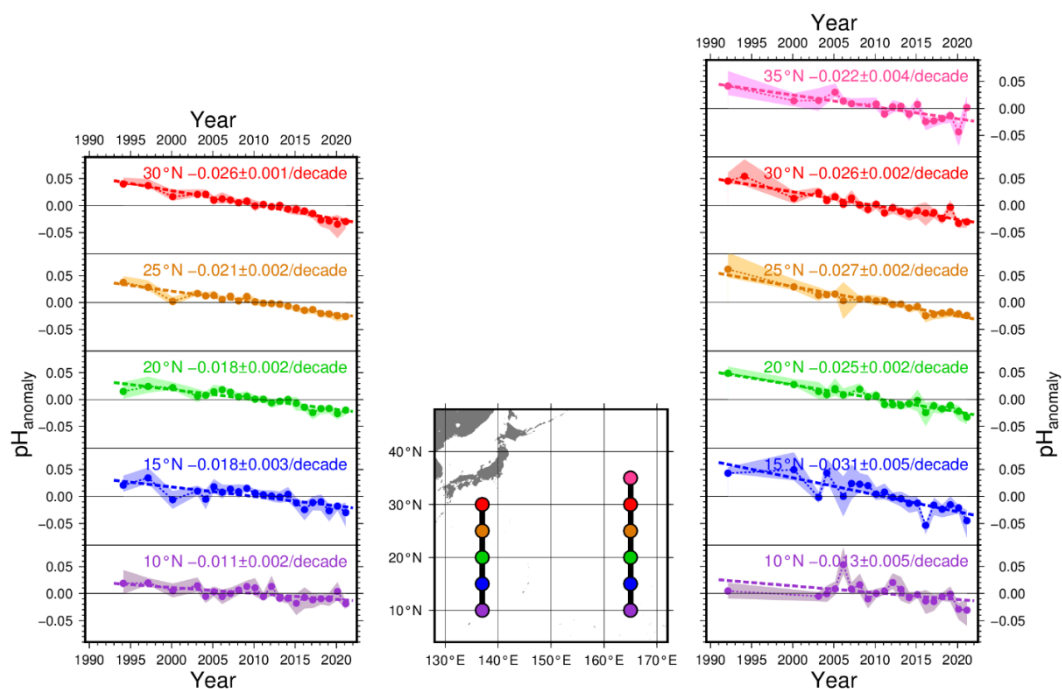


Figure 2.12-8 Long-term trends of pH between 25.0 σ_θ and 26.9 σ_θ (a depth range of about 150-800 m) along 137°E (left) and 165°E (right)

Plots show pH anomalies from averages for the whole period on the isopycnals at each latitude. The shaded areas and bold dotted lines represent the standard deviation range ($\pm 1 \sigma$) and the long-term trend, respectively. The numbers indicate rates of change at each latitude.

(3) Ocean acidification in the global ocean

JMA has analyzed monthly sea surface pH values since 1990 using a global oceanographic observation database via the method outlined in 2.12-1 (2). The results show a clear trend of in-situ pH decrease at 0.018 per decade in the global ocean. The rates of decrease are 0.018, 0.018 and 0.020 pH per decade in the Pacific, the Atlantic and the Indian Ocean, respectively.

The pH in surface ocean waters varies by area due to differences in ocean circulation, biological activity and seasonal change. In the equatorial area, upwelling CO₂-rich seawater causes relatively low pH values. Subtropical (subpolar) areas show higher pH values than equatorial areas with seasonal changes of higher (lower) pH in winter and lower (higher) pH in summer.

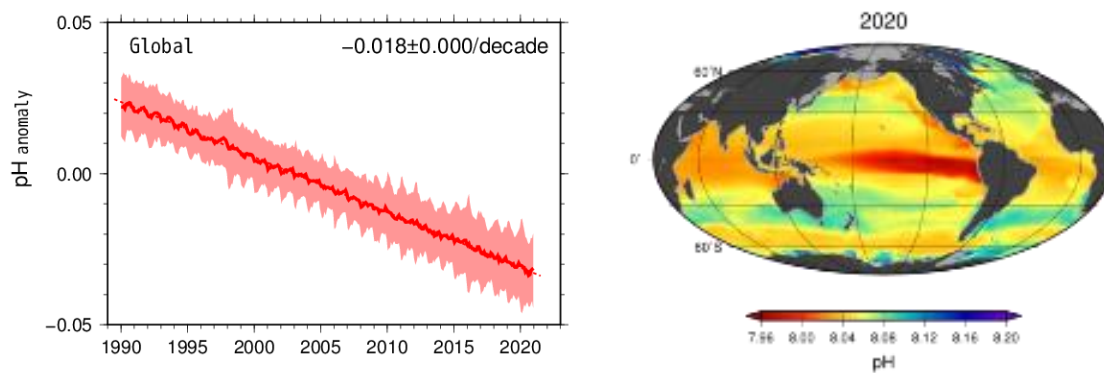


Figure 2.12-9 Long-term trend of surface ocean pH (left) and pH distribution in 2020 (right) in the global ocean
Left: Rate of pH change in the global ocean. The solid line is a time-series representation of the pH anomaly from the average from 1991 to 2020 in the global ocean. The shaded area and dotted line represent the standard deviation range ($\pm 1\sigma$) and the long-term trend, respectively. The ' \pm ' symbol indicates a 95% confidence interval.
Right: Lower pH values are represented as warmer colors.

Explanatory note on detection of statistical significance in long-term trends

Meteorological observation data, including those relating to temperature and precipitation, are subject to large amplitude fluctuations due to the influence of atmospheric and oceanic dynamics on a broad spectrum of spatial and temporal scales. To examine the possible presence of long-term climate system trends associated with global warming in consideration of natural variability, raw climate data need to be converted into suitable statistical time-series representations and subjected to statistical testing in order to highlight the likelihood of systematic temporal trends that cannot be explained by random variability alone. When the results of such testing allow reasonable conclusion that random variability is unlikely to be the sole factor at work, a change is described as statistically significant.

In this report, the likelihood of a systematic long-term change existing in a time-series representation is based on the results of statistical significance testing performed at confidence levels of 99, 95 and 90%. The following terminology summary describes each level:

Level of confidence	Term
$\geq 99\%$	Virtually certain to have increased/decreased (statistically significant at a confidence level of 99%)
$\geq 95\%$	Extremely likely to have increased/decreased (statistically significant at a confidence level of 95%)
$\geq 90\%$	Very likely to have increased/decreased (statistically significant at a confidence level of 90%)
$< 90\%$	No discernible trend

The following statistical methods are applied for the data used in this report:

- i) For statistical variables whose annual fluctuation component can be assumed to follow normal distribution
 For temperature anomalies, trend-removed annual variability data are expected to approximately follow normal distribution. T-testing is performed for statistical variables assumed to be normally distributed using a coefficient of correlation between years and values.
- ii) For statistical variables whose annual fluctuation component cannot be assumed to follow normal distribution
 The assumption of normality may not be applicable to frequency statistics regarding weather conditions, including those for extremely warm days, tropical nights and hourly precipitation amounts exceeding 50 mm. Accordingly, non-parametric testing, which does not depend on underlying assumptions about distribution, is applied to such variables.

It should be noted that statistical tests are in theory inevitably susceptible to the establishment of false conclusions even if the results indicate a statistically significant trend. Even outcomes indicating statistical significance at confidence levels of 90, 95 or 99% imply that there are small inherent probabilities of up to 10,

5 and 1%, respectively, of the significance being erroneously detected when in fact the observed long-term change occurred by mere random chance. Conversely, when a systematic long-term change actually exists, statistical testing may fail to detect the significance correctly. In general, test results are not considered highly stable if they are based on observation records that are temporally limited, influenced by large annual fluctuations/rare events or subject to change when new observations are added to a data sequence. Readers are encouraged to interpret the analytical results presented in the report appropriately with due note of these considerations.

Glossary

Aerosols

Aerosols are airborne solids or liquids in fine particle form. Their many types include particles of natural origin blown up from land/sea surfaces, anthropogenic particles and secondary aerosols formed from anthropogenic and biogenic precursors. In addition to absorbing and scattering sunlight, they also provide condensation nuclei for clouds. Particulate matter 2.5 (PM2.5) is the name given to aerosol particles measuring 2.5 micrometers or less in diameter (about 30 times thinner than a human hair), and is considered to have possible adverse effects on human health when inhaled.

Anthropogenic

Resulting from or produced by human activity.

Arctic Oscillation

The Arctic Oscillation (AO) is a major atmospheric circulation variation exhibiting an annular pattern of sea-level pressure anomalies in a seesaw fashion with one sign over the Arctic region and the opposite sign over the mid-latitudes. Its negative phase, which is characterized by positive and negative sea-level pressure anomalies over the Arctic region and the mid-latitudes, respectively, helps cold Arctic air move into the mid-latitudes. The positive phase, whose sea-level pressure anomaly pattern is reversed, keeps Arctic air over the Arctic region.

Extreme climate event

In general, an extreme climate event is recognized as an unusually severe or rare climate event creating disaster conditions or exerting significant socio-economic influence. The definition includes severe weather conditions covering periods ranging from only a few hours (such as heavy rain or strong wind) to several months (such as drought or cold summer conditions). JMA defines extreme climate events as those occurring once every 30 years or longer.

IPCC (Intergovernmental Panel on Climate Change)

The Intergovernmental Panel on Climate Change (IPCC) is an international organization established by the United Nations Environment Programme (UNEP) and the World Meteorological Organization (WMO) in 1988. It reviews and assesses scientific, technical and socio-economic information on climate change, the potential impacts of such change and related vulnerability, and options for adaptation and mitigation, in collaboration with scientists and experts on an international basis. The Panel's reports highlight common understanding of such information to support political matters such as treaty negotiations on global warming.

Kosa (Aeolian dust)

Kosa (Aeolian dust) is a meteorological phenomenon in which fine dust is blown up to an altitude of several thousand meters by cyclonic or other wind systems from deserts or cropland in semi-arid areas of the Asian continent, and is transported over long distances by westerly winds, resulting in haze or dustfall in downstream areas. It is often observed between March and June in Japan and makes the sky yellow and hazy. Heavy Kosa can affect transportation by obstructing visibility.

Monsoon

The term *monsoon* primarily refers to seasonally reversing winds, and by extension includes related seasonal rainfall change with wet and dry phases. Monsoon climate regions where seasonal winds prevail are found in numerous places around the world, with a major one located over a broad area from the Asian continent to northern Australia.

Normals

Normals represent climatic conditions at meteorological stations, and are used as a base to evaluate meteorological variables (e.g., temperature, precipitation and sunshine duration) and produce generalizations (e.g., cool summer, warm winter and dry/wet months) for particular periods. JMA uses averages for the most recent three decades (currently 1991 – 2020) as normals, which are updated every decade in line with WMO Technical Regulations.

Terms relating to surface temperature variations

El Niño/La Niña events: In an El Niño event, sea surface temperatures (SSTs) are higher than normal across a wide region from near the date line to the area off the coast of South America in the equatorial Pacific for about a year. In a La Niña event, SSTs are lower than normal in the same area. Both occur every few years, and are associated with frequent extreme climate conditions worldwide.

JMA recognizes the occurrence of an El Niño event when the five-month running mean of SST deviations from the climatological means (based on a sliding 30-year period averaged over the NINO.3 El Niño Monitoring Region (5°N – 5°S, 150°W – 90°W; Figure A)) remains +0.5°C or above for a period of six months or more. Similarly, a La Niña event is recognized when the corresponding figure is –0.5°C or below for the same area/period.

Figure B shows typical SST deviations from the normal during El Niño and La Niña events. The dark red and blue shading seen from the date line to the coast of South America indicates large deviations.

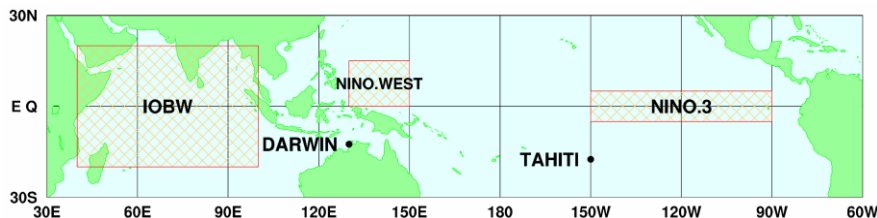


Figure A El Niño monitoring regions

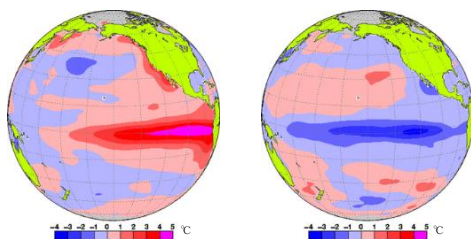


Figure B Left: monthly mean SST anomalies for El Niño (November 1997); right: for La Niña (December 1998)

Red and blue shading represents positive and negative SST deviations, respectively. Darker shading indicates larger deviations. The unit of temperature is degrees Celsius.

Southern Oscillation: El Niño and La Niña events are closely related to trade winds (easterlies blowing around the tropical Pacific), which tend to be weak during the former and strong during the latter. The strength of such winds is closely related to the sea level pressure difference between eastern and western parts of the Pacific. This pressure difference varies in a phenomenon known as the Southern Oscillation. El Niño/La Niña events and the Southern Oscillation are not independent of each other; they are different manifestations of the same phenomenon involving atmospheric and oceanic interaction, and are referred to as ENSO (El Niño – Southern Oscillation) for short.

Pacific Decadal Oscillation (PDO): A phenomenon in which variables in the atmosphere and oceans tend to co-vary with a period of more than ten years in the North Pacific. When sea surface temperatures are lower (higher) than their normals in the central part of the North Pacific, those in its part along the coast of North America are likely to be higher (lower) than their normals, and sea level pressures in the high latitudes of the North Pacific are likely to be lower (higher) than their normals. These atmospheric variations affect meteorological conditions in North America and elsewhere.

Indian Ocean Dipole mode (IOD) event: A phenomenon in which sea surface temperatures (SSTs) are below normal in the south eastern part of tropical Indian Ocean (off the Sumatra Island) and above normal in the western part during the northern hemisphere summer and autumn (June - November). This east-west contrast of SST anomaly pattern is called dipole mode. On the other hand, a phenomenon in which SSTs are above normal off the Sumatra Island and below normal in the western part is called negative IOD event. These phenomena affect the climate near Japan and Australia through the changes of atmospheric circulation caused by atmospheric active (inactive) convections over above (below) normal SST area.

Terms relating to the greenhouse effect

Greenhouse effect: The earth's atmosphere contains small amounts of greenhouse gases, which absorb a large part of the infrared radiation emitted from the earth's surface and re-emit it back, thereby warming the surface. This process is known as the greenhouse effect. Without it, the earth's average surface temperature of around 14°C would be approximately –19°C. Increased concentrations of greenhouse gases enhance the greenhouse effect, thereby producing higher surface temperatures. Major greenhouse gases include carbon dioxide, methane and nitrous oxide. Although water vapor has the strongest greenhouse effect, its main influencing factor is temperature rather than emissions relating to human activity. Water vapor is not usually regarded as a greenhouse gas in the context of global warming because it is considered a feedback factor rather than a forcing factor in climate change.

Carbon dioxide: Of all greenhouse gases, carbon dioxide (CO₂) is the most significant contributor to global warming. Since the start of the industrial era in the mid-18th century, its atmospheric concentration has increased as a result of emissions associated with human activity, such as fossil fuel combustion, cement production and deforestation. Around half of all cumulative anthropogenic CO₂ emissions have remained in the atmosphere. The rest was removed from the atmosphere and stored in natural terrestrial ecosystems and oceans (IPCC, 2021).

Methane: Methane (CH₄) is the second most significant greenhouse gas after CO₂, and has a significant radiative effect around 27.9 times greater than that of CO₂ per unit mass. Around 40% of CH₄ released into the atmosphere is of natural origin (wetlands, termites, etc.), and around 60% is from human-related activity sources (ruminant animals, rice paddy fields, fossil fuel mining, landfill, biomass burning, etc.) (WMO, 2021). It is primarily removed from the atmosphere via photochemical reaction with reactive and unstable hydroxyl (OH) radicals.

Nitrous oxide: Nitrous oxide (N₂O) is a significant greenhouse gas because of its large radiative effect per unit mass (about 273 times greater than that of CO₂) and its long lifetime (about 109 years) in the atmosphere. Around 60% of N₂O released into the atmosphere is of natural origin (oceans, soil, etc.), and around 40% is from human activity-related sources (biomass burning, nitrate fertilizers, various industrial processes, etc.) (WMO, 2021). It is photo-dissociated in the stratosphere by ultraviolet radiation.

Halocarbons: Halocarbons are generally carbon compounds containing halogens such as chlorine and bromine, many of which are powerful greenhouse gases whose atmospheric concentrations have increased rapidly since the second half of the 20th century due to artificial production. Although their atmospheric concentrations are only around a millionth those of CO₂, their greenhouse effect per unit mass is several thousand times greater. Chlorofluorocarbons (CFC-11, CFC-12 and CFC-113 among others), carbon tetrachloride, hydrochlorofluorocarbons (HCFCs), 1,1,1-trichloroethane, chloromethane, halons and bromomethane are greenhouse gases and ozone-depleting substances (ODSs). Hydrofluorocarbons (HFC-134a, HFC-152a, etc.) are also included in the definition.

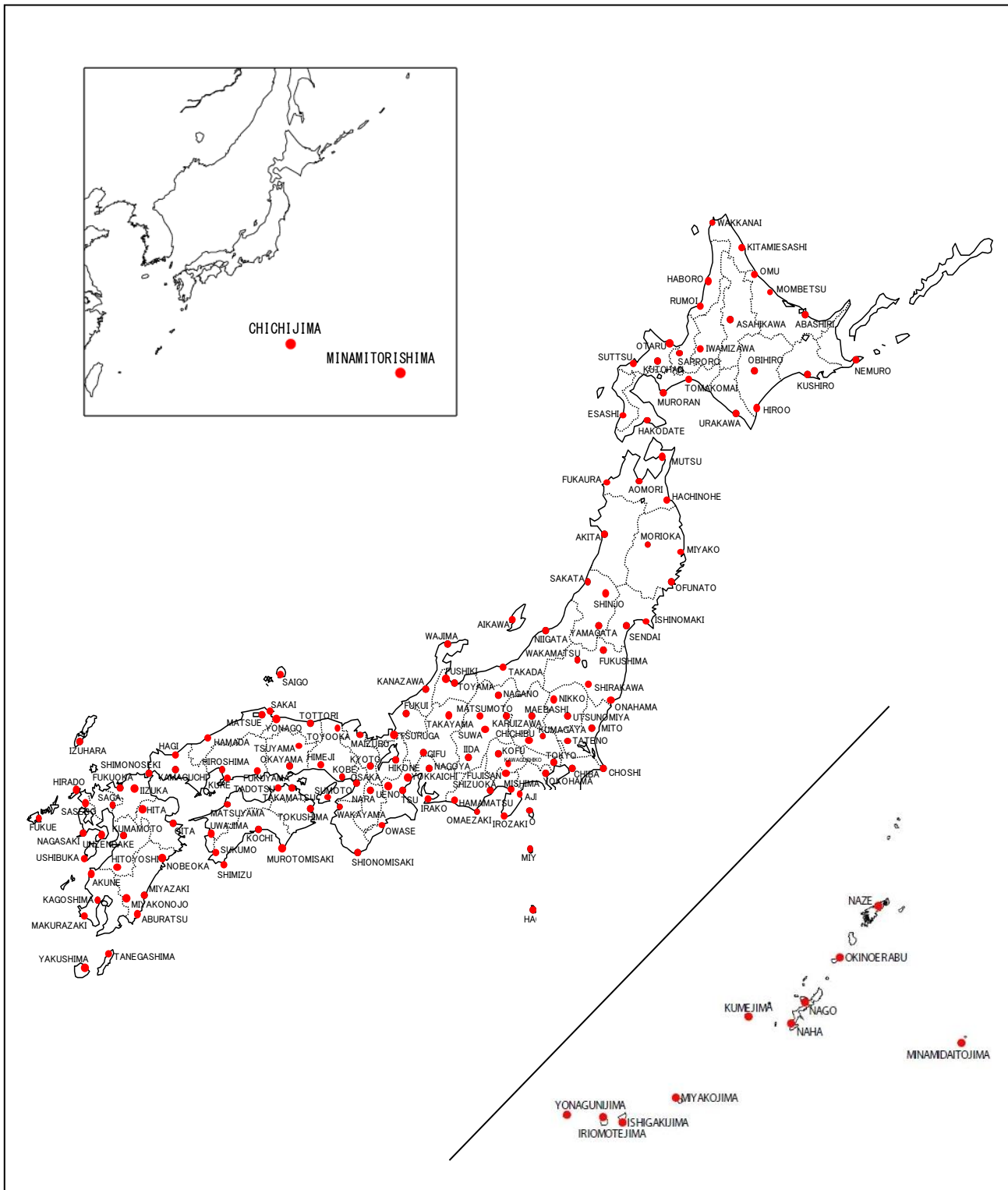
Montreal Protocol: The Montreal Protocol on Substances that Deplete the Ozone Layer (a protocol to the Vienna Convention for the Protection of the Ozone Layer) is an international treaty designed to protect the ozone layer by phasing out the production of numerous substances believed to be responsible for ozone depletion. The treaty was opened for signatures in 1987 and came into force in 1989. Since then, it has undergone several revisions. Japan ratified the protocol in 1988.

ppm, ppb, ppt: In this report, greenhouse gas concentrations are described in terms of mole fractions in units of ppm/ppb/ppt, representing the numbers of molecules of the gas per million/billion/trillion molecules of dry air, respectively.

Terms relating to water masses

North Pacific Subtropical Mode Water (NPSTMW) area: A thermostat between the seasonal and main thermoclines. The NPSTMW area is considered to form in the surface mixed layer just south of the Kuroshio Extension as a result of huge heat loss in winter. It is defined as an area of 16 – 18-degree water at depths of 100 to 400 m at around 20 to 30°N along the 137°E line.

North Pacific Intermediate Water (NPIW) area: The NPIW area forms in the mixed region between the Kuroshio Extension and the Oyashio front. It is defined as water with a salinity level of 34.0 or less at a depth of around 800 m at around 20 to 30°N along the 137°E line.



Distribution of surface meteorological observation stations in Japan

References

News

- Ballantyne, A. P., et al., 2012: Increase in observed net carbon dioxide uptake by land and oceans during the past 50 years, *Nature*, 488, 70-72, <https://doi.org/10.1038/nature11299>.
- Friedlingstein, P., et al., 2021: Global Carbon Budget 2021, *Earth Syst. Sci. Data*, doi:10.5194/essd-2021-386.
- IPCC, 2019: IPCC Special Report on the Ocean and Cryosphere in a Changing Climate [H.-O. Pörtner, D.C. Roberts, V. Masson-Delmotte, P. Zhai, M. Tignor, E. Poloczanska, K. Mintenbeck, A. Alegria, M. Nicolai, A. Okem, J. Petzold, B. Rama, N.M. Weyer (eds.)]. In press.
- IPCC, 2021: Climate Change 2021: The Physical Science Basis. Contribution of Working Group I to the Sixth Assessment Report of the Intergovernmental Panel on Climate Change [Masson-Delmotte, V., P. Zhai, A. Pirani, S.L. Connors, C. Pean, S. Berger, N. Caud, Y. Chen, L. Goldfarb, M.I. Gomis, M. Huang, K. Leitzell, E. Lonnoy, J.B.R. Matthews, T.K. Maycock, T. Waterfield, O. Yelekci, R. Yu, and B. Zhou (eds.)]. Cambridge University Press. In Press.
- Jones, C. D. et al., 2021 : The climate response to emissions reductions due to COVID-19: Initial results from CovidMIP. *Geophys. Res. Lett.*, 48, e2020GL091883. <https://doi.org/10.1029/2020GL091883>.
- Kuroda, H. and T. Setou, 2021: Extensive Marine Heatwaves at the Sea Surface in the Northwestern Pacific Ocean in Summer 2021. *Remote Sens.* 2021, 13, 3989. <https://doi.org/10.3390/rs13193989>.
- Miyama T, Minobe S and H. Goto, 2021: Marine Heatwave of Sea Surface Temperature of the Oyashio Region in Summer in 2010–2016. *Front. Mar. Sci.* 7:576240. doi: 10.3389/fmars.2020.576240.
- Tohjima, Y. et al., 2020: Detection of fossil-fuel CO₂ plummet in China due to COVID-19 by observation at Hateruma. *Scientific Reports*, 10(1), 18688, doi:10.1038/s41598-020-75763-6.
- Tohjima, Y. et al., 2022: Did Atmospheric CO₂ and CH₄ Observation at Yonagunijima Detect Fossil-Fuel CO₂ Reduction due to COVID-19 Lockdown?, *Journal of the Meteorological Society of Japan. Ser. II*, Article ID 2022-021, <https://doi.org/10.2151/jmsj.2022-021> (in press).
- WMO, 2009: Technical report of global analysis method for major greenhouse gases by the World Data Center for Greenhouse Gases. GAW Report , 184, WMO/TD, 1473.
- WMO, 2020: WMO Greenhouse Gas Bulletin, 16.
https://library.wmo.int/index.php?lvl=notice_display&id=3030
- WMO, 2021a: WMO Greenhouse Gas Bulletin, 17.
https://library.wmo.int/index.php?lvl=notice_display&id=3030
- WMO, 2021b: United In Science 2021: A multi-organization high-level compilation of the latest climate science information.
- WMO, 2022: WMO WDCGG DATA SUMMARY, WDCGG No.46, GAW Data Volume IV-Greenhouse Gases and Other Atmospheric Gases, published by the Japan Meteorological Agency in co-operation with World Meteorological Organization. Available at <https://gaw.kishou.go.jp/publications/summary>. (in preparation)

Chapter 1

- EM-DAT: The OFDA/CRED International Disaster, Database – www.emdat.be – Université Catholique de Louvain – Brussels – Belgium
- JMA, 1997: Monthly Report on Climate System, June 1997.
- Ishii, M., A. Shouji, S. Sugimoto and T. Matsumoto, 2005: Objective Analyses of Sea-Surface Temperature and Marine Meteorological Variables for the 20th Century Using ICOADS and the KOBE Collection. *Int. J. of*

Climatology, 25, 865-879.

Kobayashi et al., 2015: The JRA-55 Reanalysis: General specifications and basic characteristics. *J. Meteor. Soc. Japan.*, 93, 5-48.

Chapter 2

Aono and Saito, 2010: Cherry blossom phenology and temperature reconstructions at Kyoto. <http://atmenv.envi.osakafu-u.ac.jp/aono/kyophenotemp4/>

Dettinger, M. D. and M. Ghil, 1998: Seasonal and interannual variations of atmospheric CO₂ and climate. *Tellus*, 50B, 1–24.

Doney, S. C., V. J. Fabry, R. A. Feely and J. A. Kleypas, 2009: Ocean acidification: The other CO₂ problem, *Annu. Rev. Mar. Sci.*, 1, 169–192, doi:10.1146/annurev.marine.010908.163834.

Friedlingstein, P., et al., 2021: Global Carbon Budget 2021, *Earth Syst. Sci. Data*, doi:10.5194/essd-2021-386.

Fujibe, F., 1999: Time of observation bias in the climatological data of daily minimum and maximum temperature in Japan. *Tenki*, 46, 819-830 (in Japanese with English abstract)

Iida, Y., et al., 2021: Global trends of ocean CO₂ sink and ocean acidification: an observation-based reconstruction of surface ocean inorganic carbon variables. *J. Oceanogr.*, doi.org/10.1007/s10872-020-00571-5.

IPCC, 2019: IPCC Special Report on the Ocean and Cryosphere in a Changing Climate [H.-O. Pörtner, D.C. Roberts, V. Masson-Delmotte, P. Zhai, M. Tignor, E. Poloczanska, K. Mintenbeck, A. Alegria, M. Nicolai, A. Okem, J. Petzold, B. Rama, N.M. Weyer (eds.)]. In press.

IPCC, 2021: Climate Change 2021: The Physical Science Basis. Contribution of Working Group I to the Sixth Assessment Report of the Intergovernmental Panel on Climate Change [Masson-Delmotte, V., P. Zhai, A. Pirani, S.L. Connors, C. Pean, S. Berger, N. Caud, Y. Chen, L. Goldfarb, M.I. Gomis, M. Huang, K. Leitzell, E. Lonnoy, J.B.R. Matthews, T.K. Maycock, T. Waterfield, O. Yelekci, R. Yu, and B. Zhou (eds.)]. Cambridge University Press. In Press.

Ishii, M., A. Shouji, S. Sugimoto and T. Matsumoto, 2005: Objective Analyses of Sea-Surface Temperature and Marine Meteorological Variables for the 20th Century Using ICOADS and the KOBE Collection. *Int. J. of Climatology*, 25, 865-879.

Ishii, M., Y. Fukuda, H. Hirahara, S. Yasui, T. Suzuki, and K. Sato, 2017: Accuracy of Global Upper Ocean Heat Content Estimation Expected from Present Observational Data Sets. *SOLA*, Vol. 13, 163-167, doi:10.2151/sola.2017-030.

Keeling, C. D., T. P. Whorf, M. Wahlen and J. van der Plicht, 1995: Interannual extremes in the rate of rise of atmospheric carbon dioxide since 1980. *Nature*, 375, 666–670.

Keeling, R. F., S. C. Piper, and M. Heinmann, 1996: Global and hemispheric CO₂ sinks deduced from changes in atmospheric O₂ concentration. *Nature*, 381, 218-221.

Kudo, R., et al., 2012: Aerosol impact on the brightening in Japan. *J. Geophys. Res.*, 117(D07208), doi:10.1029/2011JD017158.

Le Quéré, C., et al., 2016: Global Carbon Budget 2016, *Earth Syst. Sci. Data*, 8, 605-649, doi:10.5194/essd-8-605-2016.

Mantua, N. J. and S. R. Hare, 2002: The Pacific Decadal Oscillation. *J. Oceanogr.*, 58, 35 – 44, doi: 10.1023/A:1015820616384.

Montzka, S. A. et al., 2018: An unexpected and persistent increase in global emissions of ozone-depleting CFC-11, *Nature*, 557, 413-417, doi:10.1038/s41586-018-0106-2.

Montzka, S. A. et al., 2021: A decline in global CFC-11 emissions during 2018-2019. *Nature*, 590, 428-432,

- <https://doi.org/10.1038/s41586-021-03260-5>.
- Niwa, Y., et al., 2014: Seasonal Variations of CO₂, CH₄, N₂O and CO in the Mid-Troposphere over the Western North Pacific Observed Using a C-130H Cargo Aircraft. *J. Meteorol. Soc. Japan*, 92(1), 50-70, doi:10.2151/jmsj.2014-104.
- Norris, J. R., and M. Wild, 2009: Trends in aerosol radiative effects over China and Japan inferred from observed cloud cover, solar “dimming,” and solar “brightening.”. *J. Geophys. Res.*, 114(D00D15), doi:10.1029/2008JD011378.
- Ohmura, A., 2009: Observed decadal variations in surface solar radiation and their causes. *J. Geophys. Res.*, 114(D00D05), doi: 10.1029/2008JD011290.
- Park, S., et al., 2021: A decline in emissions of CFC-11 and related chemicals from eastern China. *Nature*, 590, 433-437, <https://doi.org/10.1038/s41586-021-03277-w>.
- Rayner, P. J., I. G. Enting, R. J. Francey, and R. Langenfelds, 1999: Reconstructing the recent carbon cycle from atmospheric CO₂, δ¹³C and O₂/N₂ observations. *Tellus*, 51B, 213-232.
- Rigby, M., et al., 2019: Increase in CFC-11 emissions from eastern China based on atmospheric observations, *Nature*, 569, 546-550, doi:10.1038/s41586-019-1193-4.
- Saito, T., et al., 2015: Extraordinary halocarbon emissions initiated by the 2011 Tohoku earthquake. *Geophys. Res. Lett.*, 42, doi:10.1002/2014GL062814.
- Sweeney, C., et al., 2015: Seasonal climatology of CO₂ across North America from aircraft measurements in the NOAA/ESRL Global Greenhouse Gas Reference Network, *J. Geophys. Res. Atmos.*, 120, 5155-5190, doi:10.1002/2014JD022591.
- Tsuboi, K., et al., 2013: Evaluation of a new JMA aircraft flask sampling system and laboratory trace gas analysis system. *Atmos. Meas. Tech.*, 6, 1257–1270, doi:10.5194/amt-6-1257-2013.
- Umezawa, T., et al., 2018: Seasonal evaluation of tropospheric CO₂ over the Asia-Pacific region observed by the CONTRAIL commercial airliner measurements, *Atmos. Chem. Phys.*, 18, 14851-14866, doi:10.5194/acp-18-14851-2018.
- WCRP, 2010: Summary Report from the Eleventh Baseline Surface Radiation Network (BSRN) Scientific Review and Workshop. WCRP Informal Report No. 08/2010, 21pp.
- Wild, M., 2009: Global dimming and brightening: A review. *J. Geophys. Res.*, 114(D00D16), doi:10.1029/2008JD011470.
- Wild, M. and A. Ohmura, 2004: BSRN longwave downward radiation measurements combined with GCMs show promise for greenhouse detection studies. *GEWEX news*, 14, 4, 20 pp.
- WMO, 2009: Technical report of global analysis method for major greenhouse gases by the World Data Center for Greenhouse Gases. GAW Report , 184, WMO/TD, 1473.
- WMO, 2018a: Scientific assessment of ozone depletion: 2018. Global Ozone Research and Monitoring Project-Report, 58.
- WMO, 2018b: WMO Greenhouse Gas Bulletin, 14.
https://library.wmo.int/index.php?lvl=notice_display&id=3030
- WMO, 2021: WMO Greenhouse Gas Bulletin, 17.
https://library.wmo.int/index.php?lvl=notice_display&id=3030
- WMO, 2022: WMO WDCGG DATA SUMMARY, WDCGG No.46, GAW Data Volume IV-Greenhouse Gases and Other Atmospheric Gases, published by the Japan Meteorological Agency in co-operation with World Meteorological Organization. Available at <https://gaw.kishou.go.jp/publications/summary>. (in preparation)